The effect of ultra-low frequency waves on magnetosphere–ionosphere coupling at high-latitude

a multi-instrument study

Charlotte Maartje van Hazendonk

Thesis for the degree of Philosophiae Doctor (PhD)
University of Bergen, Norway
2026

UNIVERSITY OF BERGEN

The effect of ultra-low frequency waves on magnetosphere–ionosphere coupling at high-latitude

a multi-instrument study

Charlotte Maartje van Hazendonk

Thesis for the degree of Philosophiae Doctor (PhD)
at the University of Bergen

Date of defense: 10.02.2026

Year: 2026

Title: The effect of ultra-low frequency waves on magnetosphere–ionosphere coupling at high-latitude

Name: Charlotte Maartje van Hazendonk

Print: Skipnes AS / University of Bergen

Scientific environment

This dissertation has been partly funded by the Birkeland Centre for Space Science (BCSS), a Norwegian Centre of Excellence (Norwegian Research Council project number 223252) until its conclusion in 2023. The work has been carried out at the Department of Arctic Geophysics at the University Centre in Svalbard (UNIS) and at the Department of Physics and Technology at the University of Bergen (UiB).

Acknowledgements

First and foremost, I am really thankful to my main supervisor, Lisa. Your passion for ULF waves always managed to help me out with new ideas and your knowledge of both ULF waves and (EISCAT) radars was a big part of making this PhD a success. Thank you for all the discussions we had together and the feedback on my countless number of drafts over the years without any complaint. I could not have wished for a more encouraging supervisor. Kalle, I am really grateful for how seriously you took your role as co-supervisor. Despite your (more than) full calendar, you always tried to make time for our meetings, bringing a lot of valuable insights and discussion points to the table. Also, thank you for always making me feel part of your group in Bergen. To my other collaborators: Koki, thank you for giving me fresh ideas when my detection method was not yet working. Dag, thank you for the MSP data. Anasuya and Ian, thank you for the cloud and FPI data. It was lovely to meet you in my final PhD days.

To my close colleagues: Noora, thank you for always being available to talk–about science, life, or the weather to plan our next hike or skiing trip. I will not soon forget the ti topper. Mikko, thank you for all your help, the discussions that sometimes left me with more questions than I started with, but also helped me with tackling some of the revisions that came along. Fred, my very first supervisor at UNIS, without you I would never have even visited Svalbard, let alone lived here for the past 6.5 years, and I would probably never have studied space physics. And Katie, thank you for teaching me how to teach and getting me out of my comfort zone by designing the KHO escape room together. And thank you for showing me Svalbard (cabin) life and all the shared trips. A big thank you to the other PhDs at UNIS. Nina, for helping me with different data sources and UNIS bureaucracy. Lena, for sharing an office and all the chats that came with it. Kjersti, for being my jacket and sushi buddy (together with Emma & Lindis). Lukas, thank you for all the trips we shared. From my very first hike in Svalbard in August 2019 to the very last one after your defense, and everything in between, there were some truly magical trips there. Joe, thank you for introducing me to ski waxing and skiing equipment in general, but most of all, thank you for always being there for a chat (usually with one of your bakings). To the PhD group in Bergen–especially Margot

and Simon–thank you for always making me feel welcome and letting me tag along. To the rest of my colleagues at UNIS, thank you for all the fun talks and laughs we shared. And Nataly, I will miss the Tuesday and Thursday stretching sessions.

To my Svalbard friends over the years: Marjolein, thank you for always being there, all the dinners, and the trips we went on. I also really enjoyed visiting you in Lausanne. Nil, Tomi, Richard, Tobias, Cecilie, Franka, Amélie, Guillaume, Lidia, and all the others who were part of this journey: whether it was hiking, skiing, innebandy, cabin trips, dinners, movie nights, or just a chat, you made my life in Svalbard way more fun.

Ook wil ik al mijn vrienden in Nederland bedanken die ervoor hebben gezorgd dat Nederland nog steeds als thuis voelt. Alexandra, Céline, Nina en Sophia: ik vind het heel bijzonder dat wij al meer dan een half leven zulke goede vriendinnen zijn en ik kijk er elke keer weer naar uit om jullie te zien. Jullie bezoek aan Spitsbergen was een hoogtepunt en gaf mij een kans om te laten zien wat ik de afgelopen 6.5 jaar met mijn leven heb gedaan :) Quasar, het is altijd een feestje om bij te praten en ons allemaal bij elkaar te krijgen als ik in Nederland ben. Mathieu, dankjewel voor alle (digitale) gesprekken en adviezen. Het voelt heel fijn om onderdeel van elkaars leven te zijn. Verder een dankjewel naar alle mensen die in de loop van de jaren langs zijn gekomen op Spitsbergen en aan wie ik een inkijkje mocht geven in mijn leven hier.

Lieve papa, mama en Laura, dankjulliewel voor jullie steun ondanks dat ik ervoor koos om 3000 km verderop te gaan wonen. Jullie zien gelukkig mijn passie voor Spitsbergen en ik vond het geweldig om mijn leven hier met jullie te delen en de verschillende plekken te laten zien tijdens jullie bezoeken. Ook was het altijd fijn dat jullie relativering brachten als mijn PhD even niet zo lekker liep. Ondanks dat ik ver weg woon, voel ik mij altijd welkom bij jullie en hoewel de bezoeken minder frequent zijn dan ik soms zou willen, is de tijd zelf intenser en vol van liefde. Dank dat ik altijd welkom ben bij jullie! Lieve Laura, Koen, Ties (en Pluk), ik vond het geweldig om Ties te ontmoeten, in mijn armen te houden en om jullie liefde voor Ties te zien. De verwoestende bacterie en het peilloze verdriet daarna waren hartverscheurend en maakten dat de afstand met Nederland soms bijna onoverbrugbaar was. Dankjewel voor het toelaten van mij (zowel in persoon als op afstand) bij jullie verdriet.

En als laatste, dankjewel Peter voor je rugkrabbels, al je bezoeken aan Longyearbyen en het vertrouwen dat je in mij hebt. Je weet mijn stresslevels te verlagen en helpt waar mogelijk (dank voor het herinstalleren van software en het geduld waarmee je het vervolgens aan mij uitlegt!). Dankjewel!

Lotte van Hazendonk
Longyearbyen, November 2025

Use of AI

In the course of preparing this thesis, ChatGPT has been used to provide assistance with wording and to enhance the language in selected paragraphs. All such contributions were thoroughly reviewed and, where necessary, revised by the author, who bears sole responsibility for the final content of the work.

Abstract

Ultra-low frequency (ULF) waves are defined as magnetohydrodynamic oscillations with frequencies in the range of 1 mHz to 1 Hz. They transfer energy and momentum between the solar wind, Earth's magnetosphere, and ionosphere. ULF waves occur in the magnetosphere and can indirectly be observed in the ionosphere via periodic fluctuations in plasma parameters, magnetic field perturbations, or via the formation of auroral arcs, also known as ULF wave-driven auroral arcs (UAAs).

This PhD thesis investigates the generation, propagation, and energy exchange mechanisms of ULF waves, with a focus on their role in magnetosphere–ionosphere coupling. A combination of incoherent scatter radar (ISR) data, optical observations, such as from the meridian scanning photometer (MSP), satellite measurements, and inversion models is used to address the thesis' main objectives: (1) to quantify energy dissipation, from both electromagnetic and kinetic fluxes, (2) to analyze occurrence and propagation characteristics of ULF wave-driven auroral arcs at high-latitudes, and (3) to appraise the role of ULF waves in magnetosphere–ionosphere coupling via ion upflow, and field-aligned currents.

The research comprises three peer-reviewed studies: Paper I details the development of an automatic detection method for ULF waves in ISR data and the quantification of energy dissipation during a ULF wave event. The study reveals that the kinetic energy flux can be comparable in magnitude to the electromagnetic flux and that the total energy budget of a ULF wave event can amount to around 10% of that of a magnetospheric substorm. In Paper II, we conduct a statistical analysis of UAAs detected in MSP data using a modified version of the detection method developed in Paper I. The detected UAA database, covering the dawn and dusk sectors, contains 198 events recorded over 17 seasons of data. In this database, a significant equatorward propagating population is present, while previous studies of equatorward propagating UAAs were limited to three case studies. Part of the database, furthermore, consists of small-scale ULF waves, showing that small-scale waves can be associated with auroral emissions. Paper III documents the first direct link between UAAs and ion upflow at high-latitude.

In addition, the work explores the magnetosphere–ionosphere coupling further by quantifying FAC magnitudes, and energy dissipation into the ionosphere, showing a strong connection between UAAs and magnetosphere–ionosphere coupling.

Sammendrag

Ultralavfrekvente (ULF) bølger er definert som magnetohydrodynamiske oscillasjoner med frekvenser fra omtrent 1 mHz til 1 Hz. Disse bølgene overfører energi og bevegelsesmengde mellom solvinden, jordens magnetosfære og ionosfæren. ULF-bølger oppstår i magnetosfæren og kan indirekte observeres i ionosfæren gjennom periodiske fluktuasjoner i plasma-parametere, magnetfeltforstyrrelser eller gjennom dannelsen av nordlysbuer, også kjent som ULF-bølgedrevne nordlysbuer (UAAs).

Denne doktorgradsavhandlingen undersøker generering, forplantning og energioverføringsmekanismer for ULF-bølger, med fokus på deres rolle i koblingen mellom magnetosfæren og ionosfæren. En kombinasjon av data fra inkoherent spredning-radar (ISR), optiske observasjoner som meridianskanningsfotometer (MSP), satellittmålinger og inversjonsmodeller brukes for å adressere avhandlingens hovedmål: (1) å kvantifisere energiavsetning fra både elektromagnetiske og kinetiske flukser, (2) å analysere forekomst og forplantningsegenskaper til ULF-bølgedrevne nordlysbuer ved høye breddegrader, og (3) å vurdere ULF-bølgenes rolle i magnetosfære–ionosfære–kobling gjennom oppstrømmende ioner og Birkelandstrømmer.

Forskningen består av tre fagfellevurderte studier: Artikkel I beskriver utviklingen av en automatisk deteksjonsmetode for ULF-bølger i ISR-data og kvantifiseringen av energiavsetning under en ULF-bølgebegivenhet. Studien viser at den kinetiske energifluksen kan være sammenlignbar i størrelse med den elektromagnetiske fluksen, og at det totale energibudsjettet for en ULF-bølgebegivenhet kan utgjøre rundt 10% av en magnetosfærisk substorm. I Artikkel II gjennomføres en statistisk analyse av UAAs detektert i MSP-data ved bruk av en modifisert versjon av deteksjonsmetoden utviklet i Artikkel I. Den detekterte UAA-databasen, som dekker morgen- og ettermiddagssektorene, inneholder 198 begivenheter registrert over 17 sesonger med data. I denne databasen er det en betydelig populasjon av bølger som propagerer mot ekvator, mens tidligere studier av slike UAAs var begrenset til tre begivenhetstudier. En del av databasen består også av småskala ULF-bølger, som viser at småskalabølger kan være assosiert med nordlysemisjoner. Artikkel III dokumenterer den første direkte koblingen mellom

UAAs og oppstrømning av ioner ved høye breddegrader. I tillegg utforsker arbeidet magnetosfære–ionosfære–koblingen videre ved å kvantifisere Birkelandstrømmenes styrke og energiavsetning i ionosfæren, noe som viser en sterk sammenheng mellom UAAs og magnetosfære–ionosfære–koblingen.

List of publications

This thesis consists of three papers preceded by an introduction on the background theory relevant to the papers, as well as a description on the different data sources and methods used. The three scientific papers which compose the main results of this thesis are:

1. van Hazendonk, C. M., Baddeley, L., Laundal, K. M., Chau, J. L. (2024). *Detection and Energy Dissipation of ULF Waves in the Polar Ionosphere: A Case Study Using the EISCAT Radar*, Journal of Geophysical Research: Space Physics, Volume 129, Issue 7, e2024JA032633, doi: 10.1029/2024JA032633.

2. van Hazendonk, C. M., Baddeley, L., Laundal, K. M., Lorentzen, D. A. (2025). *A statistical study of optical signatures of high-latitude Pc5 waves*, Journal of Atmospheric and Solar-Terrestrial Physics, Volume 274, Pages 106585, doi: 10.1016/j.jastp.2025.106585.

3. van Hazendonk, C. M., Baddeley, L., Laundal, K. M., Partamies, N. (2025). *High-latitude observations of ULF wave driven ion upflow*, in public review for Annales Geophysicae, doi: 10.5194/egusphere-2025-5220 (preprint, public discussion)

Through the course of my PhD, I have also authored and co-authored other peer-reviewed publications on related topics, namely:

A van Hazendonk, C. M., Heino, E., Jiggens, P. T. A., Taylor, M. G. G. T., Partamies, N., Mulders, H. C. J. (2022). *Cutoff Latitudes of Solar Proton Events Measured by GPS Satellites*, Journal of Geophysical Research: Space Physics, Volume 127, Issue 3, e2021JA030166, doi: 10.1029/2021JA030166.

B Herlingshaw, K., Partamies, N., van Hazendonk, C. M., Syrjäsuo, M., Baddeley, L., Johnsen, M., Eriksen, N., McWhirter, I., Aruliah, A., Engebretson, M., Oksavik, K., Sigernes, F., Lorentzen, D., Nishiyama, T., Cooper, M., Meriwether,

J., Haaland, S., Whiter, D. (2025), *Science highlights from the Kjell Henriksen Observatory on Svalbard*, Artic Sicence, Volume 11, doi: 10.1139/as-2024-0009.

Contents

Chapter 1

Introduction

The Earth's magnetosphere is a dynamic region shaped by the interaction between the planet's intrinsic magnetic field and the solar wind–a continuous stream of charged particles emanating from the Sun. In this interaction, transfer of energy, mass and momentum occurs from the solar wind into the magnetosphere and further down into the ionosphere (*Dungey*, 1961; *Hasegawa et al.*, 2004). The energy entering the ionosphere can be carried in two forms, namely electromagnetic energy–quantified through the Poynting flux–and kinetic energy (*Thayer and Semeter*, 2004).

Ultra-low frequency (ULF) waves play a central role in the redistribution and transport of this energy within the Earth's magnetosphere. These waves are typically defined as magnetohydrodynamic (MHD) oscillations in the frequency range of 1 mHz to 1 Hz and occur in the magnetosphere. In simpler terms, MHD oscillations can be viewed as coupled fluctuations in both plasma–treated as a conducting fluid–and the magnetic field. Because plasma and magnetic fields are tightly linked, a disturbance in one propagates as a wave through the other. Under certain conditions, these waves can become resonant with the natural oscillation frequency of magnetic field lines, leading to so-called field line resonances (FLRs). This process is analogous to the vibration of a guitar string when plucked at one of its natural frequencies. ULF waves can be excited through a range of processes, which can be divided into generation mechanisms external and internal to the magnetosphere. Externally, solar wind–magnetosphere coupling processes, such as solar wind pressure variations (*Kepko et al.*, 2002) and the Kelvin-Helmholtz instability (*Kivelson and Southwood*, 1985, 1986) can excite ULF waves. Internally, wave-particle interactions from substorm injected particle populations or the radiation belts among others can generate or amplify ULF waves. Once generated, ULF waves can propagate throughout the magnetosphere, coupling energy between different plasma regions and acting as conduits for both electromagnetic and kinetic energy transfer into the

ionosphere (*Southwood and Hughes*, 1983; *Thayer and Semeter*, 2004).

A direct way to observe magnetospheric ULF wave activity in the ionosphere is via auroral phenomena. Through FLRs and modulation of particle precipitation, ULF waves can influence the formation and motion of auroral arcs–visible light emissions caused by charged particles colliding with the Earth's upper atmosphere (*Samson et al.*, 2003; *Rankin et al.*, 2021). These arcs, which can be considered as ULF wave-driven auroral arcs, not only serve as beautiful visual indicators of space weather, but also provide critical observational signatures of ULF wave dynamics, energy dissipation in the ionosphere, and magnetosphere–ionosphere coupling. Visible aurora indicates electron acceleration and thus the presence of a kinetic energy flux. Furthermore, auroral arcs have been studied in relation to ion outflow, indicating their relevance in magnetosphere–ionosphere coupling (*Lynch et al.*, 2007). Previous literature on ULF waves (e.g *Fenrich et al.*, 2019; *Hartinger et al.*, 2015; *Rae et al.*, 2007), however, ignores the existence of this kinetic flux and focuses on quantifying the electromagnetic energy flux into the ionosphere through a series of assumptions, thus potentially underestimating the total energy dissipation in the ionosphere caused by ULF waves. In addition, optical signatures of ULF waves are mostly observed when ULF waves are propagating poleward using case studies (e.g. *Yin et al.*, 2023; *Motoba et al.*, 2021; *Kozlovsky et al.*, 2006) and one statistical study (*Gillies et al.*, 2018). On the other hand, equatorward propagating ULF waves are predominantly reported in radar studies (e.g. *Michael et al.*, 2024; *James et al.*, 2013; *Mager et al.*, 2009), with only three known optical counterparts at high-latitudes (*Baddeley et al.*, 2017; *Rae et al.*, 2014; *Mathews et al.*, 2004).

Thesis Objectives

This thesis focuses on ULF waves, more specifically the Pc5 and Pc6 band ($\sim$ 0.5–7 mHz). We explore generation mechanisms, occurrence statistics, and energy dissipation associated with ULF waves as well as their role in the magnetosphere–ionosphere coupling. The main objectives of this thesis are to

1. **Quantify the energy dissipation in the ionosphere, divided into separate electromagnetic and kinetic energy fluxes, of ULF wave events.**

2. **Find occurrence statistics, propagation direction, and characteristics of ULF wave-driven auroral arcs at high-latitudes.**

3. **Investigate the role of ULF waves in the magnetosphere–ionosphere coupling via ion upflow and field-aligned currents.**

To achieve these objectives, this thesis includes three papers, which comprise two case studies and a statistical study. The first objective aims to quantify how the energy dissipation of ULF waves has previously been underestimated when only the electromagnetic energy flux was considered. To fulfill this objective, Paper I, a case study, uses incoherent scatter radar (ISR) data to quantify energy dissipation of ULF waves. To allow for easier processing of the data, an automatic detection method is developed that can trace the wave fronts of the ULF waves in low-elevation ISR data. Additional data sources, such as ground-based magnetometers, confirm the presence of the ULF wave event. Paper III continues to investigate energy dissipation, but broadens the perspective by including other magnetosphere–ionosphere coupling mechanisms such as ion upflow and field-aligned currents, thus also addressing Objective 3. ISRs looking in field-aligned orientation allow us to investigate the upflow of particles and field-aligned current magnitudes. The localized ISR measurements are put into a larger-scale perspective by using ground-based magnetometers, spacecraft, and inversion models. To our knowledge, this study provides the first connection between the occurrence of ULF wave-driven auroral arcs and ion upflow.

The second objective aims to address the knowledge gap on optical signatures of equatorward propagating ULF wave-driven auroral arcs and how their characteristics differ from their poleward propagating counterparts. The second objective is studied in Paper II through a statistical study at high-latitude. Events for this statistical study are found in data from the meridian scanning photometer (MSP) located in Longyearbyen, Svalbard, by adjusting the automatic detection mechanism from Paper I to fit this data source. To avoid false positives due to the presence of other optical phenomena, this statistical study focuses on the dawn and dusk sectors. The case study in Paper III was originally identified in the statistical study presented in Paper II.

Thesis Outline

Chapter 2 describes background theory to put the work into context. Subsequently, Chapter 3 discusses the relevant instrumentation and models, their corresponding datasets, and limitations. The developed detection method and the three papers comprised in this thesis are summarized in Chapter 4. Finally, Chapter 5 presents the conclusions and outlines directions for future research. The complete papers are provided at the end.

Chapter 2

Background Theory

This chapter introduces the key theoretical concepts that help understand the results presented in the three papers included in this thesis. Section 2.1 introduces basic space plasma physics principles including both single particle motion and the magnetohydrodynamical approach. Section 2.2 describes the relevant regions in the Sun-Earth system, while Section 2.3 focuses on the coupling between those, the relevant current systems, and auroral emissions. Waves are introduced in Section 2.4 and expanded upon in Sections 2.5 and 2.6. Lastly, Section 2.7 discusses the energy exchange processes between the magnetosphere and the ionosphere. The energy dissipation into the ionosphere–comprising electromagnetic and kinetic energy fluxes–can occur along with ion upflow and outflow.

The contents of this chapter are largely based on the works of *Baumjohann and Treumann* (1996) (Sections 2.1, 2.3, and 2.4), *Kivelson and Russell* (1995) (Sections 2.2, 2.3, and 2.4), *Brekke* (2013) (Section 2.3), *Menk and Waters* (2013) (Sections 2.5 and 2.6), *Schunk and Nagy* (2009) (Section 2.7), and *Thayer and Semeter* (2004) (Section 2.7).

2.1 Plasma Behavior

Most matter in the Sun-Earth space environment exists in the plasma state. A plasma is a quasi-neutral gas consisting primarily of charged particles, with approximately equal numbers of positive and negative charges (*Kivelson and Russell*, 1995). To understand wave behavior and the associated transfer of energy and momentum, we first need to examine the motion of these waves and the particles that support them. Depending on the conditions, we can look at the individual particles (microscopic level), or at

collective behavior of plasma (macroscopic level). At the macroscopic level, plasma can be described as a fluid by magnetohydrodynamics.

2.1.1 Single Charged Particle Motion in Electromagnetic Fields

Charged particles in an electromagnetic field are subject to the Lorentz force, $\boldsymbol{F_L}$, where

$$\boldsymbol{F_L} = q(\boldsymbol{E} + \boldsymbol{v} \times \boldsymbol{B}). \tag{2.1}$$

q is the charge, $\boldsymbol{E}$ the electric field, $\boldsymbol{v}$ the velocity, and $\boldsymbol{B}$ the magnetic field. Combining Equation 2.1 with Newton's second law of motion,

$$\boldsymbol{F} = m\boldsymbol{a}, \tag{2.2}$$

where m is the mass and $\boldsymbol{a}$ the acceleration of a particle, results in

$$m\boldsymbol{a} = q(\boldsymbol{E} + \boldsymbol{v} \times \boldsymbol{B}). \tag{2.3}$$

In this equation, other forces such as the gravitational and pressure gradient force are ignored since the electromagnetic force is assumed to be dominant. Equation 2.3 allows us to identify three types of key particle motion: (1) gyromotion, (2) bounce motion, and (3) drift motion as shown in Figure 2.1.

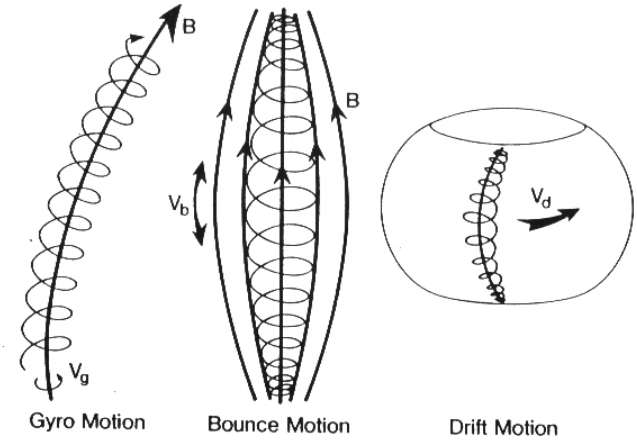

Figure 2.1: Schematic overview of the three main single particle motions due to the magnetic field. Figure from *Kivelson and Russell* (1995).

The first two types of motion are best explained when $\boldsymbol{E}$ is assumed to be zero. In case of a uniform magnetic field, a charged particle will undergo a circular motion around its

guiding center, also known as gyration. Gyromotion is characterized by a gyroradius, $r_g = \frac{mv_\perp}{|q|B}$, and an angular frequency or gyro frequency given by $\omega_g = \frac{qB}{m}$. The sign of the charge results in an opposite gyration direction for ions and electrons. When the magnetic field is non-uniform, the velocity of the particle along the magnetic field line and the radius of gyration will be affected by the strength of the magnetic field. When the magnetic field becomes stronger, the particle can be reflected at the mirror point, causing bounce motion. The particle's mirror point is defined as the location at which the pitch angle, α, defined as the angle between the particle's velocity vector and the magnetic field line, equals 90°. However, not all particles are reflected. Particles with small pitch angles have a velocity component predominantly along the magnetic field and may have reflection points that lie deep within the atmosphere, where the density of neutral particles is high. In such cases, the particle will collide frequently with neutrals, transferring its kinetic energy in the process, and ultimately being absorbed by the atmosphere. This region of pitch angles, where particles are lost instead of reflected, is known as the loss cone.

Drift motion of the particles gyrocenter occurs in the presence of external forces and happens in perpendicular direction to both $\boldsymbol{B}$ and the external force $\boldsymbol{F_{ex}}$. The best known types of drift are $\boldsymbol{E} \times \boldsymbol{B}$ drift due to an electric field (e.g. $\boldsymbol{E} \neq 0$), gradient drift due to magnetic inhomogeneities, and curvature drift due to the curvature of magnetic field lines. The curvature and gradient of the magnetic field cause electrons and protons to drift in opposite directions, causing a net current to flow. At Earth, this current is known as the ring current.

2.1.2 Magnetohydrodynamics

At large-scales, a plasma is usually described using collective behavior rather than single particle motion. Specifically, the plasma is often treated as a fluid. Magnetohydrodynamics (MHD) is used to model and understand behavior of electrically conducting fluids, such as plasmas. It combines Maxwell's electromagnetic equations with conservation laws for mass and charge (continuity equation), and momentum (equation of motion) to describe plasma by macroscopic quantities such as the bulk velocity, $\boldsymbol{v}$, pressure, p, magnetic field, $\boldsymbol{B}$, and mass density, ρ. ρ can be described as $\rho = m_i n_i + m_e n_e$, where $m_{i,e}$ and $n_{i,e}$ are the ion and electron mass and number density, respectively. Since $m_i \gg m_e$ and MHD assumes quasi-neutrality ($n_i \approx n_e \approx n$), we can approximate the mass density as $\rho \approx n m_i$.

In differential form, Maxwell's equations are described by:

$$\nabla \times \boldsymbol{E} = -\frac{\partial \boldsymbol{B}}{\partial t} \text{ (Faraday's law of induction)} \tag{2.4}$$

$$\nabla \times \boldsymbol{B} = \mu_0 \boldsymbol{j} + \epsilon_0 \mu_0 \frac{\partial \boldsymbol{E}}{\partial t} \text{ (Ampère's law)} \tag{2.5}$$

$$\nabla \cdot \boldsymbol{E} = \rho_e / \epsilon_0 \text{ (Gauss' law for electricity)} \tag{2.6}$$

$$\nabla \cdot \boldsymbol{B} = 0 \text{ (Gauss' law for magnetism)} \tag{2.7}$$

where μ_0 and ϵ_0 are the permeability and permittivity of free space, $\boldsymbol{j}$ the current density, and ρ_e the charge density given by $\rho_e = e(n_i - n_e)$. ρ_e thus describes the net charge per unit volume of the plasma. Faraday's and Ampère's law, Equations 2.4 and 2.5, show how the electric and magnetic field are spatially and temporally coupled and how they relate to the current system, which consists of the conduction current, $\mu_0 \boldsymbol{j}$, and the displacement current, $\mu_0 \epsilon_0 \frac{\partial \boldsymbol{E}}{\partial t}$. The latter is neglected in MHD. In order for the system to be a closed loop, Gauss' laws for electricity and magnetism, Equations 2.6 and 2.7, are needed. The first describes how the charge density, ρ_e, defines the electric field, and the latter shows that there are no magnetic monopoles.

The first conservation equation, known as the continuity equation, can be written as

$$\frac{\partial \rho}{\partial t} + \nabla \cdot (\rho \boldsymbol{v}) = 0 \tag{2.8}$$

and describes that the mass density, and number density if $\rho = mn$, are conserved in the absence of production and loss. The equation of motion can be obtained from Newton's second law of motion (Eq 2.2) when external forces, $\boldsymbol{F_{ext}}$, are applied on a plasma element. In this thesis, the gravitational force, given by $\rho \boldsymbol{g}$, where $\boldsymbol{g}$ is the gravitational constant, is negligible compared to the other external forces. This results in a simplified version of the equation of motion given by

$$\rho \frac{d\boldsymbol{v}}{dt} = -\nabla p + \boldsymbol{j} \times \boldsymbol{B}. \tag{2.9}$$

∇p describes the pressure force from the surrounding medium on the plasma element, while $\boldsymbol{j} \times \boldsymbol{B}$ represents the magnetic forces on the plasma. To describe the relation between the current density and the electromagnetic field the generalized Ohm's law can be used

$$\boldsymbol{E} = -(\boldsymbol{v} \times \boldsymbol{B}) + \eta \boldsymbol{j} + \frac{1}{ne} \boldsymbol{j} \times \boldsymbol{B} - \frac{1}{ne} \nabla \cdot \boldsymbol{p_e} + \frac{m_e}{ne^2} \left[\frac{\partial \boldsymbol{j}}{\partial t} + \nabla \cdot (\boldsymbol{j} \boldsymbol{v}) \right], \tag{2.10}$$

where η is the resistivity, and $\boldsymbol{p_e}$ the electron pressure. The $\frac{1}{ne} \boldsymbol{j} \times \boldsymbol{B}$ term is called the

Hall term and is caused by the difference in motion between the electrons and ions. The $\frac{1}{ne}\nabla\cdot\boldsymbol{p_e}$ and $\frac{m_e}{ne^2}\left[\frac{\partial \boldsymbol{j}}{\partial t} + \nabla\cdot(\boldsymbol{jv})\right]$ terms are known as the electron pressure term and inertia term, respectively. For ideal MHD, these three terms as well as the resistivity term ($\eta\boldsymbol{j}$) can be neglected, since the convective term ($\boldsymbol{v}\times\boldsymbol{B}$) is dominant. The generalized Ohm's law can then be simplified to

$$\boldsymbol{E} + \boldsymbol{v}\times\boldsymbol{B} = 0. \tag{2.11}$$

The next conservation equation, the conservation of energy, is usually replaced by an equation of state to close the system:

$$\frac{p}{\rho^\gamma} = \text{constant}, \tag{2.12}$$

where γ is the adiabatic index. The adiabatic index is given by the ratio of two specific heat capacities under constant pressure, c_p, and constant volume, c_v, $\gamma = \frac{c_p}{c_v}$.

In summary, MHD treats plasmas as single, electrically conducting fluids. This means that only one species is considered, neglecting differences between ions and electrons. A simplified version of MHD is known as ideal MHD. In ideal MHD, plasma cannot flow or diffuse across magnetic field lines and the plasma is thus frozen-in to the magnetic field.

2.2 The Solar Wind, Interplanetary Magnetic Field, Earth's Magnetosphere and Ionosphere

The Sun's corona emits a continuous stream of high-speed, charged particles into interplanetary space, known as the solar wind. The solar wind is a highly conducting plasma and its constituents are electrons and ions (*Baumjohann and Treumann*, 1996). Typically, ideal MHD conditions apply to the solar wind. Due to its highly conducting nature, the plasma cannot flow or diffuse across magnetic field lines, but it moves with the magnetic field. The magnetic field lines of the Sun are so-called frozen-in the solar wind plasma (*Alfvén*, 1942). The solar wind thus carries part of the Sun's magnetic field with it as it propagates through space. This is called the interplanetary magnetic field (IMF). These magnetic field lines remain attached to the Sun. The 27-day rotation period of the Sun causes the magnetic field lines to distort into a spiral structure, known as the Parker spiral, as visualized in Figure 2.2 (*Parker*, 1963).

Around Earth, at a distance of 1 astronomical unit (AU) from the Sun, the solar wind has typical magnetic field strengths around 5–10 nT, and velocities ranging from 300 to 1400 km s^{-1}, with typical values between 400–500 km s^{-1}, making the solar wind super-

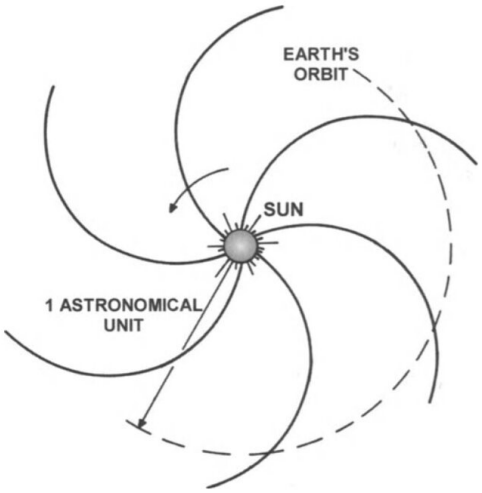

Figure 2.2: Schematic overview of the Sun, and the Parker spiral shape of the IMF in the ecliptic plane. Figure from *Bittencourt* (2004).

sonic (*Frey*, 2007; *Baumjohann and Treumann*, 1996). The Earth has its own magnetic field, which is surrounded by the IMF, thus creating a cavity (magnetosphere) around the Earth. The solar wind observes the Earth's magnetosphere as an obstacle and is slowed down as it approaches the Earth's magnetosphere, after which it gets largely deflected around the magnetosphere. In this process, the Earth's magnetic field gets compressed on the dayside by the solar wind dynamic pressure, P_{dyn}. P_{dyn} is calculated following $P_{dyn} = \rho v^2$, where ρ is the solar wind density and v the solar wind velocity. The typical shape of the Earth's magnetosphere can be observed in Figure 2.3. The magnetopause separates the two different plasma populations. At the transition from supersonic to subsonic speeds, a shock wave is created, known as the bow shock. Here, kinetic energy is converted into thermal energy, heating the plasma and increasing its density. The region between the bow shock and the magnetopause is called the magnetosheath (*Frey*, 2007). An overview of the different regions is shown in Figure 2.3.

Within the Earth's magnetosphere, charged particle motion is governed by the magnetic field, collisions are almost non-existent, and the electrical conductivity is very high. Beneath the magnetosphere, between approximately 60–1000 km altitude, the Earth's ionosphere is located. This region is defined as the partly ionized region of the Earth's upper atmosphere. Ionization is primarily caused by (1) solar extreme ultraviolet (EUV) and (2) energetic particle precipitation, where the latter is only relevant at auroral latitudes.

The ionosphere can be divided into three different layers: (1) D-layer (60–90 km), (2) E-layer (90–150 km), and (3) F-layer (150–1000 km), based on different levels of ion-

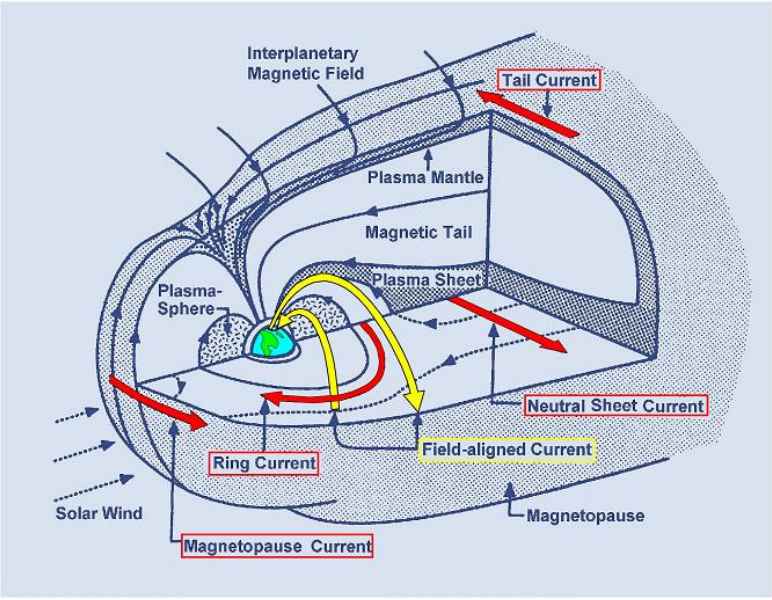

Figure 2.3: Schematic overview of the Earth's magnetosphere with the different regions of the magnetosphere, currents, and plasma regions. Figure adapted from *Kivelson and Russell* (1995).

ization. An example of an ion, electron, and neutral composition during daytime at solar minimum is shown in Figure 2.4. Ionization levels vary with the diurnal cycle, seasonal changes, solar activity, and geomagnetic conditions, which is shown by the typical electron concentrations under various conditions in Figure 2.5.

2.3 Coupling and Current Systems

This section describes how the solar wind, magnetosphere, and ionosphere are coupled together. In addition, the relevant current systems and auroral emissions are addressed.

2.3.1 Solar Wind–Magnetosphere Coupling

When there is a significant angular difference between the IMF vector and the geomagnetic field vector, the ideal MHD conditions that separate the solar wind from the Earth's magnetosphere can break down. Under these circumstances, the magnetic field lines of the IMF and of the Earth's magnetic field can connect to one another in a process called reconnection. As the frozen-in principle breaks down during reconnection,

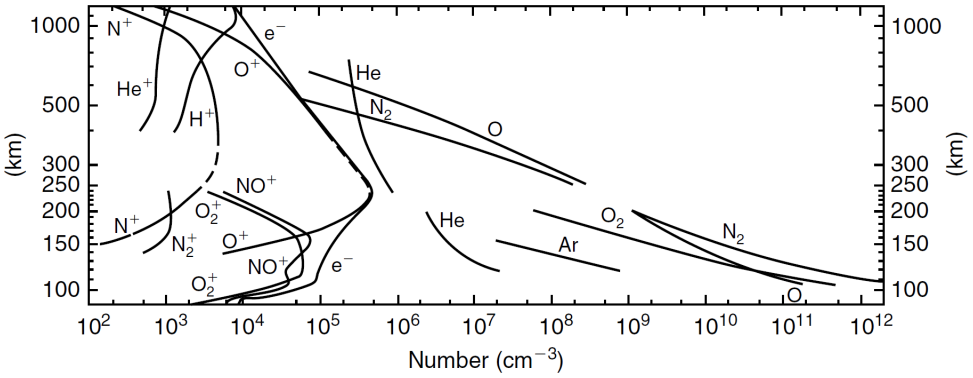

Figure 2.4: Daytime ionospheric and atmospheric composition during the international solar quiet year (1964–1965; solar minimum). Figure retrieved from *Kelley* (2009) and originally published by *Johnson* (1969).

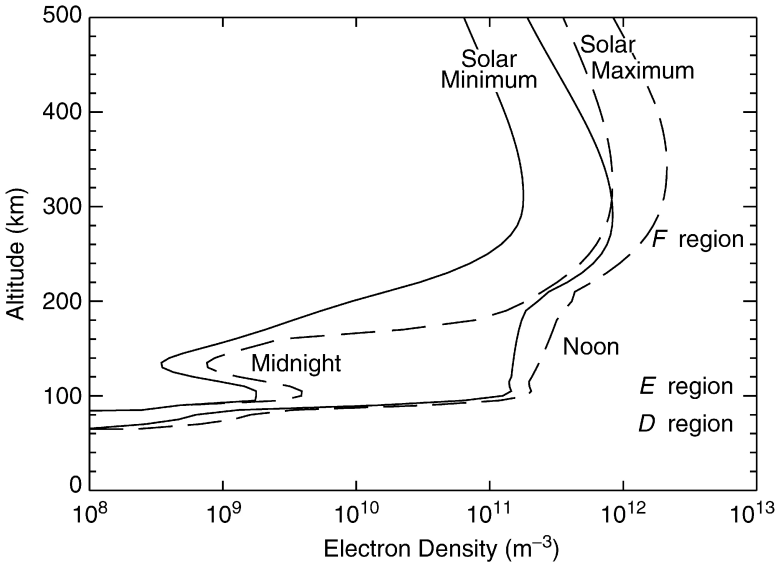

Figure 2.5: Typical electron density profiles during September equinox at noon and midnight for solar minimum and solar maximum. Figure from *Richmond* (2007).

the two plasma populations can mix together, transferring energy and momentum.

This process of magnetic reconnection leads to the formation of open and closed field lines, which are central to understanding the dynamics of the Earth's magnetosphere. Open field lines are connected to the Earth's magnetic field on one side and the IMF on the other, allowing solar wind plasma to enter the magnetosphere by flowing along the field lines. In contrast, closed magnetic field lines are connected to the Earth on both sides, trapping plasma and isolating it from the solar wind. Under southward IMF,

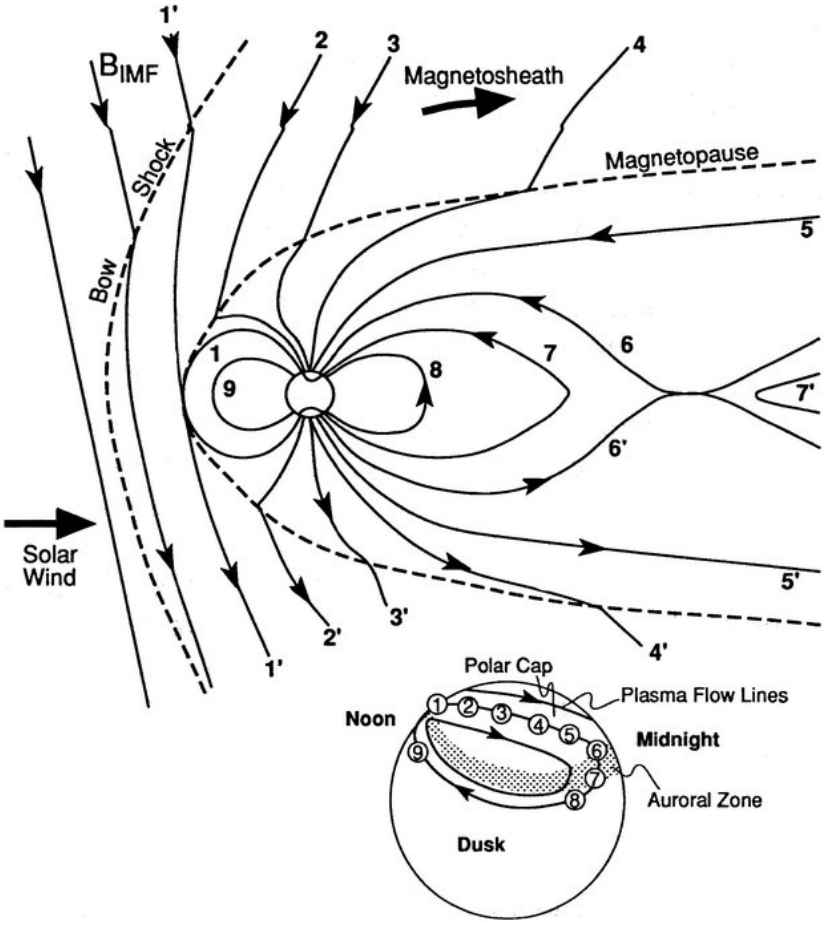

Figure 2.6: Schematic of the Dungey cycle under southward IMF. The numbered magnetic field lines show the sequence of dayside reconnection (1), antisunward transport into the magnetotail (2–5), and tail reconnection (6), after which the closed field lines return to the dayside at lower latitudes (7–9). The inset illustrates the corresponding footpoints of the magnetic field lines in the ionosphere, indicating ionospheric convection, with antisunward flow across the polar cap and sunward return flow at lower latitudes. Figure from *Kivelson and Russell* (1995).

reconnection on the dayside magnetopause creates open field lines that are swept over the polar cap toward the magnetotail by the solar wind. In the tail, those field lines reconnect again, forming closed field lines. This continuous cycle of opening and closing field lines, known as the Dungey cycle, is shown in Figure 2.6 (*Dungey*, 1961). The dayside reconnection happens between the field lines numbered as 1, field lines 2–5 get swept over the poles, after which tail reconnection takes place at 6, and the closed field lines 7–9 are returned to the dayside. During the Dungey cycle, plasma circulation takes place within the magnetosphere and ionosphere, as shown in the inset of Figure 2.6. Energy and momentum can be transported from the solar wind to the magnetosphere along the open magnetic field lines.

2.3.2 Magnetosphere–Ionosphere Coupling

The ionosphere is tightly coupled to the magnetosphere via magnetic field lines. Along these field lines, transfer of energy, momentum, and particles can take place. A manifestation of this transfer are the field-aligned currents (FACs), also known as Birkeland currents, as shown in Figure 2.7. These currents connect the magnetospheric current system as shown in Figure 2.3, to that in the ionosphere. The two main regions of FACs are the Region 1 (R1) and Region 2 (R2) FACs. The R1 currents are located at high-latitude on the poleward side of the auroral oval, and flow into the ionosphere on the dawn side and out of the ionosphere on the dusk side. They are connected to the magnetospheric current system via the high-latitude boundary of the plasma sheet, after which they merge with the neutral sheet current. The R2 currents are located at lower latitudes and show opposite flow directions. They are closed by the westward ring current in the equatorial plane.

2.3.3 Currents in the Ionosphere

The convection formed by the magnetic field lines, as described by the Dungey cycle, causes an electric field, $\boldsymbol{E}_\perp$, perpendicular to the magnetic field, $\boldsymbol{B}$, in the ionosphere. The plasma dynamics, characterized by $\boldsymbol{v}$ and $\boldsymbol{B}$, further result in the flow of electric currents in the ionosphere. The current density, $\boldsymbol{j}$, is given by $\boldsymbol{j} = n_e q_e(\boldsymbol{v_i} - \boldsymbol{v_e})$, where $\boldsymbol{v_{i,e}}$ represents the drift velocity of ions or electrons, respectively. The current density thus depends on the relative motion between the ions and electrons. In the F-region, both ions and electrons predominantly follow the $\boldsymbol{E} \times \boldsymbol{B}$ drift, moving in the same direction with comparable velocities. In contrast, the E-region is characterized by higher neutral densities, causing frequent ion-neutral collisions. These collisions disrupt the $\boldsymbol{E} \times \boldsymbol{B}$

motion of ions, while the lighter electrons remain largely governed by the $\boldsymbol{E} \times \boldsymbol{B}$ drift. The resulting velocity difference between ions and electrons produces horizontal currents, known as the Pedersen and Hall currents. The Pedersen current is in the direction of $\boldsymbol{E}_{\perp}$ and arises from the acceleration of ions and electrons after each collision, whereas the Hall current flows in the $-\boldsymbol{E} \times \boldsymbol{B}$ direction and results from the difference in efficiency of the $\boldsymbol{E} \times \boldsymbol{B}$ drift for ions and electrons. Together, these currents provide the horizontal closure for the FACs entering and leaving the ionosphere, as illustrated in Figure 2.7.

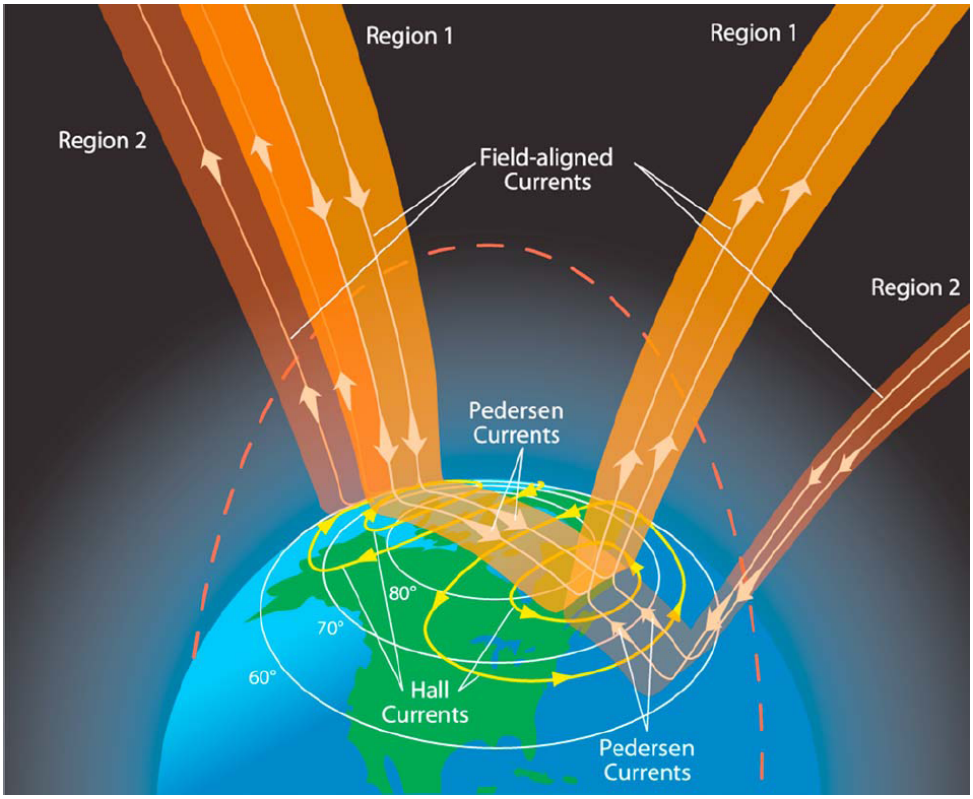

Figure 2.7: 3D schematic representation of the FACs and the ionospheric current systems. Figure from *Le et al.* (2010).

The strength of the currents depends on the conductivity. The conductivity can be divided into the Pedersen conductivity, σ_P, the Hall conductivity, σ_H, and the parallel conductivity, $\sigma_{\parallel}$, which is in the direction of the magnetic field lines. These conductivities are defined as

$$\sigma_p = \frac{eN_e}{B}\left(\frac{\nu_{en}\omega_e}{\omega_e^2+\nu_{en}^2} + \frac{\nu_{in}\omega_i}{\omega_i^2+\nu_{in}^2}\right), \tag{2.13}$$

$$\sigma_H = \frac{eN_e}{B}\left(\frac{\omega_e^2}{\omega_e^2+\nu_{en}^2} - \frac{\omega_i^2}{\omega_i^2+\nu_{in}^2}\right) \tag{2.14}$$

$$\sigma_{\parallel} = \frac{eN_e}{B}\left(\frac{\omega_e}{\nu_{en}} + \frac{\omega_i}{\nu_{in}}\right), \tag{2.15}$$

in which $\omega_{e,i}$ is the gyro frequency of electrons or ions, respectively, and $\nu_{en,in}$ the electron-neutral or ion-neutral collision frequency. The total current density can be expressed as

$$\boldsymbol{j} = \sigma_P \boldsymbol{E'}_{\perp} - \sigma_H \frac{\boldsymbol{E'}_{\perp} \times \boldsymbol{B}}{B} - \sigma_{\parallel} \boldsymbol{E'}_{\parallel}, \tag{2.16}$$

where $\boldsymbol{E'}$ is the electric field in the reference frame of the neutral atmosphere, and $\boldsymbol{E'}_{\parallel}$ is the electric field in the direction of the magnetic field (*Baumjohann and Treumann*, 1996). $\boldsymbol{E'}$ can be linked to the electric field in the fixed frame of reference, which is most commonly the frame of the rotating Earth, via

$$\boldsymbol{E'} = \boldsymbol{E} + \frac{1}{c}\boldsymbol{v_n} \times \boldsymbol{B}, \tag{2.17}$$

where c is the speed of light, and $\boldsymbol{v_n}$ the neutral wind velocity (*Vasyliūnas*, 2012). Without neutral wind, $\boldsymbol{E'} = \boldsymbol{E}$.

2.3.4 Auroral Emission in the Ionosphere

A result of the solar wind–magnetosphere–ionosphere coupling is the precipitation of energetic particles along the magnetic field lines. When the pitch angle is within the loss cone, these particles will deposit their energy in the ionosphere. More energetic particles can penetrate deeper into the ionosphere, depositing their energy at lower altitudes. While descending into the ionosphere, energetic electrons can lose their energy via three pathways:

1. Impact ionization of the neutral atmosphere, increasing the ionospheric plasma density.
2. Excitation of the neutral atmosphere, producing auroral emissions.
3. Heating of ambient electrons in the ionosphere via Coulomb collisions.

Processes (1) and (3) will be discussed in relation to kinetic energy dissipation in Section 2.7.2. The second process excites atoms and molecules, during which a bound electron is excited to a higher energy state.

Auroral emissions are then produced when the excited particle relaxes to a lower energy state via the emission of a photon. The wavelength of the photons, λ, produced due to

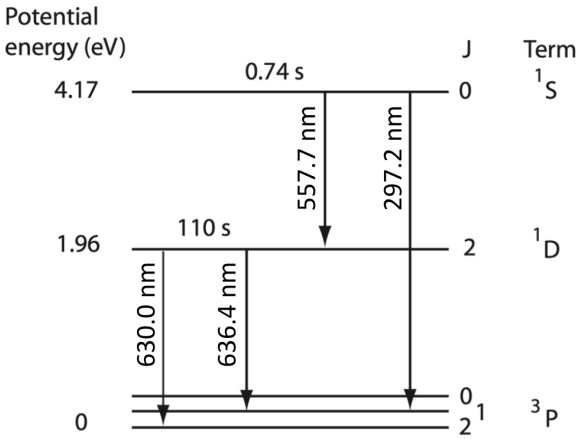

Figure 2.8: The most common emission lines from atomic oxygen. The potential energy (eV) of the different states is given on the left. The J levels represent different sub levels of the excited states (^{1}S and ^{1}D) as well as the ground state (^{3}P). Figure adapted from *Brekke* (2013).

a transition from energy state E_2 to E_1 is given by

$$\lambda = \frac{hc}{E_2 - E_1}, \tag{2.18}$$

where h is Planck's constant and c the speed of light. In this thesis, the 630.0 nm (red) and 557.7 nm (green) emission lines are studied, which are both produced by atomic oxygen. The most common emission lines originating from oxygen atoms, including 630.0 and 557.7 nm, are shown in Figure 2.8. The 630.0 nm emission originates from the transition of atomic oxygen from the metastable O(^{1}D) state to the ground state O(^{3}P). The radiative lifetime of O(^{1}D) is around 110 s (*Witasse et al.*, 1999). At altitudes below 200 km, however, collisions with predominantly N_2 (collisional quenching) shorten the effective lifetime, reducing the observed emission intensity. Consequently, the 630.0 nm emission typically peaks around 240 to 250 km altitude (*Partamies et al.*, 2025). The long lifetime of O(^{1}D) also causes the red aurora to appear diffuse, as atomic oxygen can move in between excitation and photon emission. In contrast, the 557.7 nm emission originates from the transition from O(^{1}S) to O(^{1}D). With a much shorter lifetime of about 0.7 s (*Kawamura et al.*, 2020), this transition produces sharper, intenser, more structured, and more dynamic auroral features. Collisional clenching of O(^{1}S) is only significant at lower altitudes (*Hunten and McElroy*, 1966), while at altitudes above 150 km, the decreasing atomic oxygen density (see Figure 2.4) limits the overall intensity. Depending on local time, location, and geomagnetic conditions, the peak emission altitude can vary. Above Svalbard, we have used 120 km in the dawn and dusk sectors (*Partamies et al.*, 2022).

2.4 MHD Wave Theory

The MHD theory can be used to describe wave motion from small perturbations in pressure as well as magnetic and electric fields (*Kivelson and Russell*, 1995). A general wave field can be described as

$$Ae^{i(\omega t - \boldsymbol{k}\cdot\boldsymbol{r})}, \tag{2.19}$$

where A is the wave amplitude given by a complex constant, $\boldsymbol{r}$ the position vector, ω the angular frequency that relates to the frequency, f, as $\omega = 2\pi f$, and $\boldsymbol{k}$, the wavenumber. $\boldsymbol{k}$ is related to the wavelength λ of the wave following $\boldsymbol{k} = 2\pi/\lambda\hat{k}$, where $\hat{k}$ is the unit vector in the wave propagation direction. When $\omega^2 > 0$, the system will try to restore its equilibrium after a perturbation, resulting in waves. When $\omega^2 < 0$, any displacement from equilibrium will only grow, thus resulting in instabilities. Following Equation 2.19, a solution will oscillate with frequency f in time at a fixed spatial location, or, at a fixed time, any solution will oscillate with wavelength λ in space except at the wave phase velocity $v_{ph} = \omega/k$ (*Kivelson and Russell*, 1995). The phase velocity of a wave gives the velocity with which the phase fronts advance. The wave energy is carried by a different velocity, the group velocity, which is given by $v_g = d\omega/dk$. In dispersive media, the phase and group velocities can differ significantly, and the direction of energy propagation (the group velocity vector) may not align with the direction of the wavefronts (the phase velocity vector).

To understand how the different wave modes propagate in a medium, we must derive the dispersion relation, $\omega(\boldsymbol{k})$. To do this, we must linearize the system in terms of a steady state, x_0, and perturbation component, x_1, where $x_0 \gg x_1$. The main variables that describe the system now become

$$\boldsymbol{B} = \boldsymbol{B_0} + \boldsymbol{b} \tag{2.20}$$

$$\boldsymbol{v} = \boldsymbol{v_0} + \boldsymbol{v_1} \tag{2.21}$$

$$\rho = \rho_0 + \rho_1 \tag{2.22}$$

$$p = p_0 + p_1, \tag{2.23}$$

where $\boldsymbol{B_0}$ is the background magnetic field, and $\boldsymbol{b}$ the magnetic field perturbation. This linearization is then applied to Maxwell's equations and the conservation laws. More specifically, the continuity equation (Eq 2.8), the equation of motion (Eq 2.9), in which $\boldsymbol{j}$ has been substituted by $\boldsymbol{j}$ from Ampère's law (Eq 2.5), Faraday's law (Eq 2.4), in which $\boldsymbol{E}$ has been substituted by $\boldsymbol{E}$ in the frozen-in principle (Eq 2.11), and the equation of state (Eq 2.12) are used. Under the assumption of a plane wave solution (Eq 2.19),

the general dispersion relation for MHD waves propagating in a uniform plasma with a background magnetic field vector, $\boldsymbol{B_0}$, can then be defined by

$$(\omega^2 - \boldsymbol{k}^2 v_A^2 \cos^2\theta)[\omega^4 - \omega^2 \boldsymbol{k}^2 (c_s^2 + v_A^2) + \boldsymbol{k}^4 v_A^2 c_s^2 \cos^2\theta] = 0, \tag{2.24}$$

where θ is the angle between $\boldsymbol{k}$ and $\boldsymbol{B_0}$, c_s the speed of sound, and v_A the Alfvén speed. c_s is defined by $c_s^2 = \gamma p/\rho$, where p and ρ are the pressure and mass density, respectively, and γ the adiabatic index. The Alfvén speed, which describes the speed at which waves in a plasma can transport magnetic signals, is defined as $v_A = \sqrt{B^2/\mu_0\rho}$ (*Baumjohann and Treumann*, 1996).

The two solutions to the dispersion relation, Equation 2.24, then represent two different wave modes: the Alfvén mode and the magnetoacoustic mode. The Alfvén dispersion relation reads

$$\frac{\omega^2}{\boldsymbol{k}^2} = v_A^2 \cos^2\theta, \tag{2.25}$$

while the magnetoacoustic dispersion relation is given by

$$\frac{\omega^2}{\boldsymbol{k}^2} = \frac{c_s^2 + v_A^2}{2} \pm \frac{1}{2}[(c_s^2 + v_A^2)^2 - 4c_s^2 v_A^2 \cos^2\theta]^{1/2}. \tag{2.26}$$

Equation 2.25 describes the shear Alfvén mode or simply Alfvén mode. It is also known as the transverse mode. The $\cos\theta$ term illustrates that the wave cannot propagate perpendicular to the background magnetic field and must therefore move along the magnetic field lines. Shear Alfvén waves cause the magnetic field lines to bend, while not changing the plasma density or pressure, and are thus called incompressible waves. The displacement of the wave is perpendicular to $\boldsymbol{B_0}$ and the distance between the perturbed field lines remains constant. Energy transfer by ULF waves can be described by the Poynting vector,

$$\boldsymbol{S} = \frac{1}{\mu_0}[\boldsymbol{E} \times \boldsymbol{b}]. \tag{2.27}$$

In case of Alfvén mode waves, $\boldsymbol{S}$ is restricted to the field-aligned direction. The polarization of the Alfvén wave, and the co-directionality of background magnetic field and Poynting vector, are schematically shown in Figure 2.9a.

Equation 2.26 describes the fast (positive sign) and slow (negative sign) magnetoacoustic waves, which are also know as longitudinal waves. Contrary to Alfvén waves, magnetoacoustic waves are compressible, thus changing the plasma density and magnetic field magnitude, and can move in any direction with respect to the background magnetic field. Since the wave perturbations happen oblique to $\boldsymbol{B_0}$, the spacing between the magnetic field lines becomes non uniform. For better understanding, we can split these modes into two limits: propagation parallel ($\theta = 0$) and perpendicular ($\theta = \pi/2$) to the background

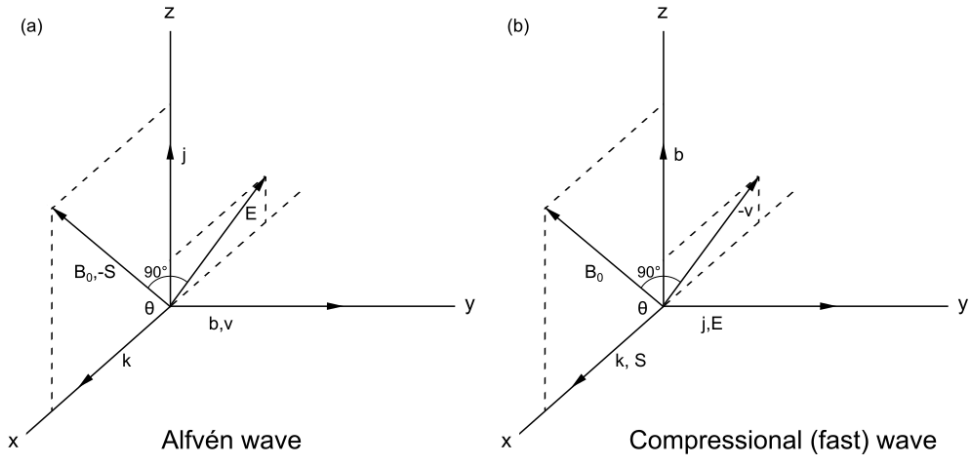

Figure 2.9: Schematic representation of wave polarization directions for (a) Alfvén waves, and (b) compressional (fast) waves. Figure is based on *Kivelson and Russell* (1995).

magnetic field. For parallel propagation, the fast mode behaves like an Alfvén wave (e.g. $v_{ph} = \pm v_A$), while the slow mode propagates at the sound speed (e.g. $v_{ph} = \pm c_s$). For perpendicular propagation, the fast mode speed is $v_{ph} = \pm\sqrt{v_A^2 + c_s^2}$, while the slow mode speed goes to 0. Fast mode waves can transport energy in all directions, and thus not exclusively in the direction of $\boldsymbol{B_0}$, which is indicated in the schematic wave polarization in Figure 2.9b. Omnidirectional energy transport is indicated by a finite fast mode group velocity in all directions, while being largest perpendicular to the background magnetic field. The energy transport of slow modes is restricted in directions close to field-aligned, defined as "field-guided". In a uniform medium, the different wave modes are decoupled. However, non-uniformities can lead to coupling between the different wave modes. In the context of this work, we ignore the slow mode, since it is only relevant in warm plasmas.

2.5 Alfvén Waves and Field Line Resonances

Alfvén waves propagate along the magnetic field lines and, within the Earth's magnetosphere, the geomagnetic field and the ionosphere provide unique boundary conditions for these Alfvén waves. The field lines act as natural waveguides and the northern and southern ionospheres, due to their large conductivities, can cause reflection. This reflection can lead to the formation of standing Alfvén waves on geomagnetic field lines. However, Alfvén waves only satisfy the reflection criteria for certain wavelengths. If the length of the magnetic field line connecting the two ionospheres is given by l, the allowed

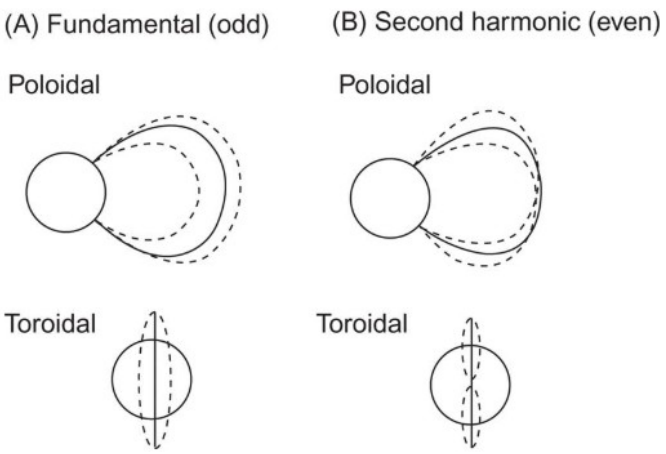

Figure 2.10: A schematic representation of (A) fundamental (odd) and (B) second harmonic (even) standing oscillations on magnetic field lines for toroidal and poloidal modes. The dashed lines represent the displaced field lines. Figure from *Menk and Waters* (2013).

wavelengths along the field direction, $\lambda_{||}$, are given by

$$\lambda_{||} = 2l/n \tag{2.28}$$

where n is an integer corresponding to different harmonics. The allowed frequencies for resonant standing Alfvén wave modes, which form field line resonances (FLRs), are then given by

$$f = \frac{nv_A}{2l} = \frac{nB}{2l\sqrt{\mu_0\rho(l)}}, \tag{2.29}$$

where v_A is the Alfvén velocity. The possible resonant frequencies thus depend on the magnetic field strength, the length of the field line and the plasma density distribution (*Kivelson and Russell*, 1995).

The two lowest harmonics, the fundamental and second harmonic modes, in a dipolar magnetic field are depicted in Figure 2.10. Here, a distinction has been made between two different polarization modes: toroidal and poloidal, which describe the oscillation direction relative to the magnetic field. The toroidal mode is characterized by magnetic (electric) field oscillations primarily in the azimuthal (radial) direction, while poloidal waves have have their perturbations in opposite direction.

The azimuthal wave number gives the number of wave cycles that fit around the Earth. m is thus defined as the phase change of the wave per degree of magnetic longitude,

$m = \frac{\Delta\phi}{\Delta\lambda_{az}}$ and can be calculated following

$$m = \frac{2\pi \mathrm{L} R_E}{\lambda_{az}}, \tag{2.30}$$

where L is the L-shell number, R_E the Earth radius, and λ_{az} the azimuthal wavelength. The L-shell number is defined by how far from Earth, given in Earth radii, R_E, magnetic field lines cross the magnetic equator. Waves can be classified according to their m number, where low-m waves have large spatial scales and are predominantly toroidally polarized. High-m waves have small spatial scales and show poloidal polarization. Waves are generally considered high-m when $m > 15$ (*Yeoman et al.*, 2010), but in other cases even higher values such as $50 < m < 150$ are used for the high-m classification (*Mager et al.*, 2019; *Michael et al.*, 2024). Low-m waves typically have m numbers between 1–10 and include FLRs, which are most effectively driven by fast mode waves when $m \approx 3$ (*Menk and Waters*, 2013; *Rubtsov et al.*, 2018). In between low-m and high-m was, there is a class of intermediate-m waves ($10 \lesssim m \lesssim 15$), which can show characteristics of either low-m or high-m waves (*Mager et al.*, 2019). In addition, waves often show a mixed polarization, and waves can transition between different polarization states (*Yeoman et al.*, 2010).

2.6 Ultra-low Frequency Waves

ULF waves can be described by MHD wave theory. These waves arise from small perturbations in the plasma and magnetic field and can appear as Alfvén waves, fast and slow magnetoacoustic waves as described by the general MHD wave framework in Section 2.4. ULF waves have frequencies between 1 mHz–5 Hz and can be categorized into continuous pulsations (Pc), with a sinusoidal waveform, and irregular pulsations (Pi), with an irregular waveform, where both have subcategories based on wave periodicity (*Jacobs et al.*, 1964). The different categories are shown in Table 2.1. In this thesis, we focus on waves in the Pc5 and Pc6 bands, which are particularly relevant for FLRs as their frequencies align with the natural eigenfrequencies of the Earth's magnetic field lines.

2.6.1 Sources of ULF Waves

The ULF wave generation mechanisms are usually divided into internal and external to the Earth's magnetosphere. Traditionally, large-scale (low-m) waves are associated with external sources, while more localized, smaller-scale (high-m) waves are associated

Category	Period [s]	Frequency
Pc1	0.2–5	0.2–5 Hz
Pc2	5–10	0.1–0.2 Hz
Pc3	10–45	22–100 mHz
Pc4	45–150	7–22 mHz
Pc5	150–600	1.7–7 mHz
Pc6	>600	< 1.7 mHz
Pi1	1–40	0.03–1 Hz
Pi2	40–150	7–25 mHz
Pi3	> 150	< 7 mHz

Table 2.1: Classification of ULF waves according to *Jacobs et al.* (1964). The Pc6 and Pi3 have been added later (*Saito*, 1978).

with internal generation mechanisms (*Mager et al.*, 2015). External sources include solar wind dynamic pressure pulses on the dayside of the magnetosphere or the Kelvin-Helmholtz instability (KHI), which arises due to velocity shear flows on the flanks of the magnetopause. These external sources can excite fast waves at the magnetopause due to local variations in the system's total pressure, which are then mitigated by the compressional fast mode waves (*Kivelson and Russell*, 1995). These compressional waves can excite FLRs when the frequency of the fast mode matches the local Alfvén frequency of a given magnetic field line. During this coupling, the energy from the fast mode is resonantly transferred into the L-shell corresponding to the FLR.

Internal sources, on the other hand, result from instabilities and kinetic processes within the magnetosphere itself, such as wave-particle interactions (*Mager et al.*, 2015). For internal generation to be possible, an energetic particle population needs to be present in order to be able to excite a ULF wave. The waves are then localized to this population. Possible wave-particle interaction processes include drift-resonance, and drift-bounce resonance. Alternatively, magnetospheric instabilities such as substorm-associated reconnection can also generate ULF waves.

2.7 Energy Exchange

When assuming an infinite conductivity in the ionosphere, the foot points of the magnetic field are fixed with respect to the plasma, such that standing ULF waves are fully reflected. In reality, the ionospheric conductivity is finite, and the wave reflection is only partial. The reflection coefficient, r, is given by

$$r = \frac{\Sigma_A - \Sigma_P}{\Sigma_A + \Sigma_P}, \tag{2.31}$$

in which Σ_A is the Alfvén wave conductance and Σ_P the height-integrated Pedersen conductance (*Wang et al.*, 2020). For a given Alfvén wave, the reflection coefficient depends on the Pedersen conductance, which modifies how efficiently the wave energy couples into the ionosphere. Consequently, a fraction of the incoming Poyning flux is absorbed rather than reflected, leading to energy dissipation into the ionosphere. Observations indicate that typical reflection levels reach approximately 97% on the dayside and 40–70% on the nightside, depending on the level of solar activity and the associated conductivity changes (*Hughes and Southwood*, 1976). The unreflected component of the wave gradually dissipates energy into the ionosphere via Joule heating, resulting in damping of the standing ULF waves (*Hartinger et al.*, 2015).

Looking at energy dissipation in a more general sense, energy enters the ionosphere-thermosphere system in two forms, namely electromagnetically and kinetically. The electromagnetic (EM) flux is carried by the Poynting flux, and the kinetic flux by the precipitating particles (*Huang*, 2021).

2.7.1 Electromagnetic Energy Flux

The EM contribution is described by the Poynting theorem:

$$\nabla \cdot \boldsymbol{S} + \frac{\partial W}{\partial t} = -\boldsymbol{j} \cdot \boldsymbol{E}, \tag{2.32}$$

where $\boldsymbol{S}$ is the Poynting vector as defined in Equation 2.27 (Section 2.4), W the EM energy density, $\boldsymbol{j}$ the current density, as defined in Equation 2.16 (Section 2.3.3). $\nabla \cdot \boldsymbol{S}$ represents the divergence of EM energy, $\frac{\partial W}{\partial t}$ the local change in EM energy, and $\boldsymbol{j} \cdot \boldsymbol{E}$ is the energy source. In this thesis, we study ULF waves in the Pc5 and Pc6 range and their energy dissipation into the ionosphere. In the ionosphere, the quasi-static approximation is valid for these waves and $\frac{\partial W}{\partial t}$ can be neglected as the wavelength of ULF waves is much larger than the electron inertial length and their frequency exceeds the ion gyro frequency (*Verkhoglyadova et al.*, 2018). The energy dissipation is thus dominated by $\boldsymbol{j} \cdot \boldsymbol{E}$.

In the ionosphere, this EM energy conversion is generally referred to as Joule heating, which in the neutral frame can be approximated by

$$\boldsymbol{j} \cdot \boldsymbol{E'} \approx \sigma_p E'^2, \tag{2.33}$$

where E' is the electric field perpendicular to the magnetic field in the frame of reference of the neutral gas, and σ_p the Pedersen conductivity, as given by Equation 2.13 (*Brekke*,

2013; *Thayer and Semeter*, 2004). An equivalent description can be given in terms of frictional heating, where collisions between ions and neutrals dissipate wave energy as thermal energy:

$$\frac{\delta E_n}{\delta t} = \frac{3k_B}{m_n} \sum_i N_i m_i \nu_{in} (T_i - T_n), \tag{2.34}$$

where E_n is the energy of the neutral species, k_B the Boltzmann constant, N_i, m_i, and T_i, respectively the number density, mass, and temperature of the ion species i, ν_{in} is the ion-neutral collision frequency, and m_n and T_n are the mass and temperature of neutral species n. Here, Maxwellian molecular interactions have been assumed as well as a balance between the energy exchange term and the frictional heating, $\frac{\partial E_i}{\partial t} = 0$, which is reasonable below approximately 400 km. Although framed differently, and applicable to different altitude ranges, Joule and frictional heating both quantify the rate at which EM energy is converted into mechanical energy (*Strangeway*, 2012; *Vasyliūnas*, 2005).

2.7.2 Kinetic Energy Flux

The kinetic energy flux, on the other hand, consists largely of precipitating energetic particles and can be divided into two separate populations: low energy ($\leq$ 100 eV) and high energy ($\geq$ 100 eV). The high energy population can deposit their energy through ionization, while the low energy population can cause heating of ambient electrons via Coulomb collisions. These correspond to processes (1) and (3) mentioned in Section 2.3.4. Energy dissipation through ionization is described by

$$Q_p(z) = W_{ion} \alpha_{eff}(z) N_e^2(z), \tag{2.35}$$

where Q_p is the deposited energy in [W m^{-3}], W_{ion} is the average energy per ion-electron pair produced, α_{eff} is the effective recombination coefficient in [m^3 s^{-1}], and N_e the electron density [m^{-3}]. W_{ion} is approximately 35.5 eV between 80–200 km altitude (*Thayer and Semeter*, 2004).

The low energetic flux ($\leq$ 100 eV), sometimes referred to as soft precipitation (*Lynch et al.*, 2007), can contribute to general thermal heating. This energy is deposited at higher altitudes via Coulomb collisions and thermal conduction. Due to the lack of energy sinks at higher altitudes, low energetic electrons can yield large increases in electron temperature (*Lynch et al.*, 2007).

2.7.3 Ion Outflow and Upflow

The transport of energy and momentum makes ULF waves an important contributor in the coupling between the ionosphere and magnetosphere. Another crucial link for this coupling is ion outflow, a major source for the magnetospheric plasma (e.g. *Schunk*, 2000; *Bjoland et al.*, 2025). Both light thermal ions (H^+ and He^+) and heavy ions (mainly O^+, but also N^+, NO^+, O^+_2, and N^+_2) originating from the ionosphere can populate the plasma sheet and magnetotail, altering mass density, Alfvén velocity, and consequently the magnetic reconnection rate and location (*Zhang and Brambles*, 2021). Understanding the mechanisms that lift ionospheric plasma into the magnetosphere–beginning as ion upflow and sometimes evolving into ion outflow–is thus essential for characterizing the coupled magnetosphere–ionosphere system.

The polar wind represents a quasi-steady, low-energy ion upflow from the polar ionosphere, consisting primarily of light ions (H^+, He^+), thermal O^+ and electrons, moving along open magnetic field lines that connect the high-latitude polar regions to the magnetosphere. This process is driven by a pressure gradient that accelerates electrons upward, generating an ambipolar electric field in the process due to the separation of electrons and ions. This ambipolar electric field then accelerates the ions upward. Other forces (i.e. the pressure gradient force, gravitational force, and upward mirror force) also contribute to the outflow (*Schunk and Nagy*, 2009; *Huang*, 2021).

Except for the outflow of H^+, most ion outflow needs an additional energization source, such as frictional heating or solar EUV, among others. Therefore, these types of outflow are known as energetic ion outflow. During geomagnetically active conditions, heavier ions, such as O^+, can be accelerated leading to ion upflow and, in some cases, outflow. The two main categories of energetic ion upflow are identified based on whether ion or electron heating dominates (*Wahlund et al.*, 1992). Type 1 ion upflow occurs when direct ion heating drives the process. Heating mechanisms include wave-particle interactions, ion-neutral frictional heating, and Joule heating. Enhanced ion temperature increases the pressure gradient, reinforcing the ambipolar electric field, resulting in uplifting ions. Furthermore, type 1 upflow is characterized by a low electron densities below 300 km, indicating a lack of energetic particle precipitation (*Wahlund et al.*, 1992). Type 2 upflow is dominated by enhanced electron temperatures and electron densities in the E- and F-region.

The difference between upflow and outflow is primarily energetic. Upflow denotes ions lifted within the topside ionosphere, but still gravitationally bound, while outflow refers to ions that have gained enough energy to escape along the open field lines into the magnetosphere.

Chapter 3

Data and Instrumentation

In this chapter, we provide an overview of the instruments, datasets, and inversion models employed throughout this thesis. Instrumentation includes the European Incoherent SCATter (EISCAT) radars, the meridian scanning photometer, auroral imaging systems operating both from the ground and from space, as well as ground- and space-based magnetometers. In addition, data from other satellite missions are utilized. For each instrument, its key characteristics and limitations are briefly discussed.

3.1 EISCAT Radars

The European Incoherent SCATter (EISCAT) radars are a type of incoherent scatter radar located near Tromsø and in Svalbard. The word radar stands for radio detection and ranging and is defined as a system that transmits an electromagnetic wave from a transmitter station, Tx, and subsequently, after the signal is reflected from the target, receives the reflected pulse at a receiver station, Rx. When the transmitter and receiver station are co-located, the system is called monostatic. Otherwise, the system is bistatic or multistatic in case of multiple receivers. In our case, all radars are used in monostatic configuration. Basic properties that can be deduced from a simple radar system include (1) range also known as distance to the target, (2) backscatter power, and (3) Doppler shift of the received signal. Backscatter power gives information about the target, while the Dopper shift can be related to the line-of-sight velocity of the target along the radar beam (*Dougherty and Farley*, 1960; *Farley*, 1969; *Evans*, 1969).

3.1.1 Incoherent Scatter Radars - Working Principle

ISRs transmit high-power radio waves into the ionospheric plasma. By deriving the back-scattered signal, ISRs can derive key plasma parameters such as electron density, ion and electron temperatures, and ion velocity. The primary scattering targets for ISRs are electrons in the ionosphere (*Evans*, 1969). When an ISR pulse encounters ionospheric plasma, electrons are accelerated by the incident electric field and this energy is re-radiated as dipole radiation, known as Thomson scattering. This Thomson scattering happens by the electrons. However, since electron motion in the ionosphere is governed by ions, the back-scattered signal is dominated by ion behavior. Electrostatic wave modes (ion acoustic modes), which occur naturally in the plasma, determine the motion of the ions (*Dougherty and Farley*, 1960).

In order to get the signal of the electron cloud surrounding the ions, the radar wavelength, λ_r, which depends on the radar frequency, needs to be chosen with respect to the Debye length, λ_D, of the ionospheric plasma. The Debye length defines the scale over which the gas is quasi-neutral. At scales smaller than the Debye length, individual charges can be observed. An EM pulse with $\lambda_r << \lambda_D$ thus scatters from individual free electrons which are shielding the ion, rather than general behavior influenced by ion dynamics. However, in case $\lambda_r >> \lambda_D$, the signal scatters from the electron cloud thus giving the collective behavior of the plasma that is governed by ion motion. ISRs are thus designed in such a way that $\lambda_r >> \lambda_D$ (*Evans*, 1969; *Schunk and Nagy*, 2009).

Thomson scattering happens isotropically, meaning that the power is uniformally spread across the surface of a sphere of which only a fraction is directed back towards the receiver (*Evans*, 1969). In addition, only a very small percentage of the incoming power is scattered from the electron cloud in the first place. ISRs thus require a very powerful beam in order to receive enough back-scatter power. To create such a beam, ISRs are designed to focus their power into a narrow beam rather than emit power isotropically, also known as antenna gain. The antenna gain is achieved by using a specific antenna design such as a cassegrain dish or a parabolic cylinder, which require manual movement in order to steer the direction of the beam. More modern radar designs use phased array configurations, allowing electronic signals to alter beam directionality. The directionality of the radar is given by azimuth and elevation angle. Azimuth gives the angle of the radar, where 0° corresponds to geographic north and positive degrees are measured clockwise from there. Elevation gives the angle of the dish from the horizontal and ranges from 0°–90°, where 90° elevation corresponds to looking straight up.

3.1.2 EISCAT Radars in this Thesis

Throughout this thesis, EISCAT radars in Tromsø (ultra-high frequency (UHF) and very-high frequency (VHF)) and Svalbard have been used. The antennae are shown in Figure 3.1.

Figure 3.1: Pictures of the EISCAT radars used in this thesis: a) EISCAT Svalbard radar 42m, b) EISCAT Svalbard radar 32m, c) Tromsø UHF, and d) Tromsø VHF. Photos taken by Katie Herlingshaw.

Tromsø VHF Radar

The Tromsø VHF radar is located at 69.58°N, 19.23°E in geographic coordinates. The VHF radar, as shown in Figure 3.1d, has a parabolic cylinder antenna design that mea-

sures 120 by 40 m and operates at 224 MHz. In Paper I, a newly developed detection algorithm is applied to data from the VHF radar, while it points northward in low elevation.

Tromsø UHF Radar

Co-located with the VHF radar, we find the UHF radar. The UHF radar consists of a fully steerable 32 m cassegrain dish, as shown in Figure 3.1c, and operates at 931 MHz. Paper I uses its data, though not shown in the paper, while the radar is aligned in the direction of the magnetic field.

EISCAT Svalbard Radar

Paper III utilizes the EISCAT Svalbard Radar (ESR), taking advantage of its co-location with the meridian scanning photometer at the Kjell Henriksen Observatory (KHO). The ESR is located 600 m north of KHO. The ESR system comprises two cassegrain dish antennae, a fully steerable 32 m (Figure 3.1b) and a stationary 42 m aligned with the Earth's magnetic field (Figure 3.1a). The ESR operates with a frequency of 500 MHz. Paper III uses the field-aligned 42 m antenna.

3.1.3 Ion Line Spectrum

A typical power spectrum from ionospheric plasma, referred to as the ion line, shows a double humped spectrum in the F-region of the ionosphere as shown in Figure 3.2. Figure 3.2 indicates the dependence of the shape of the power spectrum on plasma parameters such as electron density, N_e, electron and ion temperature, T_e and T_i, and the ion line-of-sight velocity, v_i (*Evans*, 1969; *Farley*, 1969). More specifically, N_e can be derived from the received back-scattered power, and the difference between the peaks of the power spectrum depends on T_e and T_i, but when $T_e/T_i \sim 1$, which is the case in the E-region ionosphere, they become indistinguishable. Furthermore, the width of the spectrum gives the $(T_e + T_i)/m_i$ ratio, and the Doppler shift of the peaks can be used to determine v_i (*Grydeland et al.*, 2004).

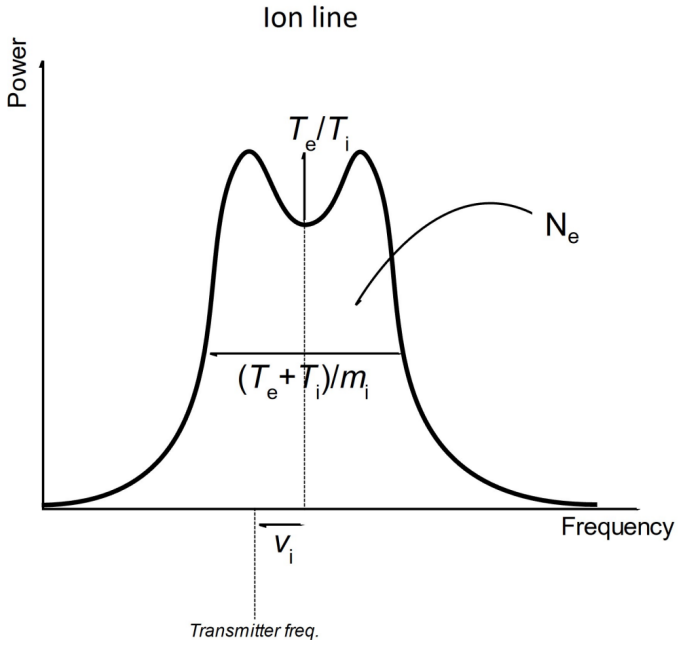

Figure 3.2: A typical incoherent scatter power spectrum for the ion line. Figure from *Tjulin et al.* (2024), retrieved July 10, 2025.

3.1.4 Data Analysis

EISCAT data is analysed using the Grand Unified Incoherent Scatter Design and Analysis Package (GUISDAP) software tool (*Lehtinen and Huuskonen*, 1996). First, the incoming received signal is converted into a complex receiver voltage. This signal is a complex valued normal distributed random variable according to the central limit theorem. Subsequently, an autocorrelation function is estimated, which can be related to the ion line spectrum via a Fourier transform. GUISDAP then finds the values of the ionospheric plasma parameters by iteratively fitting all parameters to the autocorrelation function. Because incoherent scattering is inherently stochastic, reliable parameter estimation requires averaging over a sufficiently large number of independent samples. Moreover, the electron density needs to be high enough to produce a detectable signal-to-noise ratio (SNR), ensuring that the derived plasma parameters are physically meaningful.

The received radar signal also includes backscatter signals from unwanted targets (e.g. spacecraft, mountains, space debris). In our case, range gates which includes these signals are removed before the ionospheric plasma parameters are fitted. In addition, the received signal also includes noise from system electronics and antenna sidelobes among others. The noise level is measured using the SNR, which is defined as the ratio

between the target signal power and the mean noise power. In order to reduce the SNR, the signal is typically integrated over 1 min periods.

3.1.5 Limitations

Since ISRs use electrons to scatter from, we need to have a sufficiently large electron density to obtain an adequate SNR. Because scattering is a stochastic process, many independent samples must be averaged to build up a statistically meaningful autocorrelation function. This requirement limits the temporal resolution of ISR measurements, while at the same time the fitting process of the ion line spectrum assumes homogeneity and stationarity over the entire scattering period and volume (*Grydeland et al.*, 2004). While these conditions are fulfilled during quiet conditions, the plasma can be out of thermal equilibrium during disturbed conditions, resulting in an asymmetric ion spectrum which is not suitable for fitting the plasma parameters.

The data analysis performed by GUISDAP, furthermore, relies on iteratively fitting a modeled autocorrelation function to the observed signal. This process requires a model ionosphere around which the parameters are adjusted during the fitting. As shown by *Virtanen et al.* (2024), this dependency can introduce systematic uncertainties. In particular, the assumed ion composition can deviate from reality, and the transition from molecular to atomic oxygen can occur at a different altitude than previously assumed. Since the ion line spectrum shape depends heavily on the ion mass, this affects the ion and electron temperatures, among others.

Another limitation comes from the limited beam size. This only gives us the ionospheric conditions within a limited field-of-view (FOV), thus requiring assumptions if we want to extrapolate the radar data outside of the FOV.

3.2 Meridian Scanning Photometer

The meridian scanning photometer (MSP) measures auroral intensities along the geomagnetic meridian using a rotating mirror which scans from geomagnetic north to south. The mirror reflects the incoming light towards six channels, allowing it to measure the intensity of up to six different wavelengths at the same time. These channels record the wavelength as a function of elevation angle. Each channel consists of an interference filter, a filter tilting mechanism, optics to focus the incoming light, and a photomultiplier tube (PMT), which is located inside a cooling unit to minimize thermal noise.

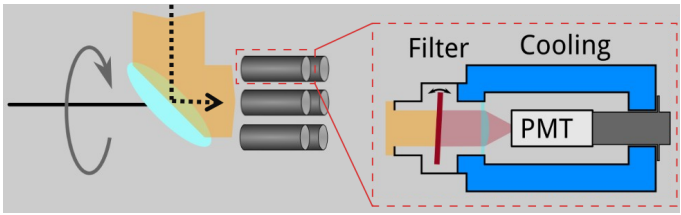

Figure 3.3: Schematics of the MSP. The incoming light (black arrow) is reflected onto six channels by a rotating mirror. Each channel consist of an interference filter located inside a filter tilting mechanism, and optics to focus the incoming light onto a PMT. The PMTs are located within a cooling unit. Behind the PMT, a detector is located. Image credits belong to Pål Gunnar Ellingsen.

A schematic representation of the MSP setup is shown in Figure 3.3, while a picture of the instrument can be found in Figure 3.4. As the interference filters are not inside temperature-controlled enclosures, the filter tilting unit can adjust the filter angle to account for changes in room temperature that can shift the center wavelength of the filter passband. A "tilt angle" calibration is regularly carried out to counteract the effects of temperature changes. In order to preserve the photomultiplier tubes, the MSP only runs when the sun is at least 10° below the horizon.

The absolute calibration of the instrument is carried out using a built-in low-level light source. This calibration converts the intensity from the number of counts to the unit Rayleigh [R]. Generally, the absolute calibration is carried out at least once a year.

The instrument used in this thesis is located at KHO, Longyearbyen, Svalbard (*Herlingshaw et al.*, 2025). Its FOV is shown in Figure 3.5a, assuming an emission height of 250 km (120 km) for 630.0 nm (557.7 nm) emission. Since its placement at KHO in Autumn 2007, the instrument has always recorded at wavelengths 427.8 nm, 557.7 nm, and 630.0 nm, while the recorded wavelengths of the other channels have varied. In this thesis, the 630.0 nm channel is central, while we also use the 557.7 nm wavelength. Specifically in Paper II, we use 17 seasons of MSP data, from season 2007/2008–2023/2024, where each seasons runs from early November to late February. The temporal resolution of the MSP has increased from 16 s (up to 11 October 2016) to 8 s currently.

The MSP data is visualized using a keogram format, where time is displayed on the x-axis and the elevation angle (or magnetic latitude) on the y-axis. An elevation of 0° corresponds to north, 90° to zenith (straight up) and 180° to south. An example keogram is shown in Figure 3.5b, where the left y-axis corresponds to the elevation angle and the right y-axis to magnetic latitude.

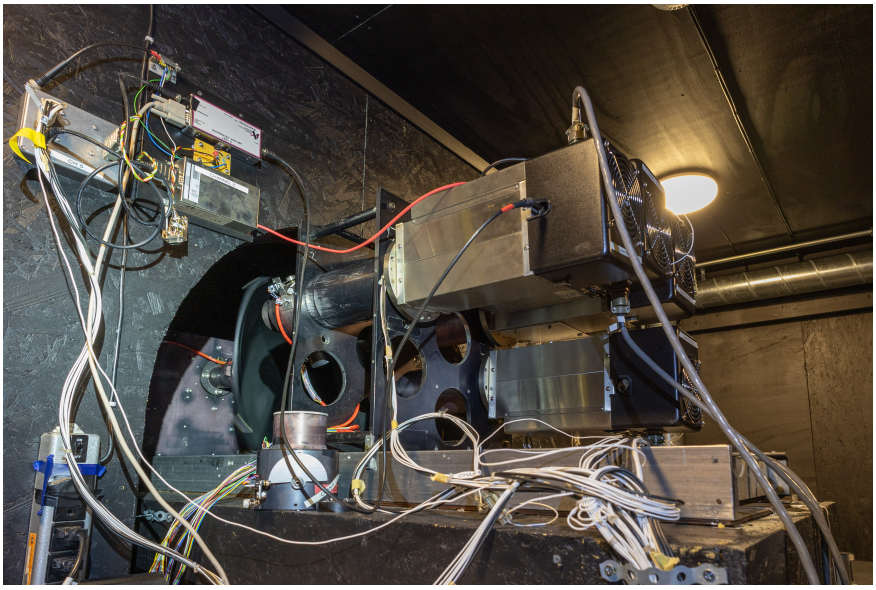

Figure 3.4: A picture of the MSP at KHO. The rotating mirror with its rotating mechanism behind it is visible on the left inside the arch. In front of the mirror, the filters and optics are located within the tubes. The PMTs are within the cooling units that have fans on the back. In the picture, four channels are in use. Picture taken by Mikko Syrjäsuo.

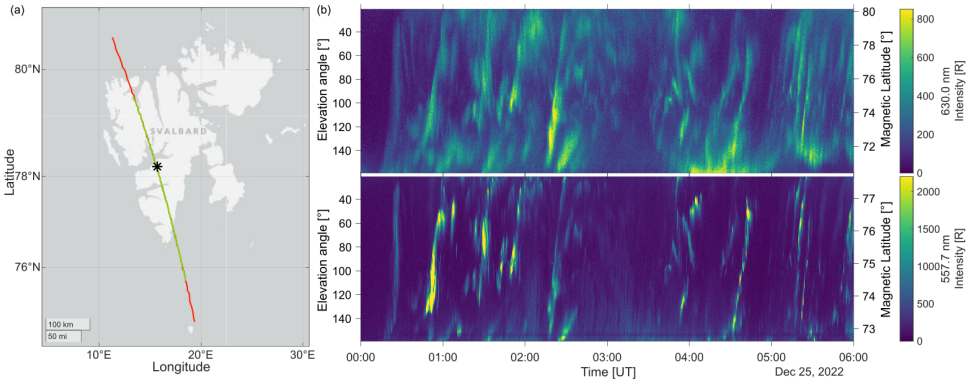

Figure 3.5: Panel (a) shows the FOV of the MSP for the 557.7 nm (green line) and 630.0 nm (red line) channels. KHO is located at the black star. Panel (b) gives example keograms for both channels. The left y-axis gives the elevation angle and the right y-axis gives the magnetic latitude. The intensity is given in Rayleigh. This image is based on Figure 1 of *van Hazendonk et al.* (2025).

3.2.1 Limitations

The MSP needs clear skies and sufficient darkness (a solar angle of $< 10°$ below the horizon) in order to image auroral features. Changes in the weather can affect the center wavelength of the filter passband. If the tilt angle calibration is slightly off, the measured brightness will be lower than the actual brightness. In extreme cases, the recorded brightness can become negative in case the background light intensity exceeds the auroral emission intensity. The recorded brightness is thus always a minimum value. A quality check is performed on the data to ensure positive values.

In order to convert the recorded elevation angles into magnetic latitudes, we need to assume the peak occurrence altitude of the auroral features. Depending on the time of day and auroral conditions, these altitudes can vary, resulting in incorrect magnetic latitudes. We use 250 km (120 km) altitude for 630.0 nm (557.7 nm) emissions (*Partamies et al.*, 2022).

3.3 Magnetometers

Magnetometers measure temporal variations in the Earth's magnetic field, $\Delta B(t)$, either from ground (ground-based magnetometers) or from spacecraft. These variations are assumed to be associated with electric currents in the ionosphere and they are expressed in local magnetic coordinates. The most common coordinate system is the $H-D-Z$ (or $X-Y-Z$) system, where H (X) corresponds to the horizontal northward component, D (Y) to the eastward component, and Z points vertically downward.

The signature of large-scale, toroidally polarized, low-m ULF waves, such as FLRs, in ground-based magnetometers is predominantly visible in the horizontal (north-south) component of the magnetic field perturbations. This is linked to changes in the Hall current (*Menk and Waters*, 2013). The characteristic FLR signature in ground-based magnetometers consists of a power peak localized in latitude combined with a 180° phase shift in latitude (e.g *Samson et al.*, 1992; *Menk and Waters*, 2013). Small-scale, high-m, waves, on the other hand, are usually not visible in ground-based magnetometers due to ionospheric screening. When the Pedersen and Hall conductance and the azimuthal wavelength are shorter than or comparable to the ionospheric height, the waves are attenuated, thus making it hard to observe small-scale waves on the ground (*Takahashi et al.*, 2013; *Hughes and Southwood*, 1976).

This thesis mostly uses the ground-based magnetometers from the International Mon-

itor for Auroral Geomagnetic Effects (IMAGE) network, which are located in Scandinavia. For world-wide coverage the SuperMAG (`http://supermag.jhuapl.edu`; *Gjerloev*, 2012) collaboration is used which contains the data of more than 300 ground-based magnetometers. The standard time resolution of these magnetometers is 10 s. In addition to ground-based magnetometers, the Lompe method, which is used in Paper III and addressed further in Subsection 3.6.1, uses magnetic field data from the Iridium and Swarm spacecraft.

3.3.1 Limitations

Each ground-based magnetometer measures the cumulative magnetic effect of all overhead currents within a footprint of several hundred kilometers. This spatial integration makes magnetometers highly effective for monitoring mesoscale and global current systems, but limits their ability to isolate small features. In coastal areas, such as around Svalbard, interpretation is further complicated by induction effects for the surrounding ocean. Conductive seawater supports electric currents that generate secondary magnetic fields (*Tyler et al.*, 2003; *Juusola et al.*, 2020). In these cases, the assumption that all current contributions are from the ionosphere is no longer valid.

3.4 Auroral Imaging

Periodic occurrences of auroral arcs associated with ULF waves can be observed using both ground-based and space-based optical instruments. Local arcs are typically captured with all-sky cameras or imagers, while global imagers provide broader context, such as identifying the location of the auroral oval. In Papers I and III, data from all-sky cameras and the Defense Meteorological Satellite Program (DMSP) were used for these purposes. The following sections describe the optical instruments relevant to this thesis in more detail.

3.4.1 All-Sky Cameras and Imagers

All-sky imagers or all-sky cameras use fish eye lenses to capture 180° images. In some cases, these images are taken in RGB format. This is the case for the Sony a7s All-Sky Camera located at KHO. This camera uses an exposure time of 4 s, and has a spatial resolution of 12 megapixels. The full sky image is often used to put MSP data in perspective, as the MSP only records along the geomagnetic meridian. Despite having

been used to put the MSP data in perspective, this data has not been shown in the papers itself. Other instruments are using filters to record specific wavelengths. An example of this at KHO is the all-sky imager (ASI) from the University in Oslo used in Paper I. This ASI uses a filterwheel with two filters (557.7 nm and 630.0 nm). The images are captured with a high-sensitivity Keo Sentry 4ix Monochromatic Imager from Keo Scientific using a 2048x2048 pixel CCD sensor which is downsampled to 512x512 pixels. The temporal resolution is 15 s for 557.7 nm and 30 s for 630.0 nm.

Limitations

Limitations of all-sky cameras and imagers are similar to those of the MSP. Again, a clear sky and darkness are needed to record auroral features. If we want to map the auroral feature to a geographical grid, we need to assume a peak emission height. However, in reality, emission occurs along a height profile rather than at one height (*Whiter et al.*, 2013). The exact peak emission altitude is dependent on ionospheric conditions, which can introduce additional uncertainties. These uncertainties are amplified near the edge of the FOV. As an example, a 10 km height offset in the 630.0 nm emission at 30° elevation corresponds to a $\sim$ 17 km horizontal offset.

3.4.2 Special Sensor Ultraviolet Spectrographic Imager

The DMSP mission provides in-situ measurements of the polar ionosphere using spacecraft in near-polar, Sun-synchronous orbits. The spacecraft are located around 840 km altitude and a full orbit lasts approximately 101 minutes. Since 2003, DMSP spacecraft carry the Special Sensor Ultraviolet Spectrographic Imager (SSUSI). The SSUSI instrument consists of two main components: a Scanning Imaging Spectrograph (SIS) and a Nadir Photometer System (NPS) (*Paxton et al.*, 1992, 2002).

In this thesis, the SIS instrument is used, which consists of a spectrograph which scans cross-track using a rotating mirror and a diffraction grating. The schematics of the scan and the different resolutions are shown in Figure 3.6. Each scan takes around 15 seconds and approximately 20 minutes are required to record an overview image of the auroral region. It records five different wavelength bands in the far ultra-violet range produced by Hydrogen, Oxygen, and Nitrogen: (1) H Lyman α (121.6 nm), (2 & 3) OI (130.4 nm and 135.6 nm), (4) N_2 Lyman-Birge-Hopfield (LBH) Short (LBHS) (140–160 nm), and (5) N_2 LBH Long (LBHL) (160–180 nm). The OI lines arise from the radiative recombination of O^+ ions with electrons. These different wavelengths are then used to calculate electron mean energies and energy fluxes, among others, which are used in this

thesis.

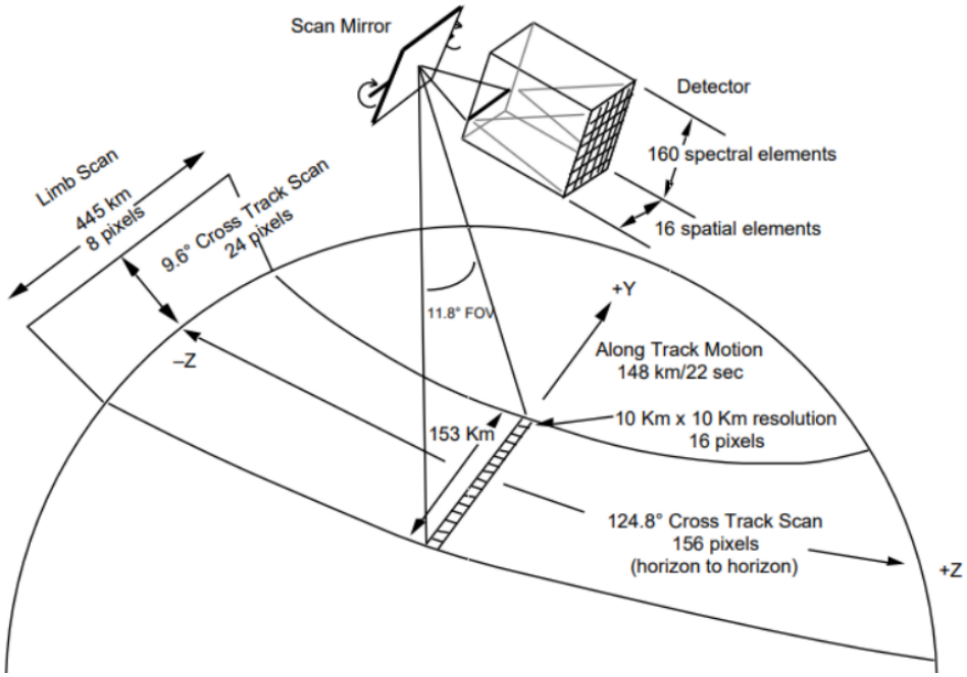

Figure 3.6: Schematic working principle of the SSUSI SIS instrument. Figure from *Paxton et al.* (1992).

Limitations

The orbit of the DMSP spacecraft is limited in time and space. One full orbit takes 101 min, thus limiting the number of available overpasses in the region of interest. Moreover, a single overpass of the northern auroral region takes approximately 20 min, thus combining several time stamps into one overview plot.

3.5 Other Spacecraft Observations

In addition to the magnetometers onboard the Iridium and Swarm spacecraft as well as the SSUSI instrument onboard DMSP satellites, other space-based instrumentation is used in this thesis.

3.5.1 DMSP – other instrumentation

In conjunction with the SSUSI data, other payloads onboard the DMSP spacecraft are used in Paper III to study ion up- and outflow. The Sensor for Ion and Electron Scintillation (SSIES) measures plasma properties, while the Special Sensor J (SSJ) particle detector provides data on the precipitating electron and ion fluxes (*Redmon et al.*, 2017). The SSJ/5 instrument measures both electron and ion fluxes across 19 logarithmically spaced energy channels from 30 eV to 30 keV. The SSIES instrument is used to obtain the vertical ion drift velocities and the plasma density to calculate ion upflow.

3.5.2 Solar Wind Data

At the first Lagrangian point (L1) the solar wind parameters, including the IMF components, solar wind velocity, and solar wind density are measured by a variety of spacecraft. For this thesis, the used data was collected by different spacecraft, namely ACE (*Smith et al.*, 1998), WIND (*Ogilvie and Desch*, 1997), and DSCOVR (*NOAA Space Weather Prediction Center*, 2016). This data, shifted to the bowshock nose with a 1 min resolution, is available through the Operating Missions as Nodes on the Internet (OMNI) project at NASA's Goddard Space flight Center (GSFC).

3.6 Models

In Paper III, two inversion models are used to determine FACs, total energy flux, and Joule heating, among others.

3.6.1 Lompe

The Local Mapping of Polar Electrodynamics (Lompe) model is a data assimilation framework developed to derive 2-dimensional (2D) maps of ionospheric electrodynamics. It provides a way to combine heterogeneous datasets, such as ground magnetometers, low-Earth orbit satellite measurements, and coherent scatter radars, into a physically constrained estimate of the high-latitude ionospheric state (*Laundal et al.*, 2022; *Hovland et al.*, 2022).

The Lompe technique is based on spherical elementary current system analysis, and finite difference analysis on a cubed-sphere projection. The model uses a thin-sheet

ionosphere approximation, modeling the height-integrated current, and representing it as a 2D surface current at a fixed altitude, typically at around 110 km. Relevant output parameters of the Lompe method for this thesis include FACs, convection velocities, and Joule heating rates. Compared to the localized EISCAT data, the Lompe model provides a larger-scale perspective on the magnetosphere-ionosphere coupling.

A major advantage of Lompe method is its flexible inversion framework. The grid location, spatial and temporal resolution, and size are adaptable and the method can assimilate different datasets based on availability and aim. In Paper III, DMSP SSUSI data in combination with solar EUV and a constant background conductance are used to obtain the Pedersen and Hall conductances. Other Lompe inputs are dominated by magnetic field measurements via ground-based magnetometers and Iridium. Swarm (magnetic field) and SuperDARN (ion velocities) provide a few data points near the edges of the grids.

Limitations

The Lompe model can only explain the measured (magnetic) variations within the used grid, while some perturbations could be caused by currents flowing outside of the grid. This is an important boundary conditions to be taken into account. In addition, the inversion relies on correct input data, which is not always available. For example, the background conductance is not commonly studied and the values are often estimates (*Robinson et al.*, 2021; *Laundal et al.*, 2025). Small changes in the background conductance can, however, correspond to large variations in the Joule heating rate for example as shown in Paper III.

3.6.2 ELSPEC

The ELectron Spectrum (ELSPEC) method (*Virtanen et al.*, 2018) is based on inversion to estimate the differential fluxes of precipitating electrons within the 1–100 keV energy range using field-aligned ISR data, in this case from the EISCAT Svalbard radar, in the altitude region 80–150 km. The output parameters from ELSPEC include the differential number flux, differential energy flux, upward FAC magnitude, and the total energy flux with their statistical errors. All these outputs correspond to localized features in the ionosphere, since the EISCAT measurements are concentrated within the narrow radar beam. More information on the method is available in *Virtanen et al.* (2018).

Limitations

Due to the lower energy limit of 1 keV, ELSPEC cannot detect low-energy electrons (< 1 keV), resulting in a potential underestimation of the FACs. Furthermore, a polynomial model is used to approximate the differential number flux [m^{-2} s^{-1} eV^{-1}]. The error estimates are underestimated because of the assumption that the selected spectrum model perfectly reproduces the true spectrum. Other assumptions in ELSPEC include: (1) that the spectrum does not change within 5 s time steps, (2) that NO^+ and $O_2{}^+$ are the main ion species between 80–150 km altitude, and (3) that vibrationally excited states are ignored, among others (*Virtanen et al.*, 2018).

Chapter 4

Summary of Results

This thesis studies the role of ULF waves in the magnetosphere–ionosphere coupling in the polar ionosphere, as specified further in Objectives 1 and 3, as well as their occurrence characteristics (Objective 2). To facilitate the study of ULF wave characteristics, we first developed a detection method to quantitatively detect, and subsequently reconstruct, ULF waves. The core of this research is presented in three scientific papers, Papers I—III, which can be found at the end of this thesis. In this chapter, first the automatic detection method as described in Paper I and re-applied in Paper II, is introduced. Subsequently, summaries of Papers I, II, and III are provided.

4.1 ULF Wave Detection Method

Paper I describes a new detection method developed to recognize ULF wave fronts in EISCAT data. Paper II then adapted the method to be applied to keograms of the MSP. This detection method aims to minimize the subjective bias in the detection of ULF waves. In addition, it allows for large-scale systematic processing of data.

4.1.1 Detection Method on EISCAT Data

The detection algorithm as originally described in Paper I was developed to detect ULF wave activity in low-elevation EISCAT data. When the VHF radar is pointing northward at low elevation, a location further away from the radar corresponds to an increasing altitude and latitude. In case of a poleward propagating wave, the 2D structure of the wave field corresponds to multiple slanted wavefronts moving toward higher latitudes

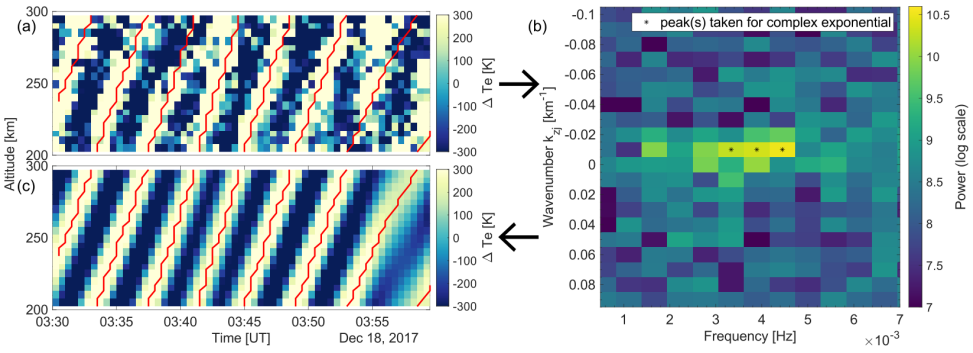

Figure 4.1: An example window for the reconstruction of a ULF wave. Panel (a) shows the high-pass filtered EISCAT VHF signal. Panel (b) shows the power spectrum from the 2D FFT in which the peaks used for reconstruction are highlighted with asterisks. Panel (c) shows the real part of the reconstructed complex wave. Reconstructed wavefronts are overlaid in red in panels (a) and (c). After Figure 3 from *van Hazendonk et al.* (2024).

and altitudes.

For the detection method, the EISCAT data are analyzed with an integration time of 30 s, and an altitude integration of 5 km. To isolate the ULF wave signature, a high-pass filter was applied by subtracting a median background computed over a 15 min by 30 km window. This filter corresponds to a frequency cutoff of 0.49 mHz. Missing data segments shorter than 10 min were interpolated linearly, while longer data gaps were treated as independent intervals.

To extract the frequency and spatial characteristics of the ULF wave event, a 2D fast-Fourier transform (FFT) was applied to the filtered data. An example of such a 2D FFT is shown in Figure 4.1b. Each FFT was taken over a 30 min by 100 km window, with 15 min overlap between successive windows. An example of such a window is shown in Figure 4.1a. The 30 min window length results in a frequency resolution of $\Delta f = 0.56$ mHz.

To enhance spectral robustness, seven consecutive 30 min windows (covering 2 hours) were stacked to generated averaged power spectra. Up to four spectral peaks exceeding a certain threshold were selected. In our case, this threshold was equal to 85% of the maximum power peak for detection in our main parameter, the electron density, while it was being relaxed to 65% for detection in the other parameters. Only peaks detected in both the individual power spectra as well as the averaged power spectra are used. Each identified peak j, characterized by its amplitude A_j, frequency ω_j, phase ϕ_j, and vertical

wavenumber k_{zj}, was used to reconstruct the complex wave field using

$$\sum A_j \exp i\phi_j \exp\left(i(\omega_j t - k_{zj} z)\right), \tag{4.1}$$

where t is the reconstruction time in seconds and z the altitude in km at which the reconstruction takes place. The real part of the reconstructed complex wave is shown in Figure 4.1c. The wavefronts in the reconstructed spectrum are defined as the location where a phase shift occurs and are overlaid in red in Figure 4.1 panels a and c.

4.1.2 Detection Method on MSP Data

For Paper II, we tailored the detection method to MSP data. Since the MSP scans along the geomagnetic meridian, each wavelength channel shows how auroral features of that wavelength move between geomagnetic north and south. Auroral arcs, the optical signature of ULF waves, will occur as slanted wavefronts similarly to their appearance in low-elevation EISCAT radars. Applying the algorithm to the MSP database thus gives us only propagation information in the north–south direction and not in the east–west direction, making it impossible to derive sunward or anti-sunward propagation direction of the ULF waves.

To make the MSP data suitable for the detection method, the elevation angle of the MSP is converted into magnetic latitude (mlat). For this, a fixed emission height is assumed at 250 km (120 km) altitude for the 630.0 nm (557.7 nm) wavelength, resulting in a FOV of 72°–78° (73°–77°) mlat. Linear interpolation ensures a fixed mlat spacing of 0.05°. Similar to the original detection method, noise is reduced by applying a high-pass filter, which consists of moving median window with a window size of 20 min by 20 km. The time length is slightly increased compared to the original detection algorithm to reduce the frequency cutoff to 0.37 mHz.

To avoid false positives, the analysis is run with four different window sizes for the 2D FFT. The window lengths in the time domain are 30 min and 60 min, combined with window lengths of 2° and 3° mlat in the latitudinal direction. Detection in the 630.0 nm channel is only registered when it occurs in at least three out of four window sizes. The results of the 60 min by 3° mlat window, which gives a frequency resolution of 0.28 mHz, are then used to analyze the ULF wave characteristics.

4.2 Paper I: Detection and Energy Dissipation of ULF Waves in the Polar Ionosphere: A Case Study Using the EISCAT Radar

In Paper I, we describe a novel algorithm, described in Section 4.1, that enables the detection of ULF waves in EISCAT data. We then show the effectiveness of this method with a case study. The other objective of this case study is to quantify the energy dissipation–both electromagnetic and kinetic–of a ULF wave event. The case study took place on 18 December 2017 between Svalbard and mainland Norway and is visible in data from the EISCAT VHF radar that points northward at low elevation. The event is most pronounced in the electron density parameters, which is thus used for detection of the wave. The ULF wave event was found to last for 2 hr and 15 min. Using ground-based magnetometers and the SSUSI instrument on board the DMSP spacecraft, the minimum area of the ULF wave event was estimated to 4° mlat by 74° magnetic longitude, which was then used to extrapolate the energy dissipation calculated within the EISCAT radar beam.

The energy dissipation rates are divided into an EM rate, which comes from the Poynting flux and a kinetic flux. The EM flux is calculated for Joule and frictional heating, while the kinetic flux can be divided into two different sources: low energy ($\leq$ 100 eV) and a high energy ($>$ 100 eV) electrons, where the latter represents ionization. The heating rates were then determined for the entire ULF wave event and extrapolated over the entire ULF wave area. The Joule and frictional heating rates show the same order of magnitude (1.24×10^{13} J and 7.3×10^{12} J, respectively). In addition, we found the kinetic flux, for which the ionization part is dominant, to be of almost equal magnitude (8.7×10^{12} J) as the EM fluxes. The significant kinetic flux shows that, contrary to the previous assumption that the EM flux is dominant, the kinetic flux can be almost as large as the EM flux. The kinetic flux should thus be taken into account into future ULF wave energy dissipation estimations.

4.3 Paper II: A Statistical Study of Optical Signatures of High-Latitude Pc5 Waves

In Paper II, the method from Paper I is adjusted to fit to data from the MSP located at KHO in Longyearbyen, Svalbard. This allows us to detect ULF wave-driven auroral arcs (UAAs) in the MSP data. To enable the statistical study of these UAA characteristics,

as aimed for by Objective 2 in this thesis, the method is applied to the dawn and dusk sectors of the full MSP dataset from 2007 onward, corresponding to 17 seasons of data. In total, we found 198 UAAs in the 630.0 nm channel of the MSP, of which a small part also shows detection in the 557.7 nm channel. These 198 UAAs can be categorized into distinct groups according to magnetic local time, with 129 occurrences at dawn and 69 at dusk, or based on their propagation direction, with 126 events with poleward propagation and 72 with equatorward propagation.

Previous literature on optical signatures of ULF waves mostly focus on FLR signatures and almost exclusively report these FLRs to move poleward. This suggests that the equatorward-propagating population might be a different class of ULF waves. Therefore, we looked at driving mechanisms for the different ULF wave populations. The poleward-propagating population partly consists of FLR driven auroral arcs, exhibiting a previously reported dawn–dusk asymmetry. Solar wind data suggested an external generation mechanism on the flanks of the magnetopause through the Kelvin-Helmholtz instability. Another part of the poleward-propagating population is most likely made up of small-scale internally generated waves. The equatorward-propagating population, on the other hand, also seems to consists of these small-scale internally generated waves. Possibly, the energy source exciting those waves is formed by substorm-injected energetic particles.

4.4 Paper III: High-Latitude Observations of ULF Wave Driven Ion Upflow

In Paper III, we present a case study of the first direct observations of ionospheric ion upflow driven by UAAs at high-latitude. The event occurred above Svalbard on 16 November 2021 under quiet geomagnetic conditions (Kp = 2) and was investigated using a comprehensive multi-instrument approach that included the ESR, the MSP at KHO, ground-based magnetometers, and satellite observations from DMSP, Iridium, and Swarm, combined with inversion models (ELSPEC and Lompe) to quantify energy dissipation, FACs, and ion upflow, addressing Objectives 1 and 3 in this thesis.

The UAA event, originally detected as part of the statistical study in Paper II, manifested optically as a series of six poleward moving auroral arcs, primarily observed in the 630.0 nm emission line. These arcs had a frequency of 1.1 mHz and propagated poleward at 740 m s^{-1} between 72°–75° mlat. ESR measurements revealed periodic electron density and temperature enhancements consistent with auroral precipitation, accompanied by energetic ion upflow. The ion upflow fluxes were in the low to medium range (median

of 3.3×10^{13} particles m^{-2} s^{-1}) and corresponded to type 2 upflow, driven by enhanced electron temperatures rather than ion heating. No concurrent outflow signatures were detected by the DMSP spacecraft.

Ground-based magnetometer data revealed power enhancements near 1.1 mHz, but lacked the 180° phase shift that is characteristic for FLRs. This indicated that the event was driven by small-scale, non-FLR ULF waves. Nevertheless, inversion models showed FAC magnitudes up to 6 µA m^{-2} locally and 3 µA m^{-2} regionally, which are comparable to those reported for large-scale FLRs. Similarly, energy fluxes up to 12 mW m^{-2} and Joule heating rates of 8 – 11 mW m^{-2} were found, placing the energy dissipation of this event within the range typically associated with larger-scale ULF wave activity. The study thus highlights the complex nature of UAAs and their role in the magnetosphere-ionosphere coupling. Despite the non-FLR nature, the UAA event generated significant FACs, energy dissipation, and ion upflow, indicating that even small-scale ULF waves can drive ion upflow in the ionosphere.

Chapter 5

Conclusion and Future Work

The motivation for the research in this thesis was to deepen our understanding of the role ULF waves play in the magnetosphere–ionosphere coupling and energy exchange at high-latitude. The magnetosphere–ionosphere coupling is investigated through quantifying energy dissipation–both EM and kinetic–, ion upflow, and FAC magnitudes. In addition, the optical signature of ULF waves, which is a sign of energy dissipation, is used to study occurrence statistics, propagation direction, and characteristics of ULF wave driven auroral arcs. Specifically, three studies were carried out to address the main objectives of this thesis as introduced in the Chapter 1:

1. In Paper I the objective about energy dissipation in the ionosphere is addressed by quantifying the electromagnetic and kinetic energy fluxes of a ULF wave event using EISCAT radar data. In addition, Paper I introduced a ULF wave detection algorithm developed to enable quantitative ULF wave detection in EISCAT data.
2. In Paper II, the objective addressing the ULF wave characteristics is investigated by examining the occurrence characteristics of ULF wave-driven auroral arcs using an adapted version of the detection algorithm described in Paper I applied to MSP data.
3. In Paper III both the objectives on energy dissipation and the role of ULF waves in magnetosphere–ionosphere coupling are studied. The paper investigated how ULF waves influence ion upflow, FAC magnitudes, and energy dissipation using EISCAT data, inversion models, and spacecraft data, among others.

5.1 Main Findings

The key findings of this thesis, which are discussed in more detail in Chapter 4, are the following:

- The kinetic energy flux associated with a ULF wave event can be of almost equal magnitude as the EM flux. Studies focusing solely on the EM flux are thus prone to underestimating the total energy budget of ULF wave events.
- The energy budget of a ULF wave event can amount to around 10% of the substorm budget.
- As a result of the algorithm, a new statistically significant population of equatorward propagating UAAs was discovered (36%, 72 events). Before this work, only three case studies existed.
- Part of the UAA events, both equatorward and poleward propagating, consist of small-scale, internally generated, ULF waves, showing that small-scale waves can be associated with auroral emissions.
- The first link between ionospheric ion upflow and the presence of UAAs at high latitude has been found. This indicates that ULF waves result in not only energy dissipation into the ionosphere, but also energy extraction toward the magnetosphere by driving ion upflow.

In summary, we have developed a detection method to detect ULF waves in ISR data and optical keograms. This detection method has then been used to study energy exchange driven by ULF waves via case studies, showing strong magnetosphere–ionosphere coupling through EM and kinetic energy dissipation, FACs, and ion upflow. In addition, the detection method allowed for a statistical study into the characteristics of UAAs.

5.2 Future Work

The results in this thesis have shown that existent frameworks and data cannot always capture the complicated dynamics of ULF waves and their energy exchange. Events can show behavior corresponding to small-scale ULF waves (e.g. limited signature in ground-based magnetometers), while energy fluxes and FAC magnitudes are in range with those of large-scale ULF wave events. One of the most important parameters when quantifying energy exchange rates is the conductivity. Direct measurements of the conductivity are rare. In this thesis, a combination of local measurements, provided by EISCAT radars, and global measurements, provided by DMSP spacecraft, have been

used. However, both measurements are limited in time and space and rely on assumptions to derive conductivities. Auroral imaging from space, such as previously provided by the Imager for Magnetopause-to-Aurora Global Exploration (IMAGE) satellite, would provide conductance estimations with higher time and spatial resolution thanks to its elliptical orbit compared to the current conductance estimates from DMSP. In addition, modern ISRs, such as EISCAT 3D, could improve the spatial coverage and temporal resolution of conductivity estimates.

Furthermore, the automatic detection method, both in ISR data and optical keograms, could help with expanding the ULF wave event list from Paper II. Ultimately, this could allow for statistical studies into energy dissipation rates, FAC magnitudes, and ion upflow related to ULF waves.

Bibliography

Alfvén, H. (1942), Existence of Electromagnetic-Hydrodynamic Waves, *Nature*, *150*(3805), 405–406, doi:10.1038/150405d0.

Baddeley, L. J., D. A. Lorentzen, N. Partamies, M. Denig, V. A. Pilipenko, K. Oksavik, X. Chen, and Y. Zhang (2017), Equatorward propagating auroral arcs driven by ULF wave activity: Multipoint ground- and space-based observations in the dusk sector auroral oval: ULF wave-driven auroral arcs, *Journal of Geophysical Research: Space Physics*, *122*(5), 5591–5605, doi:10.1002/2016JA023427.

Baumjohann, W., and R. A. Treumann (1996), *Basic Space Plasma Physics*, Published by Imperial College Press and distributed by World Scientific Publishing CO., doi:10.1142/p015.

Bittencourt, J. A. (2004), *Fundamentals of Plasma Physics*, Springer New York, New York, NY, doi:10.1007/978-1-4757-4030-1.

Bjoland, L. M., Y. Ogawa, and S. Haaland (2025), Characteristics of the ambipolar electric field during ion upflow events, *Earth, Planets and Space*, *77*(1), 78, doi:10.1186/s40623-025-02217-6.

Brekke, A. (2013), *Physics of the Upper Polar Atmosphere*, Springer Atmospheric Sciences, Springer Berlin Heidelberg, Berlin, Heidelberg, doi:10.1007/978-3-642-27401-5.

Dougherty, J., and D. Farley (1960), A theory of incoherent scattering of radio waves by a plasma, *Proceedings of the Royal Society of London. Series A. Mathematical and Physical Sciences*, *259*(1296), 79–99, doi:10.1098/rspa.1960.0212.

Dungey, J. W. (1961), Interplanetary Magnetic Field and the Auroral Zones, *Physical Review Letters*, *6*(2), 47–48, doi:10.1103/PhysRevLett.6.47.

Evans, J. (1969), Theory and practice of ionosphere study by Thomson scatter radar, *Proceedings of the IEEE*, *57*(4), 496–530, doi:10.1109/PROC.1969.7005.

Farley, D. T. (1969), Incoherent Scatter Correlation Function Measurements, *Radio Science*, *4*(10), 935–953, doi:10.1029/RS004i010p00935.

Fenrich, F. R., D. M. Gillies, E. Donovan, and D. Knudsen (2019), Flow Velocity and Field-Aligned Current Associated With Field Line Resonance: SuperDARN Measurements, *Journal of Geophysical Research: Space Physics*, *124*(6), 4889–4904, doi:10.1029/2019JA026529.

Frey, H. U. (2007), Localized aurora beyond the auroral oval, *Reviews of Geophysics*, *45*(1), 2005RG000,174, doi:10.1029/2005RG000174.

Gillies, D. M., D. Knudsen, R. Rankin, S. Milan, and E. Donovan (2018), A Statistical Survey of the 630.0-nm Optical Signature of Periodic Auroral Arcs Resulting From Magnetospheric Field Line Resonances, *Geophysical Research Letters*, *45*(10), 4648–4655, doi:10.1029/2018GL077491.

Gjerloev, J. W. (2012), The SuperMAG data processing technique, *Journal of Geophysical Research: Space Physics*, *117*(A9), 2012JA017,683, doi:10.1029/2012JA017683.

Grydeland, T., A. Strømme, T. van Eyken, and C. La Hoz (2004), The Capabilities of the EISCAT Svalbard Radar for Inter-hemispheric Coordinated Studies, doi:10.48550/arxiv.physics/0404098, publisher: arXiv Version Number: 1.

Hartinger, M. D., M. B. Moldwin, S. Zou, J. W. Bonnell, and V. Angelopoulos (2015), ULF wave electromagnetic energy flux into the ionosphere: Joule heating implications, *Journal of Geophysical Research: Space Physics*, *120*(1), 494–510, doi:10.1002/2014JA020129.

Hasegawa, H., M. Fujimoto, T.-D. Phan, H. Rème, A. Balogh, M. W. Dunlop, C. Hashimoto, and R. TanDokoro (2004), Transport of solar wind into Earth's magnetosphere through rolled-up Kelvin–Helmholtz vortices, *Nature*, *430*(7001), 755–758, doi:10.1038/nature02799.

Herlingshaw, K., N. Partamies, C. M. van Hazendonk, M. Syrjäsuo, L. J. Baddeley, M. G. Johnsen, N. K. Eriksen, I. McWhirter, A. Aruliah, M. J. Engebretson, K. Oksavik, F. Sigernes, D. A. Lorentzen, T. Nishiyama, M. B. Cooper, J. Meriwether, S. Haaland, and D. Whiter (2025), Science highlights from the Kjell Henriksen Observatory on Svalbard, *Arctic Science*, *11*, 1–25, doi:10.1139/as-2024-0009.

Hovland, A. Ø., K. M. Laundal, J. P. Reistad, S. M. Hatch, S. J. Walker, M. Madelaire, and A. Ohma (2022), The Lompe code: A Python toolbox for ionospheric data analysis, *Frontiers in Astronomy and Space Sciences*, *9*, 1025,823, doi:10.3389/fspas.2022.1025823.

Huang, C. (2021), Magnetospheric Energy Input to the Ionosphere, in *Geophysical Monograph Series*, edited by C. Huang, G. Lu, Y. Zhang, and L. J. Paxton, 1 ed., pp. 1–20, Wiley, doi:10.1002/9781119815617.ch1.

Hughes, W. J., and D. J. Southwood (1976), The screening of micropulsation signals by the atmosphere and ionosphere, *Journal of Geophysical Research*, *81*(19), 3234–3240, doi:10.1029/JA081i019p03234.

Hunten, D. M., and M. B. McElroy (1966), Quenching of metastable states of atomic and molecular oxygen and nitrogen, *Reviews of Geophysics*, *4*(3), 303–328, doi:10.1029/RG004i003p00303.

Jacobs, J. A., Y. Kato, S. Matsushita, and V. A. Troitskaya (1964), Classification of geomagnetic micropulsations, *Journal of Geophysical Research*, *69*(1), 180–181, doi:10.1029/jz069i001p00180.

James, M. K., T. K. Yeoman, P. N. Mager, and D. Y. Klimushkin (2013), The spatio-temporal characteristics of ULF waves driven by substorm injected particles, *Journal of Geophysical Research: Space Physics*, *118*(4), 1737–1749, doi:10.1002/jgra.50131.

Johnson, C. Y. (1969), Ion and neutral composition of the ionosphere., *Annals of the IQSY*, *5*, 197–213, tex.adsnote: Provided by the SAO/NASA Astrophysics Data System.

Juusola, L., H. Vanhamäki, A. Viljanen, and M. Smirnov (2020), Induced currents due to 3D ground conductivity play a major role in the interpretation of geomagnetic variations, *Annales Geophysicae*, *38*(5), 983–998, doi:10.5194/angeo-38-983-2020.

Kawamura, Y., K. Hosokawa, S. Nozawa, Y. Ogawa, T. Kawabata, S.-I. Oyama, Y. Miyoshi, S. Kurita, and R. Fujii (2020), Estimation of the emission altitude of pulsating aurora using the five-wavelength photometer, *Earth, Planets and Space*, *72*(1), 96, doi:10.1186/s40623-020-01229-8.

Kelley, M. C. (2009), *The Earth's Ionosphere: Plasma Physics and Electrodynamics*, no. v. 96 in International geophysics series, 2nd ed ed., Academic Press, Amsterdam Boston.

Kepko, L., H. E. Spence, and H. J. Singer (2002), ULF waves in the solar wind as direct drivers of magnetospheric pulsations, *Geophysical Research Letters*, *29*(8), doi:10.1029/2001GL014405.

Kivelson, M. G., and C. T. Russell (Eds.) (1995), *Introduction to Space Physics:*, 1 ed., Cambridge University Press, doi:10.1017/9781139878296.

Kivelson, M. G., and D. J. Southwood (1985), Resonant ULF waves: A new interpretation, *Geophysical Research Letters*, *12*(1), 49–52, doi:10.1029/GL012i001p00049.

Kivelson, M. G., and D. J. Southwood (1986), Coupling of global magnetospheric MHD eigenmodes to field line resonances, *Journal of Geophysical Research: Space Physics*, *91*(A4), 4345–4351, doi:10.1029/JA091iA04p04345.

Kozlovsky, A. E., H. Nilsson, and V. V. Safargaleev (2006), Complex study of the auroral arc dynamics and ionospheric plasma convection in prenoon hours, *Geomagnetism and Aeronomy*, *46*(4), 473–484, doi:10.1134/S0016793206040098.

Laundal, K. M., J. P. Reistad, S. M. Hatch, M. Madelaire, S. Walker, A. Ø. Hovland, A. Ohma, V. G. Merkin, and K. A. Sorathia (2022), Local Mapping of Polar Ionospheric Electrodynamics, *Journal of Geophysical Research: Space Physics*, *127*(5), e2022JA030,356, doi:10.1029/2022JA030356.

Laundal, K. M., A. S. Skeidsvoll, B. Popescu Braileanu, S. M. Hatch, N. Olsen, and H. Vanhamäki (2025), Global Inductive Magnetosphere-Ionosphere-Thermosphere Coupling, doi:10.5194/egusphere-2025-2051.

Le, G., J. A. Slavin, and R. J. Strangeway (2010), Space Technology 5 observations of the imbalance of regions 1 and 2 field-aligned currents and its implication to the cross-polar cap Pedersen currents, *Journal of Geophysical Research: Space Physics*, *115*(A7), doi:10.1029/2009ja014979.

Lehtinen, M. S., and A. Huuskonen (1996), General incoherent scatter analysis and GUISDAP, *Journal of Atmospheric and Terrestrial Physics*, *58*(1-4), 435–452, doi:10.1016/0021-9169(95)00047-X.

Lynch, K. A., J. L. Semeter, M. Zettergren, P. Kintner, R. Arnoldy, E. Klatt, J. LaBelle, R. G. Michell, E. A. MacDonald, and M. Samara (2007), Auroral ion outflow: low altitude energization, *Annales Geophysicae*, *25*(9), 1967–1977, doi:10.5194/angeo-25-1967-2007.

Mager, O. V., M. A. Chelpanov, P. N. Mager, D. Y. Klimushkin, and O. I. Berngardt (2019), Conjugate Ionosphere-Magnetosphere Observations of a Sub-Alfvénic Compressional Intermediate-m Wave: A Case Study Using EKB Radar and Van Allen Probes, *Journal of Geophysical Research: Space Physics*, *124*(5), 3276–3290, doi:10.1029/2019JA026541.

Mager, P. N., D. Y. Klimushkin, and N. Ivchenko (2009), On the equatorward phase propagation of high-m ULF pulsations observed by radars, *Journal of Atmospheric and Solar-Terrestrial Physics*, *71*(16), 1677–1680, doi:10.1016/j.jastp.2008.09.001.

Mager, P. N., O. I. Berngardt, D. Y. Klimushkin, N. A. Zolotukhina, and O. V. Mager (2015), First results of the high-resolution multibeam ULF wave experiment at the

Ekaterinburg SuperDARN radar: Ionospheric signatures of coupled poloidal Alfvén and drift-compressional modes, *Journal of Atmospheric and Solar-Terrestrial Physics*, *130-131*, 112–126, doi:10.1016/j.jastp.2015.05.017.

Mathews, J. T., I. R. Mann, I. J. Rae, and J. Moen (2004), Multi-instrument observations of ULF wave-driven discrete auroral arcs propagating sunward and equatorward from the poleward boundary of the duskside auroral oval, *Physics of Plasmas*, *11*(4), 1250–1259, doi:10.1063/1.1647137.

Menk, F. W., and C. L. Waters (2013), *Magnetoseismology: Ground-Based Remote Sensing of Earth's Magnetosphere*, 1 ed., Wiley, doi:10.1002/9783527652051.

Michael, C. M., T. K. Yeoman, D. M. Wright, M. A. Chelpanov, and P. N. Mager (2024), Evolving Phase Propagation in an Intermediate-m ULF Wave Driven by Substorm-Injected Particles, *Journal of Geophysical Research: Space Physics*, *129*(3), e2023JA031,654, doi:10.1029/2023JA031654.

Motoba, T., Y. Ogawa, Y. Ebihara, A. Kadokura, A. J. Gerrard, and A. T. Weatherwax (2021), Daytime Pc5 Diffuse Auroral Pulsations and Their Association With Outer Magnetospheric ULF Waves, *Journal of Geophysical Research: Space Physics*, *126*(8), e2021JA029,218, doi:10.1029/2021JA029218.

NOAA Space Weather Prediction Center (2016), Deep space climate observatory (DSCOVR), doi:10.7289/V51Z42F7.

Ogilvie, K., and M. Desch (1997), The WIND spacecraft and its early scientific results, *Advances in Space Research*, *20*(4-5), 559–568, doi:10.1016/S0273-1177(97)00439-0.

Parker, E. N. (1963), *Interplanetary dynamical processes*, Wiley - Interscience Publishers, New York.

Partamies, N., D. Whiter, K. Kauristie, and S. Massetti (2022), Magnetic local time (mlt) dependence of auroral peak emission height and morphology, *Annales Geophysicae*, *40*(5), 605–618, doi:10.5194/angeo-40-605-2022.

Partamies, N., R. Dayton-Oxland, K. Herlingshaw, I. Virtanen, B. Gallardo-Lacourt, M. Syrjäsuo, F. Sigernes, T. Nishiyama, T. Nishimura, M. Barthelemy, A. Aruliah, D. Whiter, L. Mielke, M. Grandin, E. Karvinen, M. Spijkers, and V. E. Ledvina (2025), First observations of continuum emission in dayside aurora, *Annales Geophysicae*, *43*(2), 349–367, doi:10.5194/angeo-43-349-2025.

Paxton, L. J., C.-I. Meng, G. H. Fountain, B. S. Ogorzalek, E. H. Darlington, S. A. Gary, J. O. Goldsten, D. Y. Kusnierkiewicz, S. C. Lee, L. A. Linstrom, J. J. Maynard, K. Peacock, D. F. Persons, and B. E. Smith (1992), Special sensor ultraviolet

spectrographic imager: an instrument description, in *Instrumentation for planetary and terrestrial atmospheric remote sensing*, vol. 1745, edited by S. Chakrabarti and A. B. Christensen, pp. 2 – 15, SPIE / International Society for Optics and Photonics, doi:10.1117/12.60595.

Paxton, L. J., D. Morrison, Y. Zhang, H. Kil, B. Wolven, B. S. Ogorzalek, D. C. Humm, and C.-I. Meng (2002), Validation of remote sensing products produced by the special sensor ultraviolet scanning imager (SSUSI): a far UV-imaging spectrograph on DMSP F-16, in *Optical spectroscopic techniques, remote sensing, and instrumentation for atmospheric and space research IV*, vol. 4485, edited by A. M. Larar and M. G. Mlynczak, pp. 338 – 348, SPIE / International Society for Optics and Photonics, doi:10.1117/12.454268.

Rae, I. J., C. E. J. Watt, F. R. Fenrich, I. R. Mann, L. G. Ozeke, and A. Kale (2007), Energy deposition in the ionosphere through a global field line resonance, *Annales Geophysicae*, *25*(12), 2529–2539, doi:10.5194/angeo-25-2529-2007.

Rae, I. J., K. R. Murphy, C. E. J. Watt, G. Rostoker, R. Rankin, I. R. Mann, C. R. Hodgson, H. U. Frey, A. W. Degeling, and C. Forsyth (2014), Field line resonances as a trigger and a tracer for substorm onset, *Journal of Geophysical Research: Space Physics*, *119*(7), 5343–5363, doi:10.1002/2013JA018889.

Rankin, R., D. M. Gillies, and A. W. Degeling (2021), On the Relationship Between Shear Alfvén Waves, Auroral Electron Acceleration, and Field Line Resonances, *Space Science Reviews*, *217*(4), 60, doi:10.1007/s11214-021-00830-x.

Redmon, R. J., W. F. Denig, L. M. Kilcommons, and D. J. Knipp (2017), New DMSP database of precipitating auroral electrons and ions, *Journal of Geophysical Research: Space Physics*, *122*(8), 9056–9067, doi:10.1002/2016JA023339.

Richmond, A. D. (2007), Ionosphere, in *Encyclopedia of Geomagnetism and Paleomagnetism*, edited by D. Gubbins and E. Herrero-Bervera, pp. 452–454, Springer Netherlands, Dordrecht, doi:10.1007/978-1-4020-4423-6_159.

Robinson, R. M., L. Zanetti, B. Anderson, S. Vines, and J. Gjerloev (2021), Determination of Auroral Electrodynamic Parameters From AMPERE Field-Aligned Current Measurements, *Space Weather*, *19*(4), e2020SW002,677, doi:10.1029/2020SW002677.

Rubtsov, A. V., O. V. Agapitov, P. N. Mager, D. Y. Klimushkin, O. V. Mager, F. S. Mozer, and V. Angelopoulos (2018), Drift Resonance of Compressional ULF Waves and Substorm-Injected Protons From Multipoint THEMIS Measurements, *Journal of Geophysical Research: Space Physics*, *123*(11), 9406–9419, doi:10.1029/2018JA025985.

Saito, T. (1978), Long-period irregular magnetic pulsation, Pi3, *Space Science Reviews*, *21*(4), doi:10.1007/bf00173068.

Samson, J. C., B. G. Harrold, J. M. Ruohoniemi, R. A. Greenwald, and A. D. M. Walker (1992), Field line resonances associated with MHD waveguides in the magnetosphere, *Geophysical Research Letters*, *19*(5), 441–444, doi:10.1029/92GL00116.

Samson, J. C., R. Rankin, and V. T. Tikhonchuk (2003), Optical signatures of auroral arcs produced by field line resonances: comparison with satellite observations and modeling, *Annales Geophysicae*, *21*(4), 933–945, doi:10.5194/angeo-21-933-2003.

Schunk, R. (2000), Theoretical developments on the causes of ionospheric outflow, *Journal of Atmospheric and Solar-Terrestrial Physics*, *62*(6), 399–420, doi:10.1016/S1364-6826(00)00017-1.

Schunk, R. W., and A. F. Nagy (2009), *Ionospheres: Physics, Plasma Physics, and Chemistry, Second Edition*, Cambridge Atmospheric and Space Science Series, Cambridge University Press.

Smith, C. W., J. L'Heureux, N. F. Ness, M. H. Acuña, L. F. Burlaga, and J. Scheifele (1998), The Ace Magnetic Fields Experiment, in *The Advanced Composition Explorer Mission*, edited by C. T. Russell, R. A. Mewaldt, and T. T. Von Rosenvinge, pp. 613–632, Springer Netherlands, Dordrecht, doi:10.1007/978-94-011-4762-0_21.

Southwood, D., and W. Hughes (1983), Theory of hydromagnetic waves in the magnetosphere, *Space Science Reviews*, *35*(4), doi:10.1007/BF00169231.

Strangeway, R. J. (2012), The equivalence of Joule dissipation and frictional heating in the collisional ionosphere, *Journal of Geophysical Research: Space Physics*, *117*(A2), doi:10.1029/2011JA017302.

Takahashi, K., M. D. Hartinger, V. Angelopoulos, K. Glassmeier, and H. J. Singer (2013), Multispacecraft observations of fundamental poloidal waves without ground magnetic signatures, *Journal of Geophysical Research: Space Physics*, *118*(7), 4319–4334, doi:10.1002/jgra.50405.

Thayer, J. P., and J. Semeter (2004), The convergence of magnetospheric energy flux in the polar atmosphere, *Journal of Atmospheric and Solar-Terrestrial Physics*, *66*(10), 807–824, doi:10.1016/j.jastp.2004.01.035.

Tjulin, A., M. Miháliková, I. Häggström, and C.-F. Enell (2024), EISCAT User Manual, doi:https://eiscat.se/wp-content/uploads/2024/01/EISCAT_UM.pdf.

Tyler, R. H., S. Maus, and H. Lühr (2003), Satellite Observations of Magnetic Fields Due to Ocean Tidal Flow, *Science*, *299*(5604), 239–241, doi:10.1126/science.1078074.

van Hazendonk, C., L. Baddeley, K. Laundal, and D. Lorentzen (2025), A statistical study of optical signatures of high-latitude Pc5 waves, *Journal of Atmospheric and Solar-Terrestrial Physics*, *274*, 106,585, doi:10.1016/j.jastp.2025.106585.

van Hazendonk, C. M., L. Baddeley, K. M. Laundal, and J. L. Chau (2024), Detection and Energy Dissipation of ULF Waves in the Polar Ionosphere: A Case Study Using the EISCAT Radar, *Journal of Geophysical Research: Space Physics*, *129*(7), e2024JA032,633, doi:10.1029/2024JA032633.

Vasyliūnas, V. M. (2005), Meaning of ionospheric Joule heating, *Journal of Geophysical Research*, *110*(A2), A02,301, doi:10.1029/2004JA010615.

Vasyliūnas, V. M. (2012), The physical basis of ionospheric electrodynamics, *Annales Geophysicae*, *30*(2), 357–369, doi:10.5194/angeo-30-357-2012.

Verkhoglyadova, O. P., X. Meng, A. J. Mannucci, and R. M. McGranaghan (2018), Semianalytical Estimation of Energy Deposition in the Ionosphere by Monochromatic Alfvén Waves, *Journal of Geophysical Research: Space Physics*, *123*(6), 5210–5222, doi:10.1029/2017JA025097.

Virtanen, I. I., B. Gustavsson, A. Aikio, A. Kero, K. Asamura, and Y. Ogawa (2018), Electron Energy Spectrum and Auroral Power Estimation From Incoherent Scatter Radar Measurements, *Journal of Geophysical Research: Space Physics*, *123*(8), 6865–6887, doi:10.1029/2018JA025636.

Virtanen, I. I., H. W. Tesfaw, A. T. Aikio, R. Varney, A. Kero, and N. Thomas (2024), F_1 Region Ion Composition in Svalbard During the International Polar Year 2007–2008, *Journal of Geophysical Research: Space Physics*, *129*(3), e2023JA032,202, doi:10.1029/2023JA032202.

Wahlund, J.-E., H. J. Opgenoorth, I. Häggström, K. J. Winser, and G. O. L. Jones (1992), EISCAT observations of topside ionospheric ion outflows during auroral activity: Revisited, *Journal of Geophysical Research: Space Physics*, *97*(A3), 3019–3037, doi:10.1029/91JA02438.

Wang, B., Y. Nishimura, M. Hartinger, N. Sivadas, L. L. Lyons, R. H. Varney, and V. Angelopoulos (2020), Ionospheric Modulation by Storm Time Pc5 ULF Pulsations and the Structure Detected by PFISR-THEMIS Conjunction, *Geophysical Research Letters*, *47*(16), doi:10.1029/2020GL089060.

Whiter, D. K., B. Gustavsson, N. Partamies, and L. Sangalli (2013), A new automatic method for estimating the peak auroral emission height from all-sky camera images, *Geoscientific Instrumentation, Methods and Data Systems*, *2*(1), 131–144, doi:10.5194/gi-2-131-2013.

Witasse, O., J. Lilensten, C. Lathuillère, and P. Blelly (1999), Modeling the OI 630.0 and 557.7 nm thermospheric dayglow during EISCAT-WINDII coordinated measurements, *Journal of Geophysical Research: Space Physics*, *104*(A11), 24,639–24,655, doi:10.1029/1999JA900260.

Yeoman, T. K., D. Y. Klimushkin, and P. N. Mager (2010), Intermediate-m ULF waves generated by substorm injection: a case study, *Annales Geophysicae*, *28*(8), 1499–1509, doi:10.5194/angeo-28-1499-2010.

Yin, Z., X. Zhou, Z. Hu, Q. Zong, J. Liu, C. Yue, S. Wang, X. Zhao, H. Yang, and B. Li (2023), Multi-Band Periodic Poleward-Moving Auroral Arcs at the Postdawn Sector: A Case Study, *Journal of Geophysical Research: Space Physics*, *128*(9), e2023JA031,516, doi:10.1029/2023JA031516.

Zhang, B., and O. J. Brambles (2021), Polar Cap O^+ Ion Outflow and Its Impact on Magnetospheric Dynamics, in *Geophysical Monograph Series*, edited by C. Huang, G. Lu, Y. Zhang, and L. J. Paxton, 1 ed., pp. 83–114, Wiley, doi:10.1002/9781119815617.ch5.

Papers

Paper I

Detection and Energy Dissipation of ULF Waves in the Polar Ionosphere: A Case Study Using the EISCAT Radar

van Hazendonk, C. M., Baddeley, L., Laundal, K. M., Chau, J. L.
Journal of Geophysical Research: Space Physics, **129/7**, (2024)
doi: 10.1029/2024JA032633

AGU ADVANCING EARTH AND SPACE SCIENCES

JGR Space Physics

RESEARCH ARTICLE
10.1029/2024JA032633

Detection and Energy Dissipation of ULF Waves in the Polar Ionosphere: A Case Study Using the EISCAT Radar

C. M. van Hazendonk[1,2], L. Baddeley[1], K. M. Laundal[2], and J. L. Chau[3]

[1]Department of Arctic Geophysics, University Centre in Svalbard, Longyearbyen, Norway, [2]Department of Physics and Technology, University of Bergen, Bergen, Norway, [3]Leibniz Institute of Atmospheric Physics at the University of Rostock, Kühlungsborn, Germany

Key Points:

- We present a new method to detect and reconstruct ULF waves in ISR data with a 2D fast-Fourier transform
- We estimate ionospheric energy dissipation rates due to EM and kinetic energy sources using the new method
- We find that kinetic and EM energy rates are of similar magnitude and should both be included in ionospheric energy deposition by ULF waves

Correspondence to:
C. M. van Hazendonk,
charlottva@unis.no

Citation:
van Hazendonk, C. M., Baddeley, L., Laundal, K. M., & Chau, J. L. (2024). Detection and energy dissipation of ULF waves in the polar ionosphere: A case study using the EISCAT radar. *Journal of Geophysical Research: Space Physics*, *129*, e2024JA032633. https://doi.org/10.1029/2024JA032633

Received 13 MAR 2024
Accepted 22 JUN 2024

Author Contributions:
Conceptualization: C. M. van Hazendonk, L. Baddeley, K. M. Laundal
Formal analysis: C. M. van Hazendonk
Funding acquisition: L. Baddeley
Investigation: C. M. van Hazendonk, L. Baddeley, K. M. Laundal
Methodology: C. M. van Hazendonk, L. Baddeley, K. M. Laundal, J. L. Chau
Project administration: L. Baddeley
Software: C. M. van Hazendonk, J. L. Chau
Supervision: L. Baddeley, K. M. Laundal
Validation: C. M. van Hazendonk
Visualization: C. M. van Hazendonk
Writing – original draft: C. M. van Hazendonk
Writing – review & editing: C. M. van Hazendonk, L. Baddeley, K. M. Laundal, J. L. Chau

Abstract Ultra-low frequency (ULF) waves transfer energy and momentum into the ionosphere-thermosphere system. To quantify this energy, this paper first presents a new method to quantitatively detect ULF waves in Incoherent Scatter Radar (ISR) data based on 2D fast-Fourier transforms and subsequent reconstruction of the wave. In parallel with other data sets, including optical, magnetometer, satellite, and models, we present the first full ionospheric energy dissipation rates for a ULF wave, split into electromagnetic (EM) and kinetic fluxes. The EM energy deposition is calculated from the use of the Poynting theorem, looking at Joule and frictional heating rates, where both rates show the same order of magnitude (1.24×10^{13} and 7.3×10^{12} J) respectively when integrated over the wave lifetime of 2 hr 15 min and an area of 4° magnetic latitude × 74° magnetic longitude. However, contrary to the common assumption that the EM flux is dominant, we determined the kinetic flux, to be almost equal in magnitude (8.7×10^{12} J). This indicates that previous papers might have underestimated the total energy dissipation by ULF waves. Compared to the substorm energy budget, we find that locally, the ULF wave event studied here makes up approximately 10% of a typical substorm cycle budget.

Plain Language Summary The Earth's magnetic field lines can move back and forth regularly, like waves on a guitar string. When this happens on the time scale of minutes, we call these ultra-low frequency (ULF) waves. ULF waves play an important role in the transfer of energy from the Earth's magnetic field to the Earth's upper atmosphere. In this study, we developed a new method to detect ULF waves in radar data to obtain information about the wave. By combining several data sets, such as radar, optical, satellite, and magnetic field measurements, we were then able to determine how much energy is being transferred in one ULF wave event. Both electromagnetic and kinetic energy are important in this transfer of energy.

1. Introduction

Ultra-low frequency (ULF) magnetohydrodynamic (MHD) waves contribute to magnetosphere—ionosphere (M-I) coupling by the transfer of momentum and energy into the Earth's ionosphere. This can appear as ion frictional heating in the ionosphere—thermosphere (I-T) system, and enhancement and/or modulation of ionospheric parameters such as the electron density. Driving mechanisms of ULF waves are diverse and often divided into external and internal sources with respect to the magnetosphere. External sources include the Kelvin-Helmholtz instability (KHI) on the flanks of the magnetopause, interplanetary shocks, high solar wind speeds, or peaks in the dynamic pressure of the solar wind, while internal sources can be wave-particle interactions from the radiation belts among others (Hartinger et al., 2022). Due to the many drivers, ULF waves can occur in all magnetic local time sectors. More information, including an extensive introduction to ULF waves as well as a recent overview of outstanding questions can be found in Hartinger et al. (2022) and references herein.

ULF wave observations are often limited to satellite observations or ground-based instrumentation such as magnetometers (e.g., Berube et al., 2003; Hynönen et al., 2020; D. M. Wright et al., 2001). However, attenuation in the ionosphere proves to be a challenge to measure (high-m) ULF waves with ground-based magnetometers (D. M. Wright & Yeoman, 1999). Satellites, on the other hand, do not provide a continuous measurement of one region due to their orbital movement. Additionally, there is a lack of (satellite) measurements between 100 and 200 km altitude, while Joule heating and auroral particle precipitation maximize in these regions (Palmroth et al., 2021; Sarris et al., 2020).

Incoherent scatter radars (ISRs) and coherent scatter radars (CSRs) are able to overcome both obstacles using direct measurements of ionospheric parameters combined with fixed field-of-views (FOVs). ULF waves, including high-m ones, have been detected in the line-of-sight velocity (v_i) of the Super Dual Auroral Radar Network (SuperDARN) (Chisham et al., 2007) (e.g., Fenrich et al., 1995, 2019; Kozyreva et al., 2020; Rae et al., 2007; Shi, Baker, et al., 2018; Shi, Ruohoniemi, et al., 2018), as well as in different parameters of ISRs such as electron density (N_e) (Belakhovsky et al., 2016; Pilipenko et al., 2014; Wang et al., 2020), and electron and/or ion temperature (T_e and T_i) (Baddeley et al., 2017).

In order to investigate the role of ULF waves in M-I coupling and to quantify their ionospheric energy deposition, altitude profiles of ionospheric parameters such as N_e, T_e, T_i, and v_i are essential. Whilst SuperDARN can provide measurements of v_i in the F-region ionosphere, only ISRs can provide these parameters as altitude profiles. This makes ISRs the only instrument capable of providing the full characterization of energy dissipation due to ULF waves. Often, ISR data can be integrated with a <1 min temporal resolution to satisfy the need for the study of shorter period wave events and capture changes in ULF waves in more detail (Hartinger et al., 2022).

Energy enters the I-T system in two forms, electromagnetic (EM) as described by the Poynting flux, and kinetic via precipitating particles (Huang, 2021). More information on both energy forms and how they are determined in this paper can be found in Section 2. In short, the energy entering the I-T system consists of an EM component, which is then dissipated through mechanisms such as Joule and frictional heating, and a kinetic energy component dissipated through ionization and thermal heating of the plasma. The EM component is, in the literature, often assumed to be entirely represented through measurements of Joule heating and Joule heating is thus the only term included in many studies quantifying energy deposition of ULF waves (e.g., Baddeley et al., 2005; Hartinger et al., 2015; Rae et al., 2007). However, Thayer and Semeter (2004) and A. N. Wright et al. (2003) suggested that the kinetic energy term can be (equally) important. More specifically, the EM and kinetic energy terms could be coupled by adiabatic energy conversion, in which case the Poynting flux provides the energy source for aurorally accelerated electrons which are observed as kinetic energy flux in the ionosphere (Thayer & Semeter, 2004).

The relatively few papers calculating energy dissipation rates, especially for ULF waves, focus on only one of the heating rates, and/or depend on many assumptions due to a lack of measurements. Examples include estimating a value for the (altitude-integrated) Pedersen conductivity (Baddeley et al., 2005; Rae et al., 2007), assuming direct transfer of the Poynting flux into Joule heating (at one altitude) (Hartinger et al., 2015), and/or neglecting neutral winds (Fenrich et al., 2019; Rae et al., 2007).

As pointed out, ISR data provide an opportunity to calculate heating rates more accurately due to the direct measurements of N_e, T_e, T_i, and v_i. However, due to the complicated nature of ISR data (different experiment types, multiple pointing directions, variable spatial and temporal resolution, poor signal-to-noise ratio), ULF waves are often only found by visual inspection. In addition, ISRs are not measuring continuously, and are thus not automatically recording data during events found in different data sources (e.g., magnetometers, SuperDARN, and satellite measurements). This study thus presents a new method to quantitatively detect ULF waves in ISR data, specifically focusing on data sets where the radar pointing direction is such that it allows a large coverage in latitude.

Using this method, in parallel with other data sets, we show quantitative detection of the wave, therefore enabling the first direct measurements of the full ionospheric energy dissipation rates in the I-T system for a ULF wave. The energy dissipation rates calculated in this paper are split into an EM and a kinetic component to see how both energy sinks are connected. This will enable a better understanding of the energy dissipation governed by ULF waves and their role in the global I-T system.

In the next sections, the background theory on energy deposition rates is discussed, after which the data sources and the detection method are presented. The detection method is then demonstrated via a case study and the energy deposited by this ULF wave event is determined and compared to previous literature. All in all, this paper shows unique observations of ULF waves in ISR data, in which the wave and its energy deposition are visible across all ionospheric parameters, allowing to determine energy dissipation by ULF waves with more temporal and spatial variability, and less assumptions than before.

2. Background Theory

The EM energy is usually described by the differential form of the Poynting flux:

$$\nabla \cdot \vec{S} + \frac{\partial W}{\partial t} + \vec{j} \cdot \vec{E} = 0, \tag{1}$$

where S is the Poynting flux vector with $\vec{S} = \frac{1}{\mu_0}\left[\vec{E} \times \vec{B}\right]$, $\frac{\partial W}{\partial t}$ gives the change in the EM energy density for the magnetic and electric fields, W, over time, $\vec{j}$ the current density (A/m^2), and $\vec{E}$ the electric field. Together $\vec{j} \cdot \vec{E}$ represent the energy conversion. In the context of the results in this paper, the wavelength of ULF waves is much larger than the electron inertial length and their frequency is smaller than the ion gyro frequency. We can thus assume that our Alfvén waves are non-dispersive and we are in the quasi-static regime where $\frac{\partial W}{\partial t}$ can be neglected (Verkhoglyadova et al., 2018). In short, it is assumed that there is little change in wave energy over time compared to the change in $\vec{j} \cdot \vec{E}$.

$\vec{j} \cdot \vec{E}$ can be regarded as the rate at which EM energy is converted into mechanical energy (e.g., Strangeway, 2012). In the ionosphere, the different mechanical heating terms, known as Joule, frictional, and Ohmic heating all provide different realizations of the local energy dissipation process. Confusion in the literature between the different terms arises from their different origin, the Joule heating rate comes from MHD equations, while the frictional heating rate originates from the relative movement between individual species. The total joule heating can also be defined as the sum of the frictional heating of all different species under steady-state conditions (e.g., Thayer & Semeter, 2004). In this paper, we calculate the Joule and frictional heating rates with the equations described by Thayer and Semeter (2004). Even though both heating rates should be similar, assumptions regarding some of the input parameters (e.g., the use of models for neutral particle densities and ionospheric constituents) can yield different results. Joule heating is calculated using

$$\vec{j} \cdot \vec{E'} \approx \sigma_p E'^2_{\perp}, \tag{2}$$

where $E'_{\perp}$ is the electric field perpendicular to the magnetic field in the frame of reference of the neutral gas, and σ_p the Pedersen conductivity. $E'_{\perp}$ is estimated based on direct ISR measurement of the ion line-of-sight velocity, v_i, as will be explained in Section 4.2. For the Joule heating rate, Equation 2, the Pedersen conductivity is calculated using

$$\sigma_p = \frac{eN_e}{B}\left(\frac{\nu_{en}\omega_e}{\omega_e^2 + \nu_{en}^2} + \frac{\nu_{in}\omega_i}{\omega_i^2 + \nu_{in}^2}\right), \tag{3}$$

where e is the electrostatic charge, N_e is the electron density, B the magnetic field strength, ν_{en} and ν_{in} the collision frequency between respectively electrons and neutrals or ions and neutrals, and ω_e and ω_i the electron and ion gyrofrequency. In this paper, we use the equations for ν_{en} and ν_{in}, where the first depends on T_e and the latter on T_i and T_n, as given by Schunk and Nagy (2009) for a realistic ionosphere dominated by N_2, O_2, and O species. For calculation of the Pedersen conductivity, direct ISR measurements of N_e, T_e, and T_i are used in combination with International Geomagnetic Reference Field (IGRF) values for B and neutral densities and temperatures from the NRLMSISE-00 model (Picone et al., 2002).

Assuming Maxwellian molecule interactions and a balance between the energy exchange and the frictional heating, $\frac{\delta E_i}{\delta t} = 0$, which is reasonable below approximately 400 km, leads to a frictional heating rate described as

$$\frac{\delta E_n}{\delta t} = \frac{3k_B}{m_n}\sum_i N_i m_i \nu_{in}(T_i - T_n), \tag{4}$$

where E_n is the energy of neutral species, k_B the Boltzmann constant, N_i, m_i, and T_i respectively number density, mass, and temperature of the ion species i, ν_{in} is the ion-neutral collision frequency, and m_n and T_n are the mass and temperature of neutral species n. For a more detailed derivation, see Thayer and Semeter (2004). To calculate the frictional heating using Equation 4, direct ISR measurements provide T_i, while neutral temperatures come from the NRLMSISE-00 model, and the ion densities from the International Reference Ionosphere 2016 (IRI-2016) model (Bilitza, 2018). The frictional heating is determined between 100 and 400 km.

The kinetic energy source consists largely of precipitation particles. In terms of energy dissipation, these can be considered as two populations: low energy (≤100 eV), and high energy (≥100 eV). The ionization energy deposition rate (related to the high energy population), can be derived from assuming a balance between production and loss in the continuity equation, (e.g., Thayer & Semeter, 2004) and can be written as

$$Q_p = W_{ion}\alpha_{eff}N_e^2, \tag{5}$$

where Q_p is the deposited energy, W_{ion} is the average energy per ion-electron pair produced, α_{eff} is the effective recombination coefficient, and N_e the electron density as directly measured by ISR. W_{ion} is approximately 35.5 eV between 80 and 200 km altitude. To calculate the effective recombination coefficient, α_{eff}, in the ionization energy deposition rate (Equation 5), the definition given by Brekke (2013) is used:

$$\frac{1}{\alpha_{eff}} = \frac{1}{\beta}\left(\frac{k_1[N_2]}{\alpha_1} + \frac{k_2[O_2]}{\alpha_2}\right) \tag{6}$$

where $\beta = k_1[N_2] + k_2[O_2]$. The reaction rates, α_1, α_2, k_1, and k_2, partly depend on T_e, T_i, and T_n as provided by direct ISR measurements and the NRLMSISE-00 model. Full equations for the reaction rates are given in Table 4.4 of Brekke (2013).

In addition, low energy electrons (<100 eV), sometimes known as soft precipitation (Lynch et al., 2007) can also contribute to general thermal heating. This energy is deposited at higher altitudes via Coulomb collisions and thermal conduction. In this case, the electron temperature can be increased without accompanying increases in electron density. Due to the lack of energy sinks at higher altitudes, electrons with low energies can yield large increases in T_e (Lynch et al., 2007). To get an estimate of the energy involved in this process, the average kinetic energy of an electron with 3 degrees of freedom is used, which is described by $E_{av} = \frac{3}{2}k_B T_e$, following the equipartition theorem. By determining the difference in kinetic energy between hotter, corresponding to ULF wavefronts, and colder electron populations, we can get an estimate of these thermal energy contributions.

3. Data

For this study, we are using ISR data from the European Incoherent Scatter (EISCAT) network on 18 December 2017 to demonstrate the detection method. More specifically, the EISCAT radars in Tromsø (VHF and UHF radars), located at 69.58°N, 19.23°E geographic; 66.73°, 102.18° geomagnetic coordinates, and Svalbard (ESR), (78.09°N, 16.02°E geographic; 75.43°, 110.68° geomagnetic coordinates), provide data about electron density, N_e, electron and ion temperature, T_e and T_i, and line-of-sight velocity, v_i. The VHF radar was running the entire day in low elevation pointing toward geographic north, while the UHF (00:00–04:00 UT) and ESR (entire day) were both pointing aligned parallel to the geomagnetic field (in a so called field-aligned pointing direction). In single beam mode, the VHF radar has an east/west beam width of 0.6°, corresponding to 1 (4.2) km at 100 (400) km altitude. Figure 1 shows the location of the radar beams as well as co-located instruments.

The EISCAT data, in combination with the NRLMSISE-00 model and the IRI-2016 model are used to characterize energy deposition rates. Both models are calculated for each EISCAT data point in time. To support ULF wave characteristics we use ground magnetometer data, all-sky images of the aurora from the Longyearbyen all-sky imager (ASI) from the University of Oslo (UiO) (co-located with the ESR), and satellite UV images of the aurora from the Special Sensor Ultraviolet Spectrographic Imager (SSUSI) onboard the Defense Meteorological Satellite Program (DMSP) spacecraft. We use two different sources of magnetometer data, 10 s resolution data from the International Monitor for Auroral Geomagnetic Effects (IMAGE) magnetometer network to study the latitudinal variations of the ULF wave and 1 min resolution data from SuperMAG (Gjerloev, 2012) to assess the longitudinal extent of the ULF waves. The locations of these instruments are shown in Figure 1. In addition, solar wind data from DSCOVR (NOAA Space Weather Prediction Center, 2016) is used to determine possible generation mechanisms of the ULF waves. Data sources for all instruments are provided in Data Availability Statement of the paper.

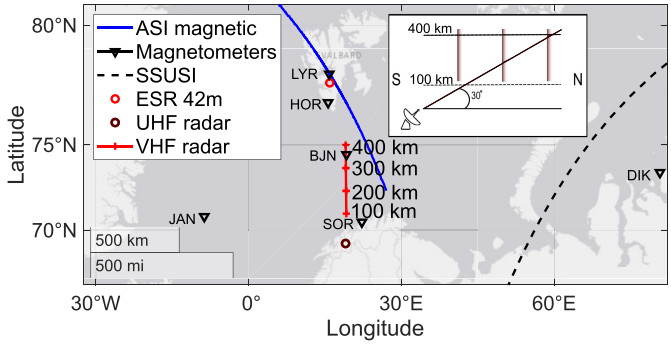

Figure 1. Locations of the geomagnetic meridian of the Longyearbyen all-sky imager (ASI), relevant magnetometers and their corresponding name, SSUSI overpass, and EISCAT radar beams are shown in geographic coordinates. The locations of the ESR 42 m and UHF radar, both pointing in field aligned direction, are centered at 250 km altitude, while the VHF radar beam is shown between 100 and 400 km altitude. On the top right, a schematic representation of the VHF radar beam at low elevation with dark red wavefronts in the beam is shown, indicating that each altitude corresponds to a different latitude and that multiple wavefronts can be seen in the radar beam simultaneously.

4. Methods

This section describes the detection method developed for ULF waves in EISCAT data. As mentioned previously, due to the nature of ISR data, most ULF waves are identified and parameterized (e.g., duration, spatial extent etc.) using visual inspection of the data. The method highlighted here provides the first quantitative based technique of identifying such structures in the data sets. Once the ULF wave is identified, the energy dissipation rates are calculated. In addition, the various caveats and assumptions relating to this particular data set (low elevation angle observations) are discussed.

4.1. Detection of ULF Waves in EISCAT Data With 2D FFT

EISCAT data are analyzed with an integration time of 30 s, and an altitude integration of 5 km to prepare the data for the 2D fast-Fourier transform (FFT) procedure. For the case study of 18 December 2017, this data is shown for all parameters (N_e, T_e, T_i, and v_i) in Figure 2 as a function of time and of both altitude and magnetic latitude, for the time period around the ULF wave event. The data show a ULF wave manifested in multiple ionospheric parameters. The line-of-sight velocity, the parameter most often used to identify ULF waves in radar data, is oscillating between up to ±500 m/s over 69.0°–71.3° mlat, which corresponds to 130–335 km altitude. The low elevation orientation of the VHF radar means that the 2D structure of the wave field can be seen as multiple poleward propagation wavefronts, where the wave moves to higher latitudes over time as seen by the slightly slanted wavefronts, extending over 2.3° (≈250 km) in latitude. Subsequently, a high-pass filter is applied to the data by subtracting a 15 min by 30 km median window. In case of data gaps below 10 min, linear interpolation is applied (Munteanu et al., 2016). Otherwise, data on either side of the data gap have been treated separately. For detection of the ULF wave a 2D FFT procedure is used. Previously, Günzkofer et al. (2023) applied a 2D FFT to detect gravity waves in EISCAT electron density data. For the 2D FFT procedure, a 2D FFT window of 30 min by 100 km is used to detect ULF waves. The window runs in time with 15 min window overlap. Combined with the data resolution of 30 s, the 30 min temporal axis results in a frequency resolution of $\Delta f = 0.56$ mHz. An example of one such a 2D FFT window for the T_e parameter and its corresponding power spectrum are shown in Figures 3a and 3b.

To distinguish peaks from background, 2 hr of subsequent single power spectra are stacked on top of each other to form an averaged power spectrum. The window length of 30 min in combination with 15 min overlap of the individual power spectra thus result in seven single power spectra being stacked on top of each other to create one averaged power spectrum. Only peaks within a certain threshold percentage of the maximum power peak for an event are selected with a maximum of four peaks. In this way, each individual power spectrum has a maximum of four peaks and each averaged power spectrum is also limited to four peaks. The frequency ω_j, phase ϕ, wave

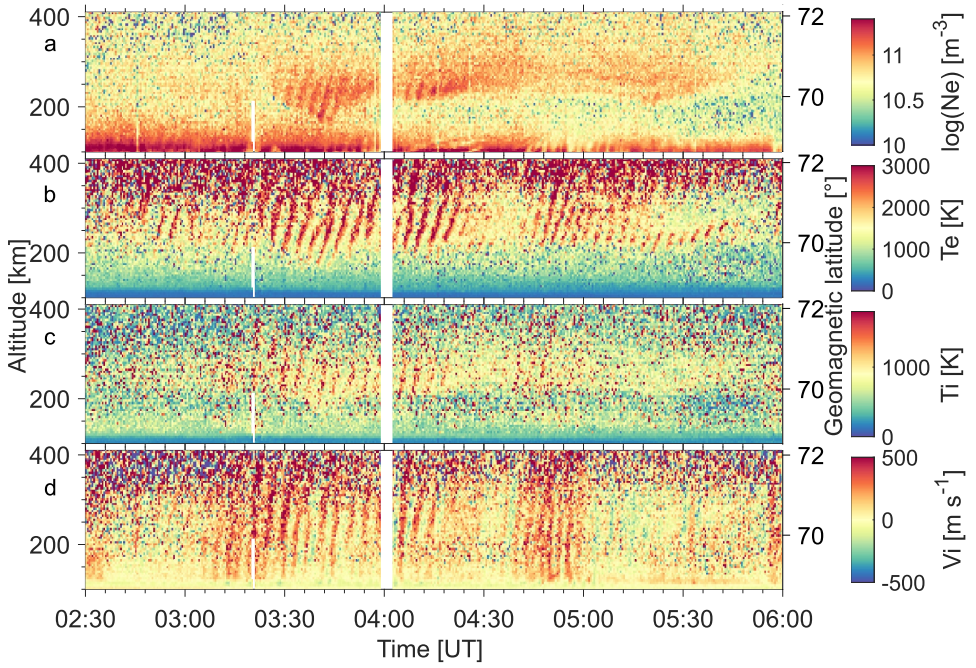

Figure 2. Data from the EISCAT VHF radar, 18 December 2017 02:30–06:00 UT, (a) electron density (log scale), (b) electron temperature, (c) ion temperature, and (d) ion velocity, plotted as a function of altitude (left) and geomagnetic latitude (right).

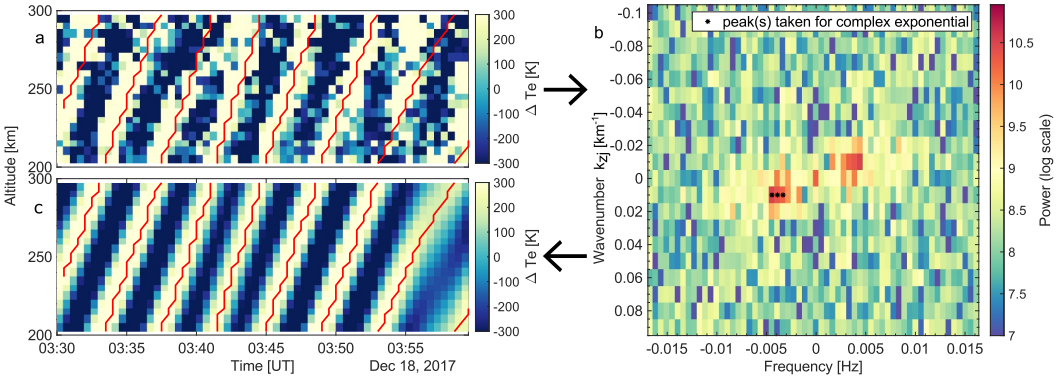

Figure 3. Reconstruction of the ULF wave for the window between 03:30 and 04:00 UT on 18 December 2017 based on electron temperature, (a) high-pass filtered EISCAT VHF data between 200 and 300 km with reconstructed wavefronts overlaid in red, (b) power spectrum from the 2D FFT in which the peaks used for reconstruction are highlighted with asterisks and (c) the real part of the reconstructed complex wave using Equation 7 with reconstructed wavefronts overlaid in red.

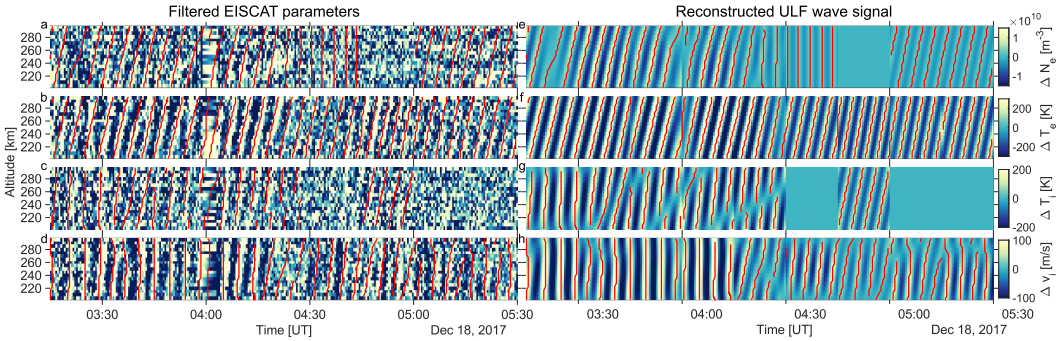

Figure 4. A reconstruction of the ULF wave in all parameters for the ULF event on 18 December 2017 between 03:15 and 05:30 UT. The panels on the left (a–d) show the high-pass filtered EISCAT VHF data between 200 and 300 km altitude. The panels on the right (e–h) show the real part of the concatenated reconstructed complex wave for the same altitude range. In all panels, the reconstructed wavefronts have been overlaid in red. Panels (a and e) correspond to the electron density, N_e, panels (b and f) to the electron temperature, T_e, panels (c and g) to the ion temperature, T_i, and panels (d and h) to the ion velocity, v_i.

number k_{zj}, and amplitude A_j of each detected peak j in the power spectrum are used to reconstruct the complex wave using

$$\sum A_j \exp(i\phi)\exp\big(i(\omega_j t - k_{zj} z)\big), \tag{7}$$

where t is the reconstructed time in seconds and z the altitude in km at which the reconstruction takes place. The real part of the reconstructed ULF wave power spectrum is then shown in Figure 3c. Wavefronts are defined as the location where a phase shift occurs in the reconstructed spectrum and are overlaid in red in Figures 3a and 3c. Subsequently, the 30 min reconstructed intervals are concatenated for the entire duration of the ULF wave event. The 15 min window overlap is overcome by taking the average wave function at each moment in time. The wave needs to be detected without interruption for over an hour to qualify as ULF wave event. This method manages to detect the wave, which can be visually identified in Figure 2, as can be seen from the comparison between Figures 3a and 3c. The full detection of the wave is then shown in Figure 4 for all ionospheric parameters. In our example, we use the electron temperature as main parameter for wave detection, and the peaks in the corresponding power spectra need to be within a threshold of 85% of the maximum peak. Using this initial wave detection in the electron temperature parameter, it is possible to restrict the frequency range over which ULF waves are searched for in the other parameters; 3–5.5 mHz in this case. In addition, we relax the detection threshold for the remaining parameters to 65%.

Different EISCAT parameters can be used to detect the ULF waves depending on the waves properties and these EISCAT parameters are directly reflected in the different heating rates as defined by Equations 2, 4, and 5. Note that some of the parameters can be anti-correlated, such as T_i with both N_e and T_e, and that the wave is not equally apparent in all parameters, due to the various energy sources affecting them differently. The reconstructed wave can thus have different temporal and spatial properties depending on which parameter has been used for detection as evidently shown in Figure 4. Ultimately, the detection algorithm provides a mathematical identification of the wavefronts in the distinct ionospheric radar parameters.

4.2. Energy Dissipation

In our case study, the VHF radar points in low elevation to observe wave structures. This means that multiple wavefronts can be seen in the radar beam simultaneously at different altitudes/latitudes as schematically shown by the red waves in the diagram in Figure 1. Therefore, we assume that measurements taken in the F-region (above 160 km) in one wavefront can be applied to another wavefront at a different location occurring at the same time, providing a full altitude profile for the two wavefronts at any given time. Since two wavefronts are separated by approximately 1° in latitude (100 km) and since the radar parameters uniformally vary throughout the wave, we are confident that this approximation is valid. Secondly, electron density measurements in the E-region, close to the

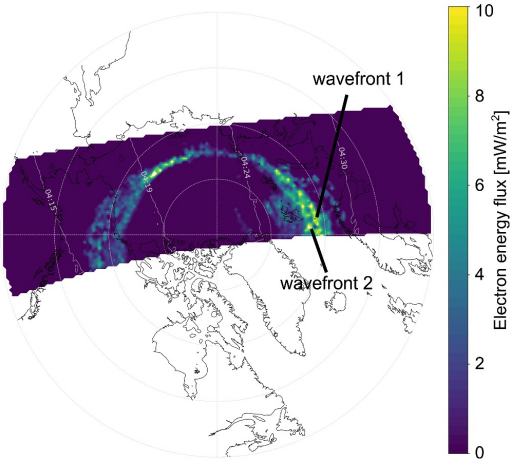

Figure 5. An UV image from the SSUSI instrument onboard the DMSP F17 spacecraft as taken during an overpass centered on 18 December 2017 04:23:00 UT. The colorscale gives the integrated electron energy flux (mW/m^2). The two wavefronts are visible as marked with wavefront 1 and 2. The image, created by scanning with a 1D cross-track pixel array, displays the UT of pixel arrays by gray contours.

radar location, also exhibit auroral precipitation associated with non-wave related auroral signatures, which can also be observed in the SSUSI data (Figure 5) as diffuse, medium flux, emissions toward the equatorward edge of the dawn side main oval. Thus, it is impossible to directly identify wave signatures at E-region altitudes in the electron density. However, precipitation signatures in the 630.0 nm channel of the ASI, projected at 250 km altitude, indicate soft F-region precipitation, a signature we also observe in the electron temperature.

We estimate the electric field, $E'_\perp$ as $|E'_\perp| = |v_i| \cdot |B|$, where v_i is the line-of-sight velocity as measured by EISCAT, and B is the total magnetic field from the IGRF model. Since the beam is pointing northwards at low-elevation, its alignment is almost perpendicular to the magnetic field, and contributions from field-aligned ion velocity components can assumed to be small (McCrea et al., 2000). Therefore, our estimate of E' can be assumed to underestimate the actual electric field, since it is based on only one component of the perpendicular velocity. As a consequence, the Joule heating will be underestimated as well. At altitudes of between 100 and 130 km, the ions are expected to move along with the neutrals. As seen in Figure 2d, since $v_i \sim 0$ at these altitudes, we can thus assume the neutral velocities to also be small. From 160 km upward we assume that the ions are moving with the $E \times B$ drift and magnetic field lines are frozen-in, because the ion mobility coefficient, k_i, which is defined as the ion gyro-frequency over the ion-neutral collision frequency, $k_i = \frac{\Omega_i}{\nu_{in}}$, exceeds 10. E' is thus estimated as a function of magnetic latitude (mlat), λ, and time (e.g., $E'(\lambda, t)$) between 69.4° and 72° mlat corresponding to altitudes of 162 and 400 km, respectively. We then make the assumption that the E-field can be mapped along the field lines from the F-region into the E-region (Brekke, 2013). The Joule heating is then determined as a 3D datacube with dimensions time, magnetic latitude, and altitude.

5. Results

The ULF wave event takes place on 18 December 2017, close to winter solstice, with a Kp index of 4 and 4-, and a location between Northern Norway and Svalbard. This area and the location of all instruments included in this study can been seen in Figure 1. A substorm was recorded on the Norwegian mainland between 01:30 and 02:30 UT, preceding the ULF wave event.

5.1. Detection, Verification and Spatial Extent of ULF Waves

We applied the method as described in Section 4.1 to our ULF wave event. This resulted in a ULF wave detection between 03:15 and 05:30 UT on 18 December 2017. The complete reconstruction is shown in Figure 4. The reconstructed frequency varies between 3.3 and 4.4 mHz, with 4.4 mHz being dominant.

To determine the total amount of energy dissipated by the wave we must determine the spatial extent of the wave. In the VHF radar data, the spatial extent in latitude is largest in v_i ranging from 69.0° to 71.3° mlat, which corresponds to 130–335 km altitude. Poleward of 71.3° mlat (above 335 km), the signal-to-noise ratio does not allow clear distinction of wave signatures, whereas equatorward from 69.0° mlat (below 130 km), there is no direct measurement of the wave in any of the radar parameters. To assess the spatial extent outside of the range of the VHF radar, other EISCAT radars, the Longyearbyen ASI, ground based magnetometers, and the SSUSI instrument onboard the DMSP spacecraft are used.

The ULF wave signature is not observed in data from the UHF radar in Tromsø nor the ESR 42 m dish. As both radar dishes were pointing along the magnetic field lines, this indicates that the ULF waves do not occur at 67.1° mlat or 74.5° mlat. Therefore, the ULF waves presumably only occur in between these magnetic latitudes. The 630.0 nm channel of the ASI, shown in Figure 6, shows the presence of periodic, poleward moving auroral arcs, extending from 69.5° mlat up to between 72 and 73° mlat between 03:15 and 03:50 UT. The periodicity of these arcs is approximately 4–5 min (3.3–4.2 mHz), similar to that of the wave. It is thus assumed that the

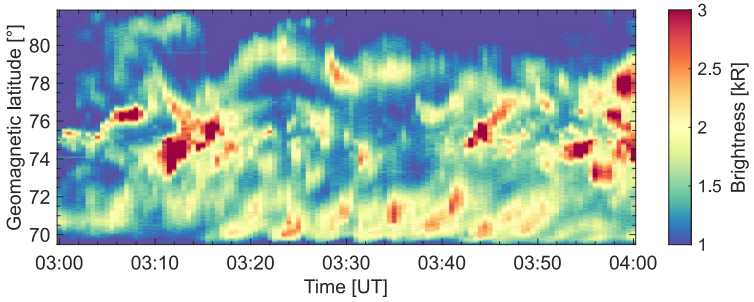

Figure 6. A keogram of the 630.0 nm channel of the Longyearbyen ASI owned by UiO between 03:00 and 04:00 UT on 18 December 2017 showing the brightness of the auroral features for magnetic latitude as a function of time.

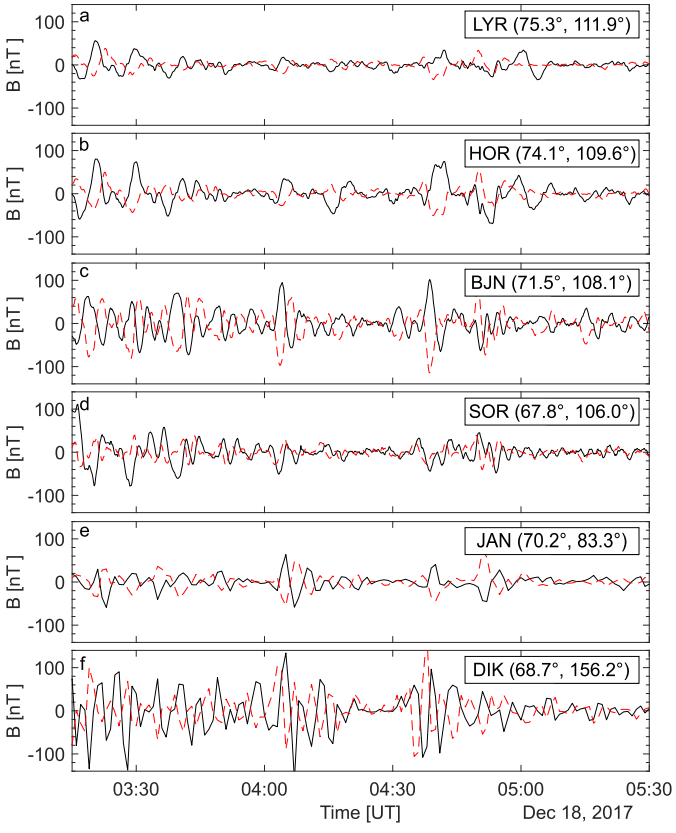

Figure 7. The X (black line) and Y (red dashed line) components of ground magnetometer stations in Longyearbyen, Hornsund, Bjørnøya, Sørøya, Jan Mayen, and Dikson with their coordinates given in (mlat, mlon).

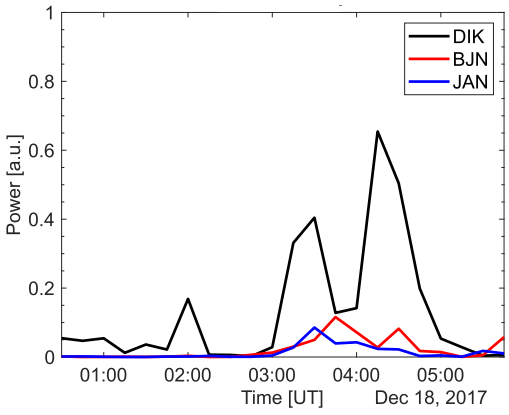

Figure 8. The wave power of the H component at 3.9 mHz as a function of time at magnetometer stations DIK, BJN, and JAN.

auroral arcs are signatures of the ULF wave in a similar manner to those previously reported by Baddeley et al. (2017) and Rae et al. (2005). The fact that the poleward propagation is observed in the ASI data, which do not have the same latitude/altitude ambiguity as the radar data, adds weight to our earlier assertion that the wave fronts are propagating in latitude. Outside this time period, the ASI data is harder to interpret due to the presence of other precipitation signatures in the 630.0 nm channel. The 557.7 nm channel, which has a low latitude cut off at 71.5° mlat, does not show a clear ULF wave signature, but it does show high energy precipitation at wave-front latitudes. Based on the available data across several instruments we thus assume a poleward boundary of 72° mlat for the entire duration of the ULF wave event.

Magnetometer data shows the presence of a ULF wave centered around Bjørnøya (71.5° mlat, 108.1° mlon) with smaller magnitude oscillations in Sørøya (67.8° mlat) and Hornsund (74.1° mlat) as shown in Figure 7. Both the X (black solid line) and the Y (red dashed line) components are plotted for stations with latitudinal variation in Figures 7a–7d, and longitudinal variation in Figures 7e and 7f. The location of all stations is plotted in Figure 1. The dominant frequency is centered at 3.9 mHz and has the largest peak to peak (nT) value between 03:15 and 04:15 UT, thus confirming the EISCAT VHF radar observations. By reviewing the ground magnetometer data further, we observe a similar magnitude in the X and Y components, as shown in Figure 7, indicating a mix of poloidal and toroidal wave modes, and thus an intermediate wave (*m*-)number. The fact that the waves are observed in ground magnetometer data indicates a (global) large scale, low-*m* wave. However, the sparsity of the ground magnetometer stations around Bjørnøya does not allow for calculation of the *m*-number, but we assume a low to intermediate *m*-number. More characteristics of toroidal and poloidal waves and their corresponding *m*-values can be found in Baddeley et al. (2017).

To assess the longitudinal extent of the ULF waves, magnetometers located between 68° and 72° mlat are used. Figure 8 shows the Pc5 wave power is largest for the Dikson magnetometer (DIK; 68.7° mlat, 156.2° mlon; easternmost magnetometer in Figure 1). In addition, signals are observed in both the Bjørnøya magnetometer, as already discussed for the latitudinal wave characteristics, and the Jan Mayen magnetometer (JAN; 70.2° mlat, 83.3° mlon; westernmost magnetometer in Figure 1). No power signatures are observed at magnetometers west from Jan Mayen and/or east from Dikson. However, it should be noted that the density of magnetometers is sparse in these regions.

To further assess the spatial extent of the ULF waves, a SSUSI overpass centered around 04:23 UT is used. As shown in Figure 5, two wavefronts, which are characterized by bright auroral emission in the direction of the auroral oval, are observed around 04:26 UT indicating the ability of SSUSI images to capture ULF waves despite their coarse scale. The equatorward edge of the auroral zone between Tromsø and Svalbard moves poleward from around 66° mlat at 03:10 UT to 69° mlat at 04:52 UT. The equatorward boundary of the ULF waves should be equal to or poleward from the auroral zone equatorward edge. In addition, we know that it should be poleward of 67.1° based on EISCAT data. Therefore, we assume a lower latitude ULF boundary of 68° mlat. All in all, the minimum surface area of the ULF wave is 4°in latitude (68°–72° mlat) and 74° in longitude (83°–157° mlon).

Table 1
An Overview of the Total Energy Dissipation Over the Wave Lifetime Determined in This Paper, Which Are Integrated Over a Time Period of 2 hr 15 min and a 4° mlat × 74° mlon Area, As Well As the Altitude-Integrated Dissipation Rate in mW/m^2

	Joule heating	Frictional heating	Ionization energy deposition
Total dissipation	1.24×10^{13} J	7.3×10^{12} J	8.7×10^{12} J
Dissipation rate	0.5–3 mW/m^2 (base level) 20 mW/m^2 (peaks)	0.5–2 mW/m^2	0.5–2 mW/m^2

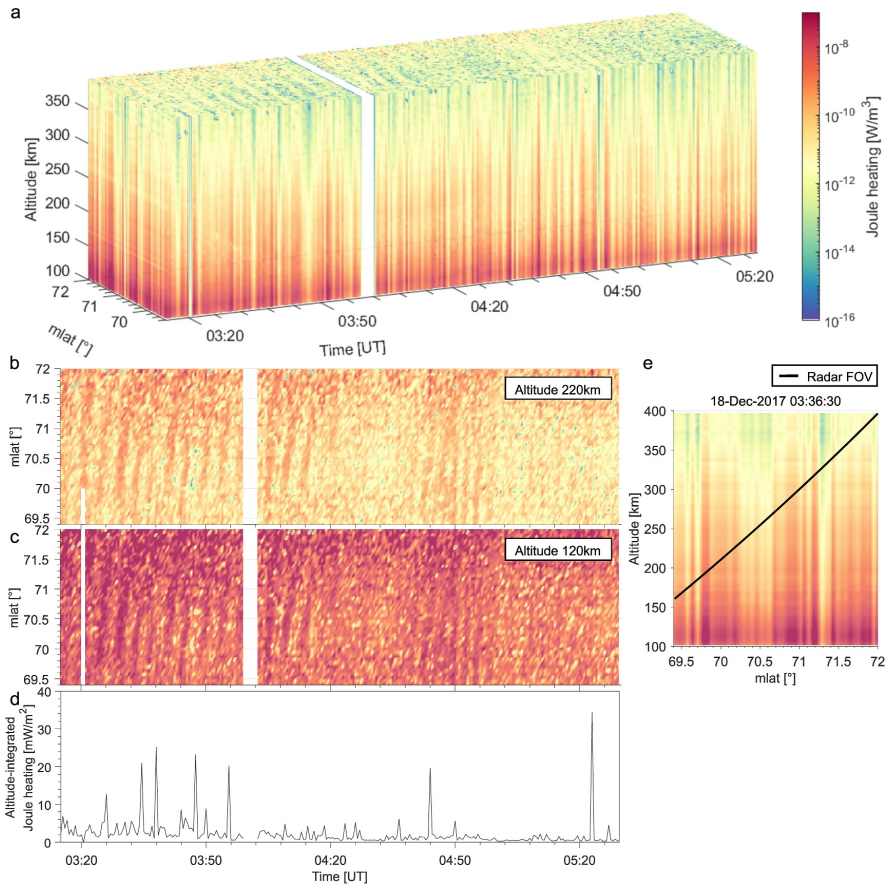

Figure 9. Panel (a) shows the Joule heating cube as a function of altitude (km), magnetic latitude (mlat) (°), and time (UT). Panels (b and c) display slices at different altitudes, where panel (b) is at 220 km, and panel (c) at 120 km altitude. Panel (d) shows the altitude-integrated Joule heating between 100 and 400 km altitude. Panel (e) shows a slice in the altitude and mlat direction at 03:36:30 UT. The black solid line represents the radar FOV.

5.2. Energy Dissipation

The energy dissipation is split into EM and kinetic, respectively, as described in Section 1. At the end of this section, Table 1 summarizes both the total dissipation of the ULF wave over its lifetime as well as the dissipation rate. This will be linked to rates reported in literature in Section 6.

5.2.1. Electromagnetic Flux

First, the Joule heating, calculated using Equation 2, is determined as a function of altitude, magnetic latitude, and time as shown in Figure 9a. For closer insights, Figures 9b and 9c show slices at different altitudes (respectively 120 and 220 km altitude) as a function of time and magnetic latitude. Figure 9e shows a slice at a particular time (03:36:30 UT) as a function of magnetic latitude and altitude. For the latter, the FOV of the radar beam is overlaid in black. As expected, Joule heating is dominant at E-region altitudes. The wave signatures can be observed most evidently in panels b and c.

To allow for better comparison with previously reported Joule heating rates, we perform an altitude integration between 100 and 400 km, which, due to the pointing direction of the radar, results in a 2D graph depending on

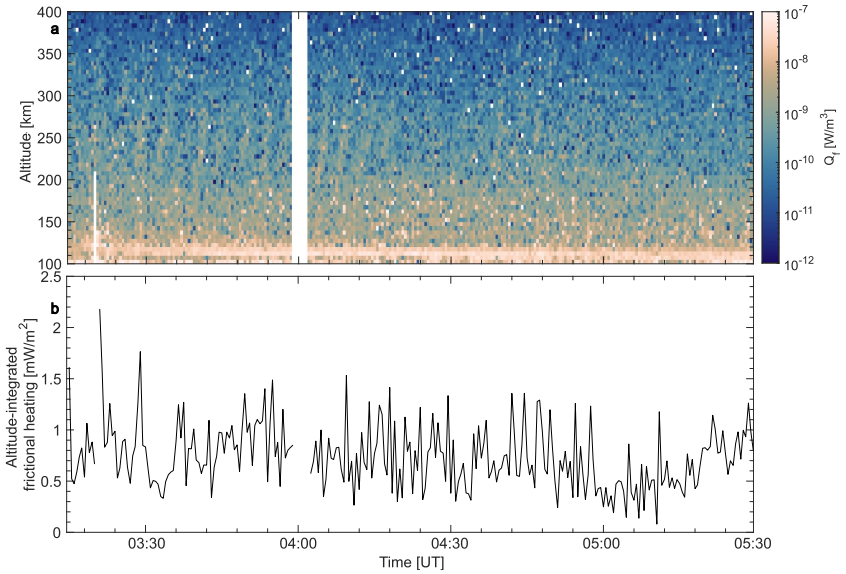

Figure 10. Panel (a) gives the frictional heating between 100 and 400 km for the ULF wave period. Panel (b) gives the altitude-integrated frictional heating between 100 and 400 km as a function of time.

magnetic latitude and time. For altitude integration, we take a mean value over all magnetic latitudes. The result is shown in Figure 9d. It can be seen that our altitude-integrated Joule heating has a base level between 0.5 and 3 mW/m^2, while it peaks at levels around 20 mW/m^2 during the more intense ULF wave signatures. In addition, the peaks in Joule dissipation rate match the peaks in wave power at Bjornøya as shown in Figure 8 with the most intense period occurring between 03:30 and 04:00 UT and a smaller peak around 04:45 UT.

Integrating the entire Joule heating data cube results in 7.7×10^9 J dissipated into the ionosphere during the ULF wave event. Extrapolating it to the minimum area of the ULF wave event (68–72° mlat and 83–157° mlon), the entire ULF wave deposits 1.24×10^{13} J into the ionosphere over its lifetime.

The frictional heating is determined as a function of time and altitude as shown in Figure 10a using Equation 4. An altitude integration between 100 and 400 km is applied for comparison to the Joule heating rates (Figure 10b). This is then integrated over the entire ULF wave area, resulting in a energy deposition of 7.3×10^{12} J over the lifetime of the wave.

5.2.2. Kinetic Energy Flux

The ionization energy deposition (>100 eV) as described by Equation 5 is integrated for the ULF wave area for an altitude between 100 and 200 km, since Equation 5 is only valid in this altitude range (Thayer & Semeter, 2004). The altitude-dependent values as a function of altitude and time as well as the altitude-integrated dissipation rate as a function of time are shown in Figures 11a and 11b, respectively. The ionization energy deposition rate lies between 0.5 and 2 mW/m^2. If we integrate over the entire ULF wave area and the lifetime of the wave, we find a total ionization energy deposition of 8.7×10^{12} J.

To estimate the contribution of lower energetic electrons (<100 eV) to the kinetic flux, we can estimate the thermal energy contributions based on the average kinetic energy of an electron $E_{av} = \frac{3}{2} k_B T_e$, and multiply this by the electron density. Since this energy (<100 eV) is usually deposited at higher altitudes, we look at 300 km to ensure sufficient altitude and a good enough signal-to-noise ratio. At 300 km, its 5%–95% percentile varies between 1 and 5 μW/m^2. Therefore, the thermal energy contributions, as seen in the electron temperature increments as shown in Figure 2b (which are the most prominent ULF wave signatures from a visual and analytical

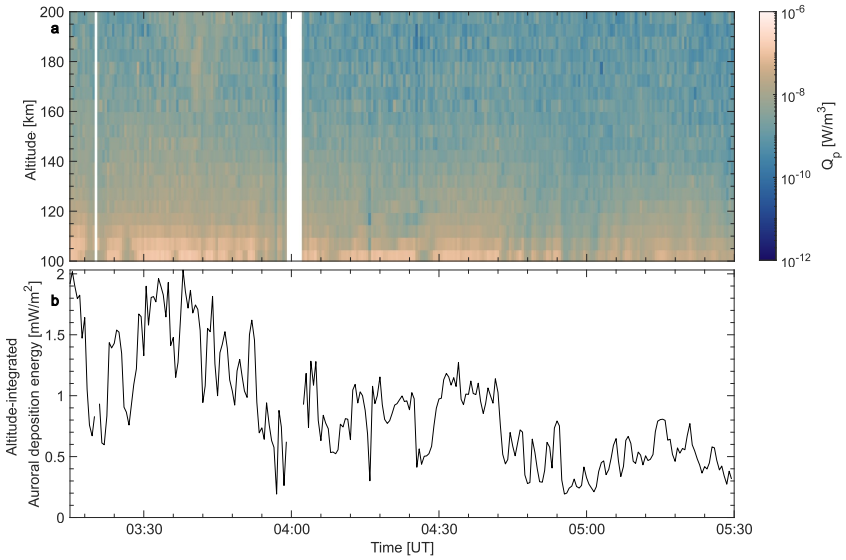

Figure 11. The ionization energy deposition plotted during the ULF event. Panel (a) gives the altitude-dependent auroral deposition (W/m^3), and panel (b) gives the altitude-integrated (between 100 and 200 km) values (mW/m^2).

perspective) result in values three orders of magnitude smaller than the contributions from the ionization energy deposition. Due to this significant difference, we decided to focus on the ionization energy (>100 eV) deposition for the quantification of the kinetic energy flux. However, low energetic electrons (<100 eV) can still have other relevant effects on other processes such as ion outflow (Lynch et al., 2007).

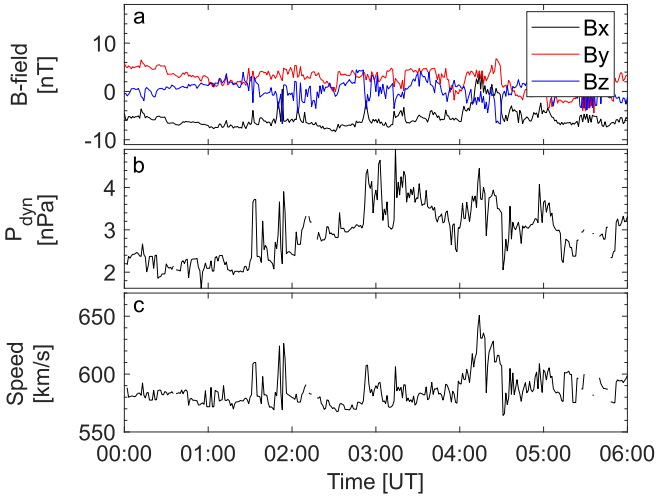

Figure 12. The magnetic field, dynamic pressure, and speed of the solar wind as measured by the DSCOVR spacecraft. In case of data gaps, the data has been supplemented with data from ACE. The data has been time shifted to the bow shock.

Table 2
A Comparison Between Results of This Paper to Literature of the Dissipation Rate (mW/m^2) and the Total Energy Dissipation by Joule Heating (J) Over the Wave Lifetime

	m-number	Dissipation rate (mW/m^2)	Integration area (° mlat × ° mlon)	Total joule heating (J)
This paper	Low/intermediate	0.5–3 (base level)	4 × 75	1.24×10^{13}
		20 (peaks)		
Rae et al. (2007)	Low	1.3 (mean)	10 × 65	8.0×10^{13}
		7.3 (peaks)		
Baddeley et al. (2005)	High	0.075	1 × 5	$\sim 10^{10}$
Baddeley et al. (2005)	High	0.68	1 × 5	$\sim 10^{11}$
Hartinger et al. (2015)	Low/intermediate[a]	0.1–1[b]	–	–
		∼10 (extremes)	–	–
Aikio et al. (2012)	No ULF waves	1–2.5 (quiet)[b]	–	–
		2.5–5 (moderate)[c]	–	–
		5–16 (high)[c]	–	–

[a]Hartinger et al. (2015) present a statistical study, but the case study indicates a mixture of modes including toroidal. [b]These rates are valid at high latitudes. [c]These are the median values between 03:00 and 06:00 UT, peak values are up to twice as large.

6. Discussion

6.1. ULF Wave Characteristics

As the ULF wave is detected between 03:15 and 05:30 UT, corresponding to approximately 06:00–08:15 magnetic local time (MLT), all observations are made in the dawn sector. The geomagnetic conditions in general are moderately active (Kp around 4), with corresponding high solar wind speeds, and some peaks in the solar wind dynamic pressure as shown in Figures 12b and 12c, respectively. The timing of the event, located on the dawn flank of the magnetopause, suggests that the driver could be the Kelvin-Helmholtz instability, due to shear flows on the flanks of the magnetosphere. Especially at high latitudes, the KHI tends to correlate with solar wind speed, thus increasing occurrence rates with faster solar wind flows (Engebretson et al., 1998; Takahashi et al., 2012). In addition, the KHI favors the dawn flank, thus causing a dawn-dusk asymmetry when the solar wind is in its usual Parker spiral orientation (Henry et al., 2017). Therefore, both the relatively high solar wind speeds as well as its location on the dawn flank make it probable that we are indeed observing KHI driven ULF waves. With the KHI we would expect duskward (anti-sunward) propagation of the wave. Unfortunately, the longitudinal coverage of magnetometer stations is too scarce to allow for calculation of the phase shifts and its propagation direction. However, as stated earlier, the fact that the wave is observed in ground magnetometer data implies it has a small to intermediate *m*-number, which is consistent with a KHI driver.

6.2. Electromagnetic Flux

Previously reported dissipation rates and total dissipated Joule heating over the lifetime of the wave can put our findings into perspective and are summarized in Table 2 for Joule heating. Aikio et al. (2012) presented a statistical study of altitude-integrated (between 80 and 180 km) Joule dissipation rates determined with the EISCAT UHF radar throughout the entire day for different geomagnetic conditions and thus not specifically related to ULF wave events. The median dissipation rates between 03:00 and 06:00 UT for different geomagnetic conditions are listed in Table 2. It can be seen in Figure 9d that the base level of our reported altitude-integrated Joule dissipation rates, which is between 0.5 and 3 mW/m^2, falls in the quiet geomagnetic conditions according to Aikio et al. (2012). At the same time, our peak altitude-integrated Joule heating values of around 20 mW/m^2 fall into the high geomagnetic activity ($Kp \geq 5^-$) category, thus exceeding the expectations when just looking at the Kp index of the event.

A recent example of Joule heating dissipation rates of ULF waves is done by Hartinger et al. (2015) providing a statistical study that uses fluxgate magnetometers and electric field instruments onboard the THEMIS spacecraft. Here, the assumption is made that the entire Poynting flux is converted into Joule heating at one altitude, and these measurements are traced down along the magnetic field lines to an altitude of 100 km in the ionosphere, resulting

in Joule heating rates between 0.1 and 1 mW/m^2 at high latitudes. Our study shows that the energy dissipation due to the kinetic flux is in the same order of magnitude as the Joule heating, thus not taking the kinetic flux into account could potentially underestimate the total energy dissipation of a ULF wave by a factor two. When comparing the Joule dissipation rates found by Hartinger et al. (2015) to the ones obtained in this paper, theirs are slightly lower for both background and peak rates. This might be due to the high spatial resolution of ISRs compared to point measurements from spacecraft, allowing us to capture more localized phenomena, and thus more precise peaks in dissipation rates.

In addition, we can also compare our total Joule dissipation over the wave lifetime with ones reported by other studies of ULF waves. To obtain total energy deposition values in the ionosphere, dissipation rates in low-*m* FLR studies are typically multiplied by a factor four to account for both hemispheres as well as the dawn and dusk flanks, while the rates in high-*m* FLR studies tend to be only multiplied by a factor two to account for both hemispheres (Rae et al., 2007). We decided to not multiply our total energy deposition, because despite most likely seeing a mix between toroidal and poloidal ULF waves with a low-/intermediate-*m* global character, local conductivities and ionospheric conditions will be different, ultimately resulting in different energy dissipation rates in both hemispheres and/or on the flanks of the magnetopause. In addition, there might be an asymmetry present between the dawn and the dusk flank due to the KHI that is presumably driving the ULF waves. For comparison, we present the values reported previously in literature adjusted to our wave duration of 2 hr 15 min and we take away their multiplication to account for the different hemispheres and/or flanks of the magnetopause.

Rae et al. (2007), using data from SuperDARN radars, obtained a total dissipation rate due to Joule heating of 9.9×10^9 W (northern hemisphere; dusk flank) by integrating over an area of 10° mlat × 65° mlon. Multiplying their energy dissipation rate with our ULF wave interval (2 hr 15 min), results in an energy deposition of 8.0×10^{13} J, exceeding our total Joule heating over the lifetime of the wave (1.24×10^{13} J) by a factor of six. However, their ULF wave is observed over an area more than twice as large as ours. Therefore, we conclude that our total rates are comparable. Local dissipation rates reported by Rae et al. (2007) vary between 0.16 and 7.3 mW/m^2 with a mean value of 1.3 mW/m^2, versus variations between 0.22 and 33.5 mW/m^2 with a mean value of 2.2 mW/m^2 in our study as shown in Figure 9d. Our slightly higher values could, again, result from the more localized features being captured by ISRs, as well as the availability of more parameters (N_e, T_e, T_i, and ν_i) in ISR data thus allowing for less assumptions in the energy deposition rates.

Baddeley et al. (2005) presented a study of two separate high-*m* wave events, which are generally known to dissipate less energy compared to low-*m* waves, partly due to their smaller dissipation area. In the calculation of the dissipation rates, Baddeley et al. (2005) assumed both electric field and integrated Pedersen conductivity to be constant. The high-*m* character of their wave events, and the smaller scale results in less energy dissipation ($\sim 10^{10}$–10^{11} J) with is consistent with our results for a larger scale, low to intermediate-*m* wave.

Lastly, we have to keep in mind that the Joule heating rates in this study are underestimated due to the assumption of a minimum electric field which is calculated using the line-of-sight velocity rather than the actual vector velocity. This could explain the fact that our base level dissipation rate of 0.5–3 mW/m^2 falls into the quiet geomagnetic condition category when comparing to Aikio et al. (2012). In addition, the magnetometer station that recorded the largest wave power for this event is located in Dikson and thus outside of the radar beam. Therefore, the actual total Joule dissipation over the lifetime of the wave is probably (slightly) larger than the reported values.

Skjæveland et al. (2017) reported altitude-resolved frictional heating rate values measured with ESR in the cusp at 200 km between 0.004 and 0.02 μW/m^3. In addition, they observe the peak in energy deposition around 120 km altitude. We observe similar rates as well as peak altitude. However, we note that the calculation heavily depends on the modeled neutral temperatures values, therefore creating a large uncertainty. For example, the IRI-2016 model assumes a thermal equilibrium between neutrals and ions below 200 km, thus finding a frictional heating rate of 0 below 200 km when Equation 4 is used. However, the total EM energy deposition over the lifetime of the wave as calculated by integrating the frictional heating dissipation rates differs only by a factor 1.7 from the one determined by the Joule heating, indicating that both are indeed valid methods to calculate the EM flux, and can thus be used to verify one another.

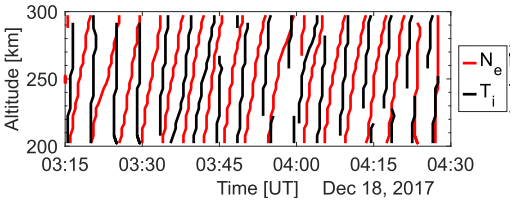

Figure 13. The wavefronts for N_e in red and T_i in black as found by the detection mechanism and shown in Figure 4 plotted on top of each other.

6.3. Kinetic Energy Flux

As the authors are not aware of any ULF wave nor ISR based kinetic energy flux calculations, we compare our auroral deposition rates to other data sources, such as SSUSI. The SSUSI instrument onboard the DMSP spacecraft gives us an estimate for the ionization energy deposition since it provides the electron energy flux. To determine this parameter, UV images of auroral emission taken during 20 min satellite overpasses of the polar region, are converted into energy fluxes for each pixel, utilizing a number of necessary assumptions including an underlying atmospheric model, a Gaussian distribution of the energies of the precipitating particles, and height-integration (Carter et al., 2020). In general, characteristic energies and mean energy values found by SSUSI tend to be higher than those obtained from direct satellite measurement (Carter et al., 2020). In our case, the same tendency is observed, as the SSUSI values range between 3 and 8 mW/m^2 as shown in Figure 5, and are thus well above the estimates in this paper of 0.5–2 mW/m^2, which rely on in situ ionospheric measurements and far less assumptions. One reason for the lower values obtained in this study is the smaller integration range between 100 and 200 km. However, since our method provides direct measurements of the relevant ionospheric parameters, and is able to capture more local phenomena, we believe that it provides a more accurate description of the ionization energy deposition.

6.4. Comparison to Substorm Energy Budget

To put the total deposited energy over the lifetime of the ULF wave into perspective, we compare it to the substorm energy deposition analysis performed by Østgaard et al. (2002). The total energy budget of the substorm includes Joule heating, U_J, and the global energy deposition by electron precipitation derived from UV- and X-ray emissions, U_A, among others. Each of them gives a combined value of energy deposited in both hemispheres. We can compare our kinetic and EM energy deposition to their values for U_A and U_J, respectively. Following a previous comparison performed by Rae et al. (2007), in which the total Joule heating deposition as obtained by Østgaard et al. (2002) has been divided by two to only take the dawn and dusk sectors in both hemispheres into account, we divide the substorm cycle budget of Østgaard et al. (2002) by a factor eight, since our study only concerns a part of the dawn flank in the northern hemisphere. In addition, we modify the substorm cycle budget to last only 2 hr 15 min to simplify comparison to the ULF wave event in this paper, resulting in EM energy deposition between 9.4 and 18 $\times$ 10^{13} J and kinetic energy deposition between 6.8 and 14 $\times$ 10^{13} J for their different substorm cycles. We can see that our values (1.2 $\times$ 10^{13} and 0.9 $\times$ 10^{13} J for respectively the EM and kinetic energy) are roughly one order of magnitude smaller. ULF wave events can thus locally make up approximately 10% of a substorm cycle budget when adjusted to only one flank in a single hemisphere. Our ULF wave area does, however, not cover the entire dawn flank, and our heating rates are most likely underestimated, both potentially increases the percentage of the ULF wave energy contribution. We note that it is hard to perform exact comparisons between large, global phenomena, such as substorms, and more localized events like this ULF wave event. However, we can use this comparison to put our heating rates into the context of a global energetic event such as a substorm, and stress that locally, ULF wave events can have significant impacts on the energy budget and the energy coupling between magnetosphere and ionosphere.

6.5. Conversion of EM and Kinetic Energy Fluxes

Thayer and Semeter (2004) describe how an anti-correlation between N_e and T_i could indicate the presence of an energy conversion boundary in the auroral acceleration region and thus the adiabatic transfer of EM energy into kinetic energy. We can measure this well below the auroral acceleration region, since electrons carry over 97% of the kinetic energy produced in the auroral acceleration region and the downward accelerated electrons provide a good assessment of the field-aligned currents associated with auroral arcs. Since we detected wavefronts in both N_e and T_i between 03:15 and 04:30 UT, as visible in Figure 4 with wavefronts overlaid in red, we can compare both parameters for this time period by plotting their wavefronts on top of each other. The result is depicted in Figure 13, and shows almost complete anti-correlation despite slightly different wave parameters. The similar magnitudes of EM and kinetic energy found in this paper further support the presence of adiabatic energy conversion in the auroral acceleration region. We have thus not only established that ULF wave energy deposition

can have a significant kinetic contribution in addition to the usually assumed to be dominant EM component, we have also shown the possibility that both energy sources are connected.

7. Conclusions, Summary, and Outlook

In this paper, we have established a new method utilizing 2D FFT analysis to detect ULF waves, thereby this is the first paper to quantitatively determine duration, frequency, and wave number for ionospheric ULF wave observations in ISR data. To demonstrate the method, we applied it to a ULF wave event on 18 December 2017. The ULF wave event is located on the dawn flank, possibly driven by the KHI. Utilizing magnetometers, an all-sky imager, SSUSI, and the IRI-2016 and NRLMSISE-00 models as complementary data sources, we then presented the energy budget, including both EM and kinetic energy, of this ULF wave event. The similar magnitude of both energy sources indicates that common energy budget assumptions for ULF waves, such as the fact that the conversion of the Poynting flux into Joule and/or frictional heating is the dominant dissipation mechanism, do not provide an accurate picture of the ionospheric effects of ULF waves. This paper is thus the first to show that the kinetic energy flux needs to be considered for the ULF wave energy budget. In addition, we show how the EM and kinetic energy fluxes are linked to each other by adiabatic energy conversion as indicated by the anti-correlation of the N_e and T_i parameters.

Total dissipation rates reported in this paper are 1.24×10^{13}, 7.3×10^{12}, and 8.7×10^{12} J for respectively Joule heating, frictional heating, and ionization energy deposition. To place the ULF wave energy deposition rates into context, we compared them to the locally dissipated substorm rates. The ULF wave energy budget amounts to around 10% of the substorm budget, thus making it a significant factor in the energy coupling between the magnetosphere and the ionosphere.

The next goal, outside the scope of this paper, is the application of this method to larger, possibly ISR, data sets allowing for statistical studies into energy dissipation of ULF waves rather than case study examples. In addition, the new EISCAT 3D system will enable us to calculate more reliable energy deposition rates of ULF waves by providing vector quantities, higher temporal resolution as well as covering a larger FOV.

Data Availability Statement

EISCAT data can be downloaded from https://madrigal.eiscat.se in hdf5 files containing already analyzed data with an integration time of 1 min. In addition, the raw data files can be downloaded from https://portal.eiscat.se/ allowing re-analyzing of the data using Guisdap as done in this paper. The newest version, Guisdap 9.2, is openly available as git repository https://gitlab.com/eiscat/guisdap9. Magnetometer data used in the assessment of the latitudinal variation of the ULF waves is downloaded from the IMAGE magnetometer network via https://space.fmi.fi/image/ (10 s time resolution). The magnetometer data for the longitudinal extent of the ULF waves is downloaded from SuperMAG via https://supermag.jhuapl.edu/ (1 min time resolution). ASI data from UiO is available via http://tid.uio.no/plasma/aurora/data.php. The DMSP F16 SSUSI data can be downloaded from the SSUSI website (http://ssusi.jhuapl.edu/). The DSCOVR data were obtained from the GSFC/SPDF OMNIWeb Plus Browser interface at https://omniweb.gsfc.nasa.gov/ftpbrowser/dscovr_merged.html.

Acknowledgments
Special thanks goes to Lasse Clausen from the University of Oslo for providing us with images taken by the Longyearbyen all-sky imager. We acknowledge EISCAT, which is an international association supported by research organizations in China (CRIRP), Finland (SA), Japan (NIPR and ISEE), Norway (NFR), Sweden (VR), and the United Kingdom (UKRI). We thank the institutes who maintain the IMAGE Magnetometer Array, for the data in this paper this specifically concerns the Tromsø Geophysical Observatory of UiT the Arctic University of Norway (Norway), and the Institute of Geophysics Polish Academy of Sciences (Poland). We thank the Arctic and Antarctic Research Institute, St. Petersburg for providing the magnetometer observations from DIK. We would like to thank Johns Hopkins University Applied Physics Laboratory for providing the DMSP/SSUSI auroral FUV data. This study was partly funded by the Norwegian Research Council under CoE contract 223252/F50 and contract 309135. Karl Laundal was also funded by the Norwegian Research Council through Grant 300844/F50 and by the European Union (ERC, DynaMIT, 101086985).

References

Aikio, A. T., Cai, L., & Nygrén, T. (2012). Statistical distribution of height-integrated energy exchange rates in the ionosphere. *Journal of Geophysical Research*, *117*(A10), A10325. https://doi.org/10.1029/2012JA018078

Baddeley, L. J., Lorentzen, D. A., Partamies, N., Denig, M., Pilipenko, V. A., Oksavik, K., et al. (2017). Equatorward propagating auroral arcs driven by ULF wave activity: Multipoint ground- and space-based observations in the dusk sector auroral oval: ULF wave-driven auroral arcs. *Journal of Geophysical Research: Space Physics*, *122*(5), 5591–5605. https://doi.org/10.1002/2016JA023427

Baddeley, L. J., Yeoman, T. K., Wright, D. M., Trattner, K. J., & Kellet, B. J. (2005). On the coupling between unstable magnetospheric particle populations and resonant high *m* ULF wave signatures in the ionosphere. *Annales Geophysicae*, *23*(2), 567–577. https://doi.org/10.5194/angeo-23-567-2005

Belakhovsky, V., Pilipenko, V., Murr, D., Fedorov, E., & Kozlovsky, A. (2016). Modulation of the ionosphere by Pc5 waves observed simultaneously by GPS/TEC and EISCAT. *Earth Planets and Space*, *68*(1), 102. https://doi.org/10.1186/s40623-016-0480-7

Berube, D., Moldwin, M. B., & Weygand, J. M. (2003). An automated method for the detection of field line resonance frequencies using ground magnetometer techniques. *Journal of Geophysical Research*, *108*(A9), 1348. https://doi.org/10.1029/2002JA009737

Bilitza, D. (2018). IRI the international standard for the ionosphere. *Advances in Radio Science*, *16*, 1–11. https://doi.org/10.5194/ars-16-1-2018

Brekke, A. (2013). *Physics of the upper polar atmosphere*. Springer Berlin Heidelberg. https://doi.org/10.1007/978-3-642-27401-5

Carter, J. A., Milan, S. E., Paxton, L. J., Anderson, B. J., & Gjerloev, J. (2020). Height-integrated ionospheric conductances parameterized by interplanetary magnetic field and substorm phase. *Journal of Geophysical Research: Space Physics*, *125*(10), e2020JA028121. https://doi.org/10.1029/2020JA028121

Chisham, G., Lester, M., Milan, S. E., Freeman, M. P., Bristow, W. A., Grocott, A., et al. (2007). A decade of the Super Dual Auroral Radar Network (SuperDARN): Scientific achievements, new techniques and future directions. *Surveys in Geophysics*, *28*(1), 33–109. https://doi.org/10.1007/s10712-007-9017-8

Engebretson, M., Glassmeier, K.-H., Stellmacher, M., Hughes, W. J., & Lühr, H. (1998). The dependence of high-latitude PcS wave power on solar wind velocity and on the phase of high-speed solar wind streams. *Journal of Geophysical Research*, *103*(A11), 26271–26283. https://doi.org/10.1029/97JA03143

Fenrich, F. R., Gillies, D. M., Donovan, E., & Knudsen, D. (2019). Flow velocity and field-aligned current associated with field line resonance: SuperDARN measurements. *Journal of Geophysical Research: Space Physics*, *124*(6), 4889–4904. https://doi.org/10.1029/2019JA026529

Fenrich, F. R., Samson, J. C., Sofko, G., & Greenwald, R. A. (1995). ULF high- and low- *m* field line resonances observed with the Super Dual Auroral Radar Network. *Journal of Geophysical Research*, *100*(A11), 21535–21547. https://doi.org/10.1029/95JA02024

Gjerloev, J. W. (2012). The SuperMAG data processing technique. *Journal of Geophysical Research*, *117*(A9), 2012JA017683. https://doi.org/10.1029/2012JA017683

Günzkofer, F., Pokhotelov, D., Stober, G., Mann, I., Vadas, S. L., Becker, E., et al. (2023). Inferring neutral winds in the ionospheric transition region from atmospheric-gravity-wave traveling-ionospheric-disturbance (AGW-TID) observations with the EISCAT VHF radar and the Nordic Meteor Radar Cluster. *Annales Geophysicae*, *41*(2), 409–428. https://doi.org/10.5194/angeo-41-409-2023

Hartinger, M. D., Moldwin, M. B., Zou, S., Bonnell, J. W., & Angelopoulos, V. (2015). ULF wave electromagnetic energy flux into the ionosphere: Joule heating implications. *Journal of Geophysical Research: Space Physics*, *120*(1), 494–510. https://doi.org/10.1002/2014JA020129

Hartinger, M. D., Takahashi, K., Drozdov, A. Y., Shi, X., Usanova, M. E., & Kress, B. (2022). ULF wave modeling, effects, and applications: Accomplishments, recent advances, and future. *Frontiers in Astronomy and Space Sciences*, *9*, 867394. https://doi.org/10.3389/fspas.2022.867394

Henry, Z. W., Nykyri, K., Moore, T. W., Dimmock, A. P., & Ma, X. (2017). On the dawn-dusk asymmetry of the Kelvin-Helmholtz instability between 2007 and 2013. *Journal of Geophysical Research: Space Physics*, *122*(12), 11888–11900. https://doi.org/10.1002/2017JA024548

Huang, C. (2021). Magnetospheric energy input to the ionosphere. In C. Huang, G. Lu, Y. Zhang, & L. J. Paxton (Eds.), *Geophysical monograph series* (1st ed., pp. 1–20). Wiley. https://doi.org/10.1002/9781119815617.ch1

Hynönen, R., Tanskanen, E. I., & Francia, P. (2020). Solar cycle evolution of ULF wave power in solar wind and on ground. *Journal of Space Weather and Space Climate*, *10*, 43. https://doi.org/10.1051/swsc/2020046

Kozyreva, O. V., Pilipenko, V. A., Bland, E. C., Baddeley, L. J., & Zakharov, V. I. (2020). Periodic modulation of the upper ionosphere by ULF waves as observed simultaneously by SuperDARN radars and GPS/TEC technique. *Journal of Geophysical Research: Space Physics*, *125*(7), e2020JA028032. https://doi.org/10.1029/2020JA028032

Lynch, K. A., Semeter, J. L., Zettergren, M., Kintner, P., Arnoldy, R., Klatt, E., et al. (2007). Auroral ion outflow: Low altitude energization. *Annales Geophysicae*, *25*(9), 1967–1977. https://doi.org/10.5194/angeo-25-1967-2007

McCrea, I. W., Lockwood, M., Moen, J., Pitout, F., Eglitis, P., Aylward, A. D., et al. (2000). ESR and EISCAT observations of the response of the cusp and cleft to IMF orientation changes. *Annales Geophysicae*, *18*(9), 1009–1026. https://doi.org/10.1007/s00585-000-1009-7

Munteanu, C., Negrea, C., Echim, M., & Mursula, K. (2016). Effect of data gaps: Comparison of different spectral analysis methods. *Annales Geophysicae*, *34*(4), 437–449. https://doi.org/10.5194/angeo-34-437-2016

NOAA Space Weather Prediction Center. (2016). *Deep space climate observatory (DSCOVR)*. NOAA National Centers for Environmental Information. https://doi.org/10.7289/V51Z42F7

Østgaard, N., Germany, G., Stadsnes, J., & Vondrak, R. R. (2002). Energy analysis of substorms based on remote sensing techniques, solar wind measurements, and geomagnetic indices. *Journal of Geophysical Research*, *107*(A9), SMP9-1–SMP9-14. https://doi.org/10.1029/2001JA002002

Palmroth, M., Grandin, M., Sarris, T., Doornbos, E., Tourgaidis, S., Aikio, A., et al. (2021). Lower-thermosphere–ionosphere (LTI) quantities: Current status of measuring techniques and models. *Annales Geophysicae*, *39*(1), 189–237. https://doi.org/10.5194/angeo-39-189-2021

Picone, J. M., Hedin, A. E., Drob, D. P., & Aikin, A. C. (2002). NRLMSISE-00 empirical model of the atmosphere: Statistical comparisons and scientific issues: Techniques. *Journal of Geophysical Research*, *107*(A12), SIA15-1–SIA15-16. https://doi.org/10.1029/2002JA009430

Pilipenko, V., Belakhovsky, V., Kozlovsky, A., Fedorov, E., & Kauristie, K. (2014). ULF wave modulation of the ionospheric parameters: Radar and magnetometer observations. *Journal of Atmospheric and Solar-Terrestrial Physics*, *108*, 68–76. https://doi.org/10.1016/j.jastp.2013.12.015

Rae, I. J., Donovan, E. F., Mann, I. R., Fenrich, F. R., Watt, C. E. J., Milling, D. K., et al. (2005). Evolution and characteristics of global Pc5 ULF waves during a high solar wind speed interval. *Journal of Geophysical Research*, *110*(A12), 2005JA011007. https://doi.org/10.1029/2005JA011007

Rae, I. J., Watt, C. E. J., Fenrich, F. R., Mann, I. R., Ozeke, L. G., & Kale, A. (2007). Energy deposition in the ionosphere through a global field line resonance. *Annales Geophysicae*, *25*(12), 2529–2539. https://doi.org/10.5194/angeo-25-2529-2007

Sarris, T. E., Talaat, E. R., Palmroth, M., Dandouras, I., Armandillo, E., Kervalishvili, G., et al. (2020). Daedalus: A low-flying spacecraft for in situ exploration of the lower thermosphere–ionosphere. *Geoscientific Instrumentation, Methods and Data Systems*, *9*(1), 153–191. https://doi.org/10.5194/gi-9-153-2020

Schunk, R., & Nagy, A. (2009). *Ionospheres: Physics, plasma physics, and chemistry* (2nd ed.). Cambridge University Press.

Shi, X., Baker, J. B. H., Ruohoniemi, J. M., Hartinger, M. D., Murphy, K. R., Rodriguez, J. V., et al. (2018). Long-lasting poloidal ULF waves observed by multiple satellites and high-latitude SuperDARN radars. *Journal of Geophysical Research: Space Physics*, *123*(10), 8422–8438. https://doi.org/10.1029/2018JA026003

Shi, X., Ruohoniemi, J. M., Baker, J. B. H., Lin, D., Bland, E. C., Hartinger, M. D., & Scales, W. A. (2018). Survey of ionospheric Pc3-5 ULF wave signatures in SuperDARN high time resolution data. *Journal of Geophysical Research: Space Physics*, *123*(5), 4215–4231. https://doi.org/10.1029/2017JA025033

Skjæveland, Å. S., Carlson, H. C., & Moen, J. I. (2017). A statistical survey of heat input parameters into the cusp thermosphere. *Journal of Geophysical Research: Space Physics*, *122*(9), 9622–9651. https://doi.org/10.1002/2016JA023594

Strangeway, R. J. (2012). The equivalence of Joule dissipation and frictional heating in the collisional ionosphere. *Journal of Geophysical Research*, *117*(A2), 2011JA017302. https://doi.org/10.1029/2011JA017302

Takahashi, K., Yumoto, K., Claudepierre, S. G., Sanchez, E. R., Troshichev, O. A., & Janzhura, A. S. (2012). Dependence of the amplitude of Pc5-band magnetic field variations on the solar wind and solar activity. *Journal of Geophysical Research*, *117*(A4), 2011JA017120. https://doi.org/10.1029/2011JA017120

Thayer, J. P., & Semeter, J. (2004). The convergence of magnetospheric energy flux in the polar atmosphere. *Journal of Atmospheric and Solar-Terrestrial Physics*, *66*(10), 807–824. https://doi.org/10.1016/j.jastp.2004.01.035

Verkhoglyadova, O. P., Meng, X., Mannucci, A. J., & McGranaghan, R. M. (2018). Semianalytical estimation of energy deposition in the ionosphere by monochromatic Alfvén waves. *Journal of Geophysical Research: Space Physics*, *123*(6), 5210–5222. https://doi.org/10.1029/2017JA025097

Wang, B., Nishimura, Y., Hartinger, M., Sivadas, N., Lyons, L. L., Varney, R. H., & Angelopoulos, V. (2020). Ionospheric modulation by storm time Pc5 ULF pulsations and the structure detected by PFISR-THEMIS conjunction. *Geophysical Research Letters*, *47*(16), e2020GL089060. https://doi.org/10.1029/2020GL089060

Wright, A. N., Allan, W., & Damiano, P. A. (2003). Alfvén wave dissipation via electron energization: Electron acceleration in Alfven waves. *Geophysical Research Letters*, *30*(16), 1847. https://doi.org/10.1029/2003GL017605

Wright, D. M., & Yeoman, T. K. (1999). High-latitude HF Doppler observations of ULF waves: 2. Waves with small spatial scale sizes. *Annales Geophysicae*, *17*(7), 868–876. https://doi.org/10.1007/s00585-999-0868-9

Wright, D. M., Yeoman, T. K., Rae, I. J., Storey, J., Stockton-Chalk, A. B., Roeder, J. L., & Trattner, K. J. (2001). Ground-based and polar spacecraft observations of a giant (Pg) pulsation and its associated source mechanism. *Journal of Geophysical Research*, *106*(A6), 10837–10852. https://doi.org/10.1029/2001JA900022

Paper II

A Statistical Study of Optical Signatures of High-Latitude Pc5 waves

van Hazendonk, C. M., Baddeley, L., Laundal, K. M., Lorentzen, D. A.
Journal of Atmospheric and Solar-Terrestrial Physics, **274**, (2025)
doi: 10.1016/j.jastp.2025.106585

Journal of Atmospheric and Solar–Terrestrial Physics 274 (2025) 106585

Contents lists available at ScienceDirect

Journal of Atmospheric and Solar–Terrestrial Physics

journal homepage: www.elsevier.com/locate/jastp

Research paper

A statistical study of optical signatures of high-latitude Pc5 waves

C.M. van Hazendonk [a,b,*], L. Baddeley [a,c], K.M. Laundal [b], D.A. Lorentzen [a,c]

[a] Department of Arctic Geophysics, University Centre in Svalbard, Longyearbyen, Svalbard, Norway
[b] Department of Physics and Technology, University of Bergen, Bergen, Norway
[c] Department of Physics, University of Oslo, Oslo, Norway

ARTICLE INFO

Dataset link: https://kho.unis.no/Keograms/keograms.php, https://doi.org/10.11582/2025.B9FR665W, https://doi.org/10.5281/zenodo.14931122, https://omniweb.gsfc.nasa.gov/form/sc_merge_min1.html, https://space.fmi.fi/image/

Keywords:
ULF waves
Meridian scanning photometer
High-latitude
Svalbard
Equatorward propagation
Statistical study

ABSTRACT

We present the first large scale study of optical signatures associated with ultra-low frequency (ULF) waves using an automated detection method at high-latitudes in the northern hemisphere winter. We classify these waves as ULF wave driven auroral arcs (UAAs). We have detected 198 UAAs in optical keograms of the 630.0 nm channel of the Meridian Scanning Photometer (MSP) located in Longyearbyen, Svalbard. Some of the detected UAAs have accompanying signatures in the 557.7 nm channel. The 198 UAAs can be divided into different populations based on magnetic local time: dawn (129) and dusk (69), or propagation direction: poleward (126) and equatorward (72). The poleward-propagating population partly consists of field line resonance driven auroral arcs (FAAs), which have been extensively studied before and are generally well understood. In our case, solar wind data suggests that the FAAs are most likely externally generated through the Kelvin–Helmholtz instability on the flanks of the magnetopause. Furthermore, they exhibit a dawn-dusk asymmetry favoring the dawn flank as reported previously in literature. Another part of the poleward-propagating population seems to consist of internally generated small-scale waves. On the other hand, the equatorward-propagating population is less known with only three previous reports of optical signatures. The data suggest that they correspond to small-scale, internally generated, ULF waves, which potentially have an energy source formed by substorm-injected energetic particles. Possibly, the high-latitude position of Svalbard at the border between the auroral oval and the polar cap, explains why most known occurrences of equatorward-propagating waves have been observed around Svalbard.

1. Introduction

Ultra-low frequency (ULF) waves transfer and redistribute energy and momentum into the Earth's magnetosphere-ionosphere-thermosphere system. The ionosphere, due to its finite conductivity, can act as an energy sink to wave fields by causing plasma motion and creating currents. Wave energy in the form of Poynting flux is thus dissipated via current systems that are damped following Joule and frictional heating. Additionally, wave energy can accelerate electrons into the ionosphere, either through interaction with the parallel electric field associated with field line resonances (FLRs) as described by Rankin et al. (2021) or, for other types of wave modes, through various pitch angle scattering or magnetic mirroring effects (e.g. Liou and Sibeck, 2014; Rae et al., 2018). These accelerated electrons then dissipate their energy through ionization and collisional processes where the high energy population (≥100 eV), contributes significantly to the total energy flux and can be observed as ionization (Van Hazendonk et al., 2024) in the E- and F-region ionosphere. This ionization, along with the collisional processes, is visible as auroral arcs. ULF waves in the Pc5 frequency range (~1 mHz–7 mHz) are generally classified as having an energy source internal or external to the magnetosphere as well as being of either large azimuthal (low-m) or small azimuthal (high-m) scale size, ($m = 2\pi R_E L/\lambda_{az}$, where λ_{az} is the azimuthal wavelength at L-shell location, L, and R_E the Earth's radius). Low-m waves are often toroidally polarized, having their magnetic (electric) field oscillations confined in the azimuthal (radial) direction, while high-m waves are predominantly poloidally polarized showing opposite magnetic and electric field oscillation directions (Wright and Mann, 2006). In general, wave polarization is often mixed and waves can convert from one polarization into the other (Yeoman et al., 2010).

In the case of low-m waves, their generation mechanism often consists of coupling of externally generated fast, compressional mode waves to standing mode waves on magnetic field lines. Here, the field lines can be driven to resonance creating FLRs as described by for example the box model of Kivelson and Southwood (1986), Fenrich and Samson (1997) and Rankin et al. (2021). The energy source can include the Kelvin–Helmholtz instability (KHI) in which fast solar

* Corresponding author at: Department of Arctic Geophysics, University Centre in Svalbard, Longyearbyen, Svalbard, Norway.
E-mail address: charlottva@unis.no (C.M. van Hazendonk).

https://doi.org/10.1016/j.jastp.2025.106585
Received 22 March 2025; Received in revised form 30 May 2025; Accepted 22 June 2025
Available online 4 July 2025

wind speeds create flow shears on the flanks of the magnetopause which can then excite compressional mode waves that can couple to FLRs. Alternatively, solar wind pressure pulses can distort the dayside magnetopause, launching fast mode waves which propagate tailward, inside a waveguide, on the flanks (e.g. Mann et al., 1999). Conversely, high-m waves are thought to have a generation mechanism internal to the magnetosphere in the form of wave-particle interactions with drifting particle populations (Mager et al., 2009; Yeoman et al., 2010; Baddeley et al., 2005).

Many statistical studies on ULF wave characteristics involve ground magnetometer data (e.g. Baker et al., 2003; Pahud et al., 2009; Hynönen et al., 2020; Dimitrakoudis et al., 2022) and focus on large scale waves, FLRs. It has been well documented that, at high-latitudes, FLRs display a distinct signature whereby there is an amplitude maximum at the latitude of the resonant field line, accompanied by a 180° change of phase, ϕ, across the peak, with a poleward phase propagation (i.e. $d\phi/dlat < 0$) observed (e.g. Samson et al., 1992). Small-scale, high-m waves are prone to ionospheric attenuation and their signature is therefore not always visible in ground magnetometer data (Wright and Yeoman, 1999; Takahashi et al., 2013). Therefore, statistical studies (partly) investigating these types of waves rely on different instrumentation such as coherent scatter radars (e.g. SuperDARN) (James et al., 2013; Shi et al., 2018; Morita et al., 2024), HF Doppler sounders (Yeoman et al., 2000; Baddeley et al., 2005), TEC receivers (Zhai et al., 2021), or spacecraft (Takahashi et al., 1985; Anderson et al., 1990; Agapitov and Cheremnykh, 2011; Korotova and Sibeck, 2024, among others). For example, Kozyreva et al. (2022) specifically distinguish between ULF wave events with only an ionospheric signature, as observed with SuperDARN, only a ground signature in ground magnetometers, or whether they appear in both, thus using this qualification to provide more insight into wave properties and possible generation mechanisms. Radar studies of high-m waves report, in addition to poleward-propagating events, equatorward-propagating events at high-latitudes (e.g. Mager and Klimushkin, 2008; Mager et al., 2009; James et al., 2013; Michael et al., 2024). These waves also typically show phase changes exceeding 180° (Yeoman et al., 1992).

Samson et al. (2003) proposed a model in which (toroidal) FLRs, assumed to be driven by compressional, near-monochromatic fast waves, can produce auroral arcs (field line driven auroral arcs, FAAs). Auroral arcs are formed when electrons are accelerated downwards, into the ionosphere, by parallel electric fields. Shear Alfvén waves do not possess such a field according to ideal MHD. However, ideal MHD breaks down when the size of the perpendicular wavelength is similar to that of the electron inertial length or the ion gyroradius. Including kinetic effects shows that FLRs or shear Alfvén waves carry a parallel electric field component that supports the FACs (Lysak, 2023; Rankin et al., 2021). In the regions of upwards FACs, downward moving electrons are then accelerated and optical emissions are created. Typical energies involved in this process are less than a few keV (Rae et al., 2018). An extensive overview on auroral particle acceleration and kinetic Alfvén waves can be found in Lysak (2023). The link between FLRs, known for their ground based magnetic signature, and auroral arcs means that the optical signature of a FAA thus has a magnetic counterpart sufficient in magnitude to be observed by ground magnetometers. Rankin et al. (2021) discussed the various theoretical approaches (such as the two fluid MHD and kinetic theory) needed to generate a parallel E-field of sufficient magnitude to accelerate electrons up to the energies needed to create optical emissions in the 630.0 nm wavelength (< 1 keV (Kosch et al., 2001)). They note, however, that more observations are needed to extend the models in cases of time-dependent ionospheric energy dissipation rates, such as with FAAs, where ionospheric conductivities are modulated by the incoming particle precipitation. An alternative method whereby electrons can be driven into the ionosphere is related to standing poloidal mode ULF waves. The large magnetic field compressions from these ULF waves could be associated with periodic altitude changes in the mirror point, thus modulating the amount of electrons scattered into the loss cone (Liou and Sibeck, 2014). Similarly, compressional ULF waves were found to modulate the loss cone and thus enhance precipitation of electrons up to 100 keV (Rae et al., 2018) which would be sufficient to cause auroral emissions. However, current studies have only found these mechanisms prevalent at lower latitudes where the field lines have a more dipolar structure and map to the radiation belts.

Additionally, typical estimates regarding the amount of energy dissipated into the ionosphere by ULF waves have focused on equating the wave electromagnetic Poynting flux with ionospheric Joule heating (e.g. Hartinger et al., 2015; Rae et al., 2007) and ignoring this potential auroral counterpart. Recent work by Van Hazendonk et al. (2024), using an incoherent scatter radar, has shown that the energy flux related to particle precipitation can be 70% of the energy dissipation caused by Joule heating for ULF waves.

Gillies et al. (2018) performed a statistical study investigating FAAs using ground magnetometer data and redline (630.0 nm) auroral arcs in all-sky cameras. Using visual inspection, they identified 400 h (which represented 5% of the images that had some form of redline aurora emission in them) of FAAs with at least three consecutive wave periods visible in the keogram. Based on these 400 h, the first FAA statistical study based on optical data was performed. Similarly to the study by Baker et al. (2003), which used ground magnetometer data, both FLRs and FAAs were found to favor the dawn sector over the dusk sector and FAA wave activity was predominantly located in the predawn (around 4 MLT) and postdusk (around 20 MLT) sectors. More optical observations of ULF waves, exhibiting themselves as undulations or auroral arcs, are reported by Milan et al. (2001), Kozlovsky et al. (2006) and Rae et al. (2014) (557.7 nm), Samson et al. (1996), Milan et al. (1999), Mathews et al. (2004) and Baddeley et al. (2017) (557.7 and 630.0 nm), and Motoba et al. (2021) (630.0, 670.0 nm and white light) among others. Recently, Yin et al. (2023) managed to record periodic (1.67–3 mHz), poleward moving, FAAs in the postdawn sectors utilizing all-sky imagers at 630.0, 557.7, and 427.8 nm from Ny-Ålesund, Svalbard. The arc signature in all three wavelengths indicates a wide energy range associated with the periodic arcs. Interestingly, all of these studies mentioned above, except three case studies by Baddeley et al. (2017) and Rae et al. (2014) and Mathews et al. (2004) show a poleward propagation of the arcs, consistent with the FAA theory originally proposed by Samson et al. (2003).

Given the paucity of observations showing ULF wave driven auroral arcs (UAAs) with equatorward propagation it is unclear if these are a separate class of FAAs or if FAAs are a general sub-class of UAAs (where the propagation is always poleward). The three case studies of UAAs with equatorward propagation mentioned previously (Baddeley et al., 2017; Rae et al., 2014; Mathews et al., 2004) discussed generation mechanisms associated with a coupling of sunward propagating fast mode waves in the tail, or unstable drifting particle populations.

As discussed earlier in the Introduction, the characteristics (such as propagation direction, dominant frequency and MLT location) of various ULF wave populations are linked to the proposed different generation mechanisms (e.g. FLRs with an external generation mechanism statistically have a poleward phase propagation and can be linked solar wind speeds exceeding 500 km/s Engebretson et al., 1998), and geomagnetic conditions (e.g. storm-time Pc5 waves dominate in the dusk sector due to dusk ward propagation after particle injection on the night side Anderson et al., 1990; Wang et al., 2020). By establishing a database of optical observations of parameters with suitable MLT coverage, it is possible to observe statistically if the same trends are apparent where there is an extra requirement of optical emissions. Beyond the commonly studied poleward-propagating FAAs, this study will investigate optical signatures of periodic arcs with an equatorward propagation and aim to expand the existing database of UAAs. Two of the three case studies of equatorward-propagating arcs have been observed using the Meridian Scanning Photometer (MSP) in Longyearbyen, Svalbard (78.15°N geographic latitude (glat); 75.12°N magnetic

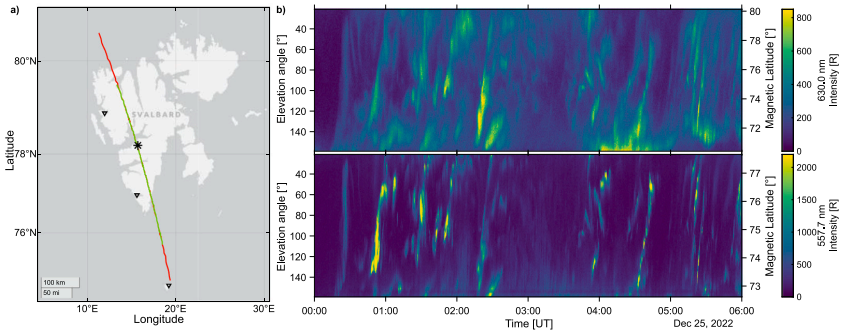

Fig. 1. Panel (a) shows the location of the KHO with a black star and the field-of-view of the 557.7 nm (green) and 630.0 nm (red) channel plotted in geographical coordinates. The black nabla symbols give the locations of magnetometer stations in Ny-Ålesund, Hornsund and Bjørnøya. An example of 6 h of MSP data is shown in panel (b), where the top panel shows the 630.0 nm channel and the bottom panel the 557.7 nm channel. The left *y*-axis gives the elevation angle, while the right *y*-axis gives the magnetic latitude. The intensity is given in Rayleigh. (For interpretation of the references to color in this figure legend, the reader is referred to the web version of this article.)

latitude (mlat)) (Mathews et al., 2004; Baddeley et al., 2017). The MSP's long time series, multiple wavelength channels, and keogram format make it well-suited for statistical ULF wave studies. The keogram format also enables methods for automatic detection, such as the technique developed by Van Hazendonk et al. (2024) which has been successfully applied to incoherent scatter radar data. Automatic detection drastically reduces the time needed to create such a ULF wave database and removes human bias associated with visual identification techniques. In addition to the 630.0 nm emissions investigated by Gillies et al. (2018), the 557.7 nm MSP channel could give additional insights in the energy involved in the various ULF wave events. In this way, multiple wavelengths can be explored to study the effects of auroral arcs with broader energetic signatures. In the next section we discuss the data sources and their characteristics. In Section 3, we describe the ULF wave detection method and event selection in detail. The results are visualized in Section 4 and discussed in Section 5 including limitations and potential generation mechanisms. Section 6 concludes the paper.

2. Data

The MSP is located at the Kjell Henriksen Observatory (KHO) (Herlingshaw et al., 2025) near Longyearbyen, Svalbard (78.15°N glat; 75.12°N mlat). The observatory is marked with a black star in Fig. 1a. The MSP records auroral intensities using a rotating mirror to scan the magnetic meridian from north to south. The scan angle is used to determine the elevation angle for each data point along the meridian. The light reflected from the mirror is input into up to six channels to record several auroral emission intensities simultaneously. Each channel comprises an interference filter, a filter tilting mechanism, and a photomultiplying tube inside a cooling unit. The tilt mechanism is used to adjust the tilt angle between the incident light and the filter: this is used both for fine-tuning the filter angle to auroral emission lines and recording background light intensities for background substraction. In this study, keograms from the 557.7 nm and 630.0 nm channels will be used. An example of the dawn sector (00:00–06:00 UT) for both wavelengths is shown in Fig. 1b, where the elevation angle is plotted on the left *y*-axis.

The instrument has been located at KHO since 2007, thus providing 17 seasons of data, from 2007/2008–2023/2024, where each season lasts from the beginning of November to the end of February. To ensure sufficient darkness, the instrument only operates when the sun is at least 10° below the horizon. Please note that seasons 2010–2011 and 2014–2015 only contain data from mid-January–late February due to instrument maintenance. The maintenance and updates over the 17 seasons include new photomultiplier tubes, coolers, electronics, filters, a new mirror, and an increased temporal resolution from 16 to 8 s. The absolute calibration of the instrument is carried out using a built-in low-level light source. The interference filters are not inside temperature-controlled enclosures, and changes in room temperature can shift the center wavelength of the filter passband. A "tilt angle" calibration is regularly carried out to counteract the effects of temperature changes. A quality check is performed to the data to ensure that a correct calibration has been applied to the data.

Since the MSP requires clear skies to make accurate observations, statistics on local cloud cover are used. To get information on cloud cover, we use a cloud detector (Aurora Cloud Sensor III from Aurora Eurotech) from the University College in London that has been in operation at KHO from mid-January 2016 onward (Aruliah and McWhirter, 2025). This instrument has a temporal resolution of 1 min and a field-of-view (FOV) of 90° centered 20° south-east of zenith, thus covering the region with the majority of ULF wave activity. The clarity is recorded as the difference between the air temperature, T_{air}, and the sky temperature, T_{sky}, resulting in Clarity = $T_{\text{air}} - T_{\text{sky}}$. A clarity value greater than 56 corresponds to a clear sky during winter months (November–February) (Marocco, 2024).

We obtain solar wind data shifted to the bow shock nose through OMNIWeb. The data have a 1 min temporal resolution and consist of a combination of ACE, DSCOVR (NOAA Space Weather Prediction Center, 2016), and WIND spacecraft from 2007–2024. Additionally, we use the SuperMAG (Gjerloev, 2012) electrojet index (SME) (Newell and Gjerloev, 2011), which provides a generalization of the auroral electrojet indices based on data of over 100 magnetometers, to give information about the geomagnetic conditions. This index also includes magnetometer stations on Svalbard to determine its value. To verify ULF wave occurrence, we use magnetometer data with 10 s resolution. This data is obtained via the International Monitor for Auroral Geomagnetic Effects (IMAGE) magnetometer network.

3. Methods

The detection method of UAAs is based on the 2D FFT method described by Van Hazendonk et al. (2024). Instead of incoherent scatter radar data, keograms of the MSP are used. To make this data suitable for the 2D FFT method, several processing steps are applied. First, the elevation angle of the MSP observation is converted into mlat, by assuming a fixed emission altitude or mapping height for each wavelength. In case of 630 nm (557.7 nm) the emission height is assumed at 250 km (120 km) altitude (Partamies et al., 2022), resulting in a FOV of 72°–78° mlat (73°–77° mlat). The corresponding meridians are shown in Fig. 1a, and the MSP spectra in Fig. 1b display the mlat values on the right y-axis. Secondly, linear interpolation is applied to

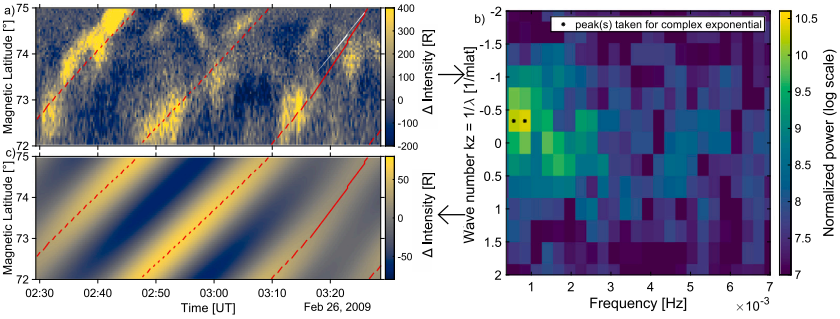

Fig. 2. Reconstruction of the ULF wave for a window between 02:30–03:30 UT and 72°–75° mlat on February 26, 2009 in a keogram of the MSP. Panel (a) shows the relevant window of the median filtered MSP 630.0 nm keogram, (b) the positive part of power spectrum from the 2D FFT in which the peaks used for reconstructed are highlighted with asterisks, and (c) the real part of the reconstructed complex wave using Equation 7 in Van Hazendonk et al. (2024) with reconstructed wavefronts overlaid in red. (For interpretation of the references to color in this figure legend, the reader is referred to the web version of this article.)

get a fixed magnetic latitude spacing of 0.05° mlat. A high-pass filter is applied to the data by subtracting the median value of a 20 min by 20 km moving window. The frequency cutoff of this filter is 0.37 mHz. Now the MSP data has been prepared for the 2D FFT procedure. The MSP temporal resolution of 16 s (8 s from the start of the 2016/2017 season onward) results in Nyquist frequencies of 31.25 and 62.5 mHz, respectively.

To avoid false positives, the whole 2D FFT procedure is performed with four different window sizes, after which an event is only identified if it occurs in at least three out of four of the analyses. Rectangular windows with window lengths of respectively 30 min and 1 h in the time direction, and 2° and 3° (1° and 2°) for the 630.0 nm (557.7 nm) channel in the mlat direction are used, giving us a number of four analyses in total. In both the time and the mlat direction, the window overlap is given by half of the window length. An example of a 1 h by 3° mlat window for the 630.0 nm channel is shown in Fig. 2a. The 1 h (30 min) window size corresponds to a frequency resolution of 0.28 mHz (0.56 mHz).

Using the 2D FFT, a relative power spectrum, determined by taking the 10 logarithm (log10) of the power spectrum divided by its own median, is calculated for each window. An example of such a power spectrum is shown in Fig. 2b. Here, only positive frequencies above the highest cutoff frequency, 0.37 mHz in this case, are shown. Of this power spectrum, up to four power peaks are selected. The frequency, phase, wave number, and amplitude information of the selected peaks is then used to reconstruct the ULF wave part of the spectrum using Equation 7 in Van Hazendonk et al. (2024). This results in the reconstructed example as shown in Fig. 2c where the detected wave fronts are plotted on top in red.

As outlined in Van Hazendonk et al. (2024), spectral peaks must be distinguished from background signals at a statistically significant level above any background noise. Therefore, 2 h of subsequent single power spectra are stacked on top of each other to form an averaged power spectrum of which, again, up to four power peaks are selected. Only peaks which occur in both the single power spectra and the averaged one can be selected. The stacked power spectra also ensure that the peaks in subsequent spectra occur at similar frequencies as is expected for ULF wave events, thus only detecting events that meet this requirement. More detailed information about this selection procedure can be found in Section 4.1 of Van Hazendonk et al. (2024). Peaks are only detected if they are above a certain detection threshold of the maximum power peak for an event. Due to upgrades to the MSP instrument over the years, the exact efficiency varies slightly over the optical seasons. To account for the changes in efficiency, the threshold has been defined per season. For a single MSP file (generally 1 file per 24 h), the maximum relative peak of the relative averaged power spectrum is recorded for each averaged power spectrum. A maximum value of this is recorded for each day. For the entire optical season, 96% of the median value of these daily power peaks is taken as the detection threshold for the season. Detected peaks have to be above this threshold.

Since UAAs and FAAs have a latitudinal propagation, instances in which the wave number is only equal to zero (usually attributed to spreading of aurora throughout the entire FOV due to the presence of clouds) are removed. Additionally, windows that have a combination of positive and negative wave number values are removed. Since it is expected that the arcs move either poleward (corresponding to a negative wave number) or equatorward (corresponding to a positive wave number), they should thus have one slant direction in the keogram. This directionality of the arcs also allows the removal of events that are made up out of windows with different slant directions. An additional control is performed to check that the detection is coherent across the different window sizes and that consistent wave front reconstruction is visible.

After detection in the individual power spectra, an event is found if there are at least two (three) consecutive windows with detection in case of a 1 h (30 min) window. The same event will continue in case of a one window gap.

At high-latitudes, especially in the cusp region (inside the FOV of the MSP during daytime, 09–15 MLT; 06–12 UT), the 630.0 nm channel shows various signatures, such as poleward moving auroral forms (PMAFs) and irregular pulsations at cusp latitudes (IPCL). Similarly, on the night side (21–03 MLT) phenomena such as auroral streamers, which are defined as north-south aligned arcs near the poleward auroral oval boundary (Gallardo-Lacourt et al., 2014), might contaminate UAA detection. To avoid false positives from phenomena with similar optical signatures, we chose to focus on the dawn (03–09 MLT; 00–06 universal time (UT)) and dusk (15–21 MLT; 12–18 UT) sectors.

Our detection method gives us information about the UAAs such as frequency, f [Hz], and meridional wave number, k_z [1/mlat]. We can use the frequency and wave number information to calculate the velocity, v, of the waves, where $v = \frac{2\pi f}{k_z}$ [mlat/s]. This can then be transformed into m/s. A negative (positive) wave number corresponds to poleward (equatorward) propagation. To get east- or westward propagation of the arc, information beyond the north-south meridian provided by the MSP is needed, such as from all-sky cameras/imagers. This is thus beyond the scope of the paper.

To determine which of our detected UAA events show FAA characteristics, we use data from four ground magnetometer stations to check the amplitude and phase of any associated magnetic signatures, which is discussed in more detail in Section 5. The stations used are Bjørnøya (BJN), Hornsund (HOR), Longyearbyen (LYR), and Ny-Ålesund (NAL)

Table 1
Total MSP data available and detected UAA events for the 630.0 nm channel (October 2007–March 2024). The events are then divided into poleward- and equatorward-propagating.

	MSP data [h]	Detection [h] (number of events)	Poleward [h] (number of events)	Equatorward [h] (number of events)
Dawn	8148	239.5 (129)	178.5 (93)	61 (36)
Dusk	5609	148.5 (69)	68.5 (33)	80 (36)

Table 2
The amount of MSP data (in hours) available in both the dawn and the dusk sector from 13 January 2016 onward when the cloud detector is providing data, and which part of this corresponds to clear skies. The detection percentage of UAAs is calculated using the total number of hours with clear skies. The UAA events are then divided into poleward- and equatorward-propagating.

	MSP data [h]	Clear sky [h] (%)	Detection [h] (%)	Poleward [h] (%)	Equatorward [h] (%)
Dawn	4510	1220 (27.0%)	78 (6.4%)	63 (5.2%)	15 (1.2%)
Dusk	3187	823 (25.8%)	73 (8.9%)	37 (4.5%)	36 (4.4%)

located at a geographical latitude of 74.5°, 77.0°, 78.2°, and 78.9° respectively as shown in Fig. 1a.

Note that the radiative lifetime of the O(^{1}D) 630.0 nm emission lasts for around 110 s (Witasse et al., 1999). Due to this long lifetime, only UAA wave periods significantly exceeding 110 s, corresponding to well below 9.1 mHz, can be distinguished in the 630.0 nm keograms.

Table 3
The total number of ULF wave events detected in the 630.0 nm channel and the number of these events that show accompanying detection in 557.7 nm.

	Events in 630.0 nm (poleward/equatorward)	Detection in 557.7 nm (poleward/equatorward)
Dawn	129 (93/36)	21 (11/10)
Dusk	69 (33/36)	12 (7/5)

4. Results

Table 1 shows the total available hours of the 630.0 nm MSP channel. Note that this includes periods with cloud cover, and the algorithm requires clear skies. Table 1 also shows the hours of UAA detection and the number of events, using a 1 h by 3° mlat detection window, split by propagation direction (poleward and equatorward).

Fig. 3 illustrates the average frequency [Hz] (panel a), wave number [1/mlat] (panel b), duration [h] (panel c), and velocity [m/s] (panel d) of the UAA events listed in Table 1 for dawn (blue; solid line) and dusk (red; dashed line). Although not depicted, the results show very similar behavior for the analyses with other detection window sizes. The mean frequencies peak around 1 mHz, corresponding to the lower end of the Pc5 spectrum. The wave numbers indicate that there is an equal number of poleward- and equatorward-propagating events during dusk, while poleward propagation is dominant on the dawn flank. Based on the wave number, we can calculate velocities along the meridian. Both flanks show velocities similar to or slightly exceeding typical ionospheric convection velocities. Event duration is dominant between 1.5–2.5 h, with some more prolonged events.

Fig. 4 shows the UAA occurrence probability as a function of MLT categorized by propagation direction. The poleward-propagating population displays a dawn-dusk asymmetry.

Table 2 shows the number of MSP hours available from 13 January 2016 onward for which the cloud detector was operating. Table 2 also includes the number of hours as well as percentages with clear sky and UAA detection. The sky is clear for slightly more than 25% of the time. The detection percentage is based on the total number of hours with clear skies. For comparison, Gillies et al. (2018) found redline, FAAs occurrence around 5% of the time for which some kind of redline aurora emission was present. This value is hard to compare to our detection percentages listed in Table 2 as our percentages include all types of UAAs and are based on clear skies, while Gillies et al. (2018) based their percentages on the occurrence of any type of redline aurora. Nevertheless, we see that our values are higher, indicating that there might be other wave modes present in our data in addition to FAAs. This will be explored further in Section 5.

Out of 129 (69) events detected in dawn (dusk) in the 630.0 nm channel, 21 (12) events show accompanying detection in 557.7 nm. In order to match, the start and ending times of an event have to be within an hour for the different wavelengths and the mlat regions need to overlap. Table 3 summarizes these numbers and divides them into poleward- and equatorward-propagating events. An example of an equatorward-propagating event during dusk on 10 December 2013 is shown in Fig. 5. The detected wave fronts are overlaid in red and the detection area is outlined in black.

To get more insight into correlations with solar wind parameters, which could point towards possible external generation mechanisms, we look into mean solar wind conditions for each UAA event. The IMF clock angle, $\theta = \arctan2(B_y, B_z)$, is plotted in Fig. 6 for poleward (panel a) and equatorward (panel b) propagation. The occurrence has been divided by the IMF clock angle distribution from November–February during all MSP seasons. A value of one, as indicated by the black dashed line, corresponds to an average occurrence of that clock angle, while a value exceeding one indicates that it is more likely to get a UAA event during this condition. It can be seen that UAA activity is slightly more likely for IMF B_y dominated periods. More specifically for poleward propagation, B_y is predominantly positive at the dawn flank and negative at the dusk flank. Equatorward propagation indicates a weaker, but opposite tendency, with negative B_y at dawn and a slight positive B_y at dusk. In addition, B_z seems to be negative more often at dawn than dusk for equatorward propagation.

There is no correlation between UAA activity and solar wind dynamic pressure in this study. We do, however, see slightly faster solar wind speeds at dawn and dusk for poleward propagation (Fig. 7a), but not for equatorward propagation (Fig. 7c). In addition, the SME index shows that UAA events mainly occur during quiet conditions for both poleward (Fig. 7b) and equatorward (Fig. 7d) propagation.

5. Discussion

Applying a newly developed detection algorithm to data from the MSP in Longyearbyen, we have identified 198 UAA events. All these events take place during northern hemisphere winter (Nov–Feb). An automated detection method makes it easier to handle large time series of data. In this case, it enables us to investigate all optical seasons of the MSP located at KHO. A disadvantage is that the method most likely misses some of the occurrences, because of an inadequate detection threshold. In addition, as the tilt angle calibration of the MSP has to be performed manually, the instrument is not always calibrated correctly, thus lowering the number of available hours. Therefore, we expect our detection values to be a minimum. This is especially the case for detection in the 557.7 nm channel, because the arc signatures have a

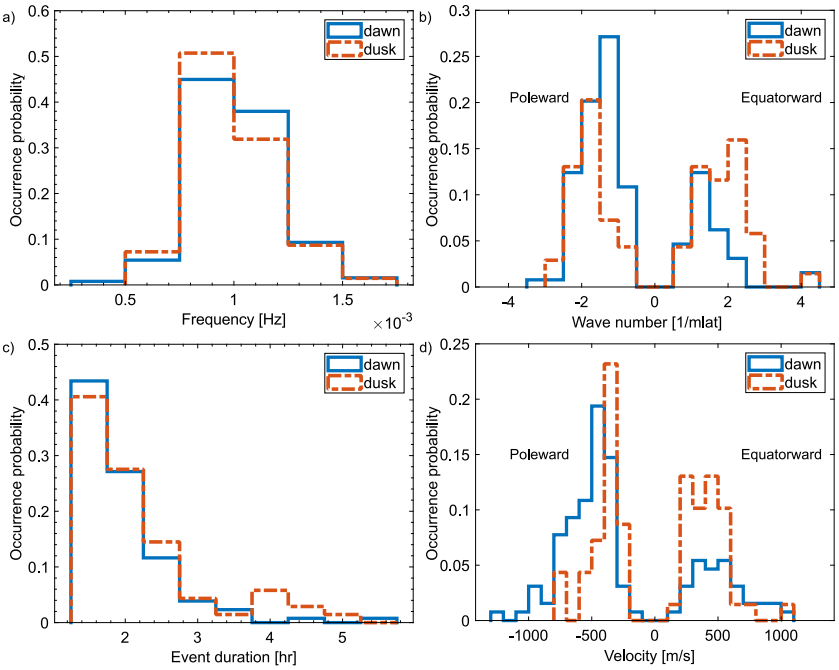

Fig. 3. Occurrence probability of the average frequency [Hz] (panel a), wave number [1/mlat] (panel b), duration [h] (panel c), and velocity [m/s] (panel d) per ULF wave event for dawn (blue; solid line) and dusk (red; dashed line) for the 630.0 nm channel. The total number of events is 129 for dawn and 69 for dusk. The normalization is applied per category (e.g. the total occurrence probability for dawn is 1 and the same goes for dusk).

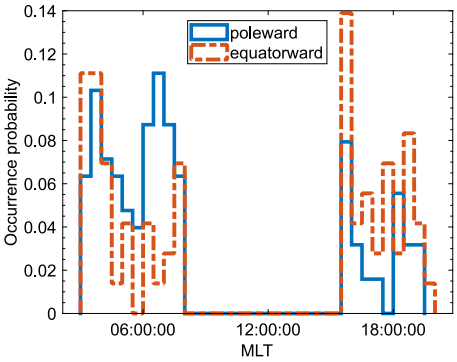

Fig. 4. The number of ULF wave events as a function of magnetic local time (MLT) at the start time of the events for poleward (blue; solid line) and equatorward (red; dashed line) propagating waves. The total number of poleward-propagating events equals 126 (93 in dawn and 33 in dusk) versus 72 equatorward-propagating events (36 in both dawn and dusk). The normalization is applied per category (e.g. the total occurrence probability for poleward-propagating is 1 and the same goes for equatorward-propagating).

smaller latitudinal extent due to the lower emission altitude. Therefore, the detection method is less efficient for this channel. However, we showed the existence of a subset of ULF waves that occurs in both channels, thus indicating higher kinetic energy deposition for this group.

Our 198 UAAs are divided over dawn (129 events) and dusk (69 events), thus showing a clear dawn-dusk asymmetry. The dominant wave frequency is around 1 mHz as depicted in Fig. 3a. This falls within the range of previous case studies around Svalbard, such as Mathews et al. (2004) (1.7 mHz), Baddeley et al. (2017) (1.63 mHz), Yeoman et al. (2008) (3.3 mHz), and Michael et al. (2024) (0.75 mHz). The SME index, as shown in Fig. 7b and d, indicates predominantly quiet geomagnetic conditions during the events. A possible explanation for the quiet geomagnetic conditions is the high-latitude location of Svalbard in relation to the auroral oval. In case of high geomagnetic activity, Svalbard is often located in the polar cap because of the general equatorward expansion of the auroral oval. Since standing wave structures such as FLRs are located on closed field lines, we do not expect to observe them within the polar cap. The fact that we are observing signatures in optical emissions also adds weight to the fact that we are inside the auroral oval region thus on closed field lines capable of maintaining a standing wave structure. A statistical study by Shi et al. (2018) utilizing SuperDARN data in the northern hemisphere confirmed, in line with our results, that low frequency Pc5 waves are dominant at high-latitudes during geomagnetically quiet period. The most probable frequency in their Pc5 range (1.7–6.7 mHz) was found to be 2.1 mHz, and the dominant frequency decreased as a function of increasing latitude. The low frequencies are typical at these latitudes and MLTs, due to field line stretching towards the magnetotail (Samson et al., 2003; Baddeley et al., 2017). Shi et al. (2018) showed a preference for events during the winter season (Nov–Feb) on the dusk flank, in comparison to our preference for dawn flank. They noted, however, that there was a distinct lack of radar back scatter on the dawn flank making a dawn-dusk asymmetry comparison difficult.

Most of our events have a short duration (1.5–2.5 h), as shown in Fig. 3c, which fits well with previous reports for UAAs, FAAs and ULF waves without optical signatures such as Mathews et al. (2004), Baddeley et al. (2017), Gillies et al. (2018) and Michael et al. (2024).

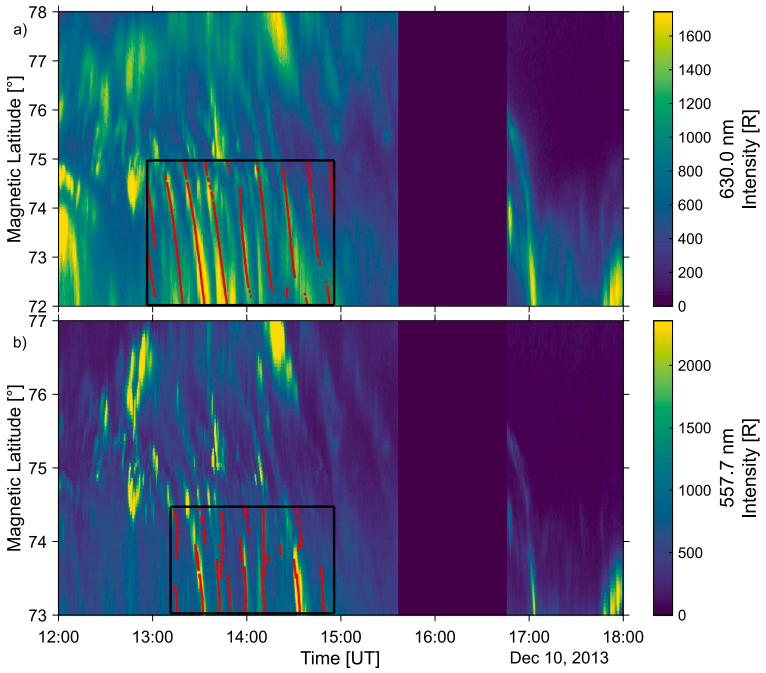

Fig. 5. UAA detection in both 630.0 nm (panel a) and 557.7 nm (panel b) on 10 December 2013. The detected wave fronts are overlaid in red on the MSP data, and the detection area is outlined in black. For detection in 630.0 nm (557.7 nm), a 1-h x 3° mlat (30 min x 1° mlat) window was used. (For interpretation of the references to color in this figure legend, the reader is referred to the web version of this article.)

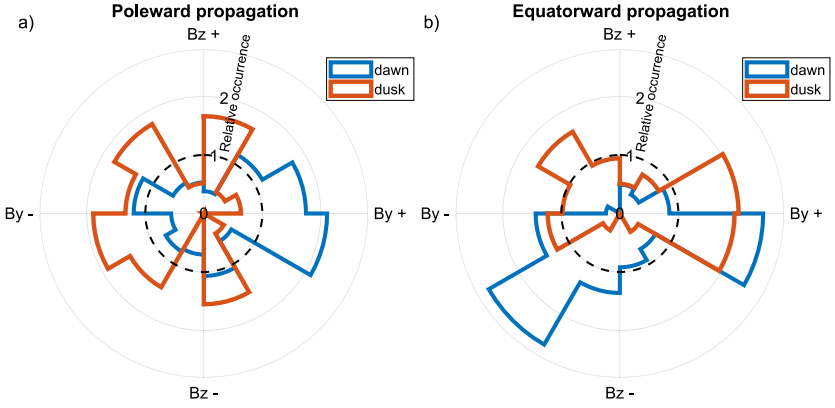

Fig. 6. A histogram of the IMF clock angle, $\theta = \arctan2(B_y, B_z)$, for poleward (panel a) and equatorward (panel b) propagating ULF waves. The horizontal axis shows the B_y direction, and the vertical axis the B_z direction. The radial axis gives the relative occurrence, which is calculated by dividing the occurrence probability during ULF wave events by the general occurrence probability of the solar wind. A relative occurrence of one is indicated by the black dashed line.

A minority of our events show extended durations. The velocities recorded in this study (Fig. 3d) represent line-of-sight values along the magnetic meridian and range up to just over 1000 m/s, the majority being between 300–600 m/s. Previous optical reports of equatorward phase propagation velocities in the MSP data are given by Baddeley et al. (2017), 460 m/s, and Mathews et al. (2004), 2.2 km/s, where Mathews et al. (2004) notes that this is a factor 10 higher than the convection velocity. Additionally, Yeoman et al. (2008) reported an equatorward phase propagation of 400 m/s above Svalbard in the dusk sector using SuperDARN radars. Poleward arc propagation velocities above Svalbard are reported by Yin et al. (2023), about 570–1000 m/s, and Kozlovsky et al. (2006), 490±110 m/s, which exceeds the measured convection velocity of about 200 m/s. Our velocities thus fall into the velocity ranges previously reported for UAAs above Svalbard, though being lower than the value reported by Mathews et al. (2004).

Within our established database of 198 events, we have classified two separate populations based on the movement of the arc structures, poleward versus equatorward. To check whether our events can be

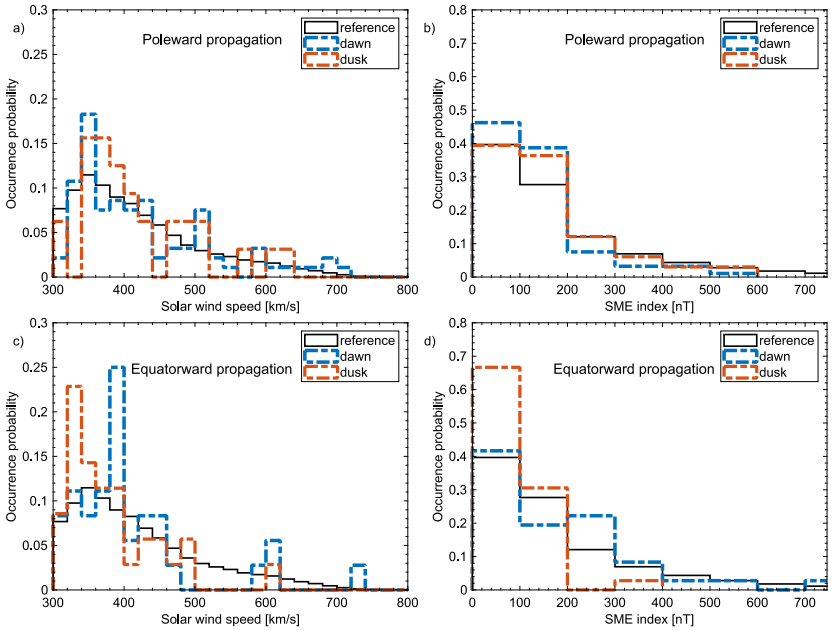

Fig. 7. A histogram showing the occurrence probability of the solar wind speed for poleward (panel a) and equatorward (panel c) wave propagation as well as the SuperMAG SME index for poleward (panel b) and equatorward (panel d) propagation. Each histogram shows the reference data, which lists all occurrences between 2007–2024, with a black solid line, while the occurrence probability for mean value per ULF wave event is shown in dashed lines, using blue for dawn and red for dusk.

classified as FAAs, we performed an FFT of ground magnetometer data to obtain the frequency, amplitude and phase for the duration of each UAA events, after filtering the magnetometer data by subtracting a 30 min median value. Using these three parameters we determine if an optical signature has a matching magnetometer signature consistent with a FLR. A distinct spectral peak in the power spectrum around the same frequency detected in the MSP data is needed and the dynamic FFT should be consistent and frequency stable over the duration of the event. The dominance of the toroidal mode polarization in FLRs, coupled with their large scale (low-m) size means that FAAs have a distinct conjugate ground magnetometer signature in the B_x component. Typically, the magnitude of the FLRs are 10s of nT, peak-to-peak (Baker et al., 2003). For a match, the peak-to-peak modulation must be at least 10 nT. Lastly, we expect the cross-phase analysis to show a power peak around the UAA frequency which has evidence of a phase change of around 180°. An example of a matching event is shown in the left column of Fig. 8 (panels a, c, e, g, and i showing the MSP keogram, magnetometer time series, FFT, dynamic FFT and cross phase analysis, respectively). An event without a match (only an optical signature) is shown on the right in Fig. 8 panels b, d, f, h, and j. In panel (f) it can be seen that the magnetometer data has a peak at a lower frequency than the MSP data. Additionally, most magnetometer power seems to be located around BJN and HOR rather than below the detected signature in the MSP, this then results in low power throughout the dynamic FFT (panel h) and an incoherent cross-phase analysis (panel j).

To investigate possible underlying energy sources responsible for driving the waves behind both the poleward- and equatorward-propagating populations, we consider each category separately.

5.1. Poleward-propagating population

Interestingly, the dawn-dusk asymmetry is only present in the 126 poleward-propagating events (93 in dawn; 33 in dusk) and not in the 72 events with equatorward propagation. Previously, Gillies et al. (2018) reported a dawn-dusk asymmetry for FAAs. Poleward-propagating UAAs in our study show a similar asymmetry with both the FAAs observed by Gillies et al. (2018) and the FLRs observed by Baker et al. (2003), with the majority of these also occurring in the dawn sector. The poleward category also shows a distribution of coinciding solar wind speeds with a distinct tail extending up to faster speed, (Fig. 7a). 23% (16%) of dawn (dusk) events occur during speeds > 500 km/s, which is consistent with an increased possibility of external generation via the KHI (Engebretson et al., 1998). The solar wind dynamic pressure (not shown) does not show large pressure pulses associated with the UAAs, which suggests that the waveguide mode proposed by Mann et al. (1999) is not a driving factor here. As stated earlier, poleward-propagating optical events have been identified as FAAs (e.g. Milan et al., 2001; Kozlovsky et al., 2006; Yin et al., 2023). The dawn-dusk asymmetry is a further indication that the poleward-propagating waves are occurring on closed field lines (Kwon et al., 2019).

The magnetometer check shows that only 12% of the poleward-propagating events exhibit a clear matching signature in the ground magnetometer data, while another 15% shows a partial match. The lack of consistent matching ground-magnetometer data indicates that there is a population of smaller-scale waves with higher m numbers in the poleward-propagating class making them a distinct phenomena from the traditional FAAs. This is supported by the fact that over half of the poleward-propagating events occur during low solar wind speeds, along with no evidence of dynamic pressure pulses indicating a smaller probability for an external generation mechanism needed for large-scale waves such as the KHI (Kavosi and Raeder, 2015; Engebretson et al., 1998). It is thus likely that part of the poleward-propagating UAAs have an energy source internal to the magnetosphere through either interactions with drifting energetic particle populations or coupling with fast mode wave which propagate sunward from the magnetotail. James et al. (2013) noted that substorm-injected particles

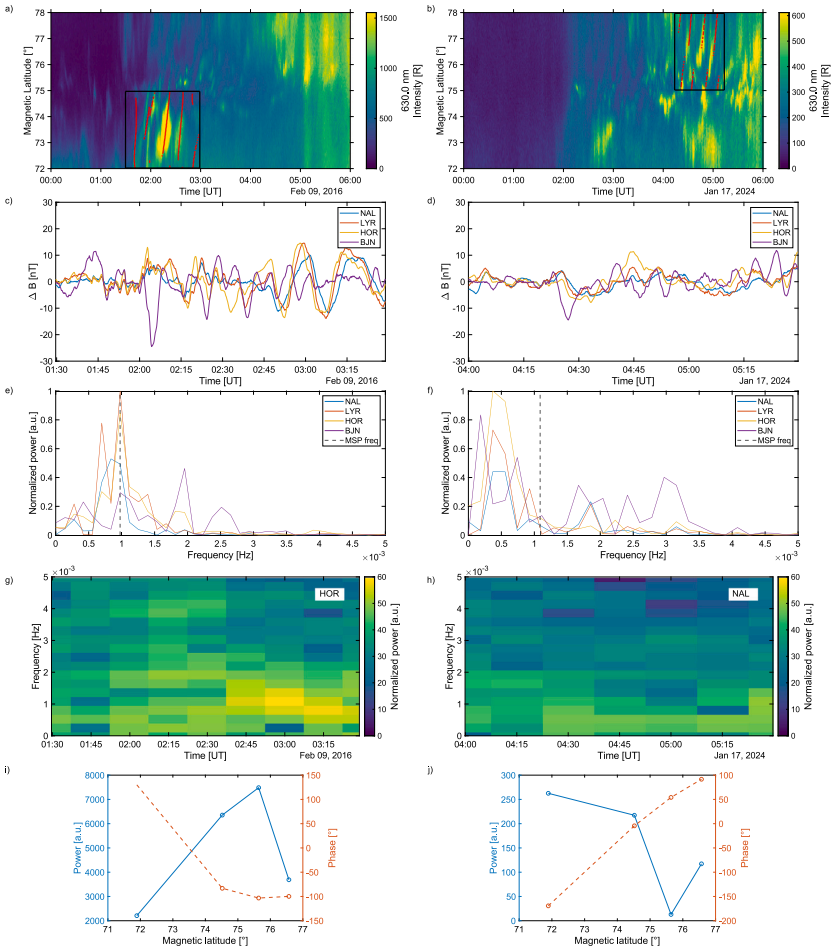

Fig. 8. Examples of the magnetometer check, in which the left column shows matching signatures across MSP and magnetometer data on 9 February 2016, while the right column provides no match for 17 January 2024. Panels (a) and (b) show the 630.0 nm channel of the MSP. Panels (c) and (d) the filtered B_x component of the ground magnetometer located in Ny-Ålesund (NAL), Longyearbyen (LYR), Horsund (HOR), and Bjørnøya (BJN) for the detection period, and a black dashed vertical line at the UAA frequency detected using MSP data. Panels (e) and (f) show the power spectrum of panels (c) and (d), respectively. Panels (g) and (h) depict a dynamic FFT at the mlat (HOR and NAL, respectively) at which the activity in the MSP keogram takes place, and panels i and j show cross-phase analysis at the MSP UAA frequency as shown in panels (c) and (d). (For interpretation of the references to color in this figure legend, the reader is referred to the web version of this article.)

can provide an energetic particle populations within the Earth's magnetosphere that are capable to sustain poloidally polarized, small-scale ULF waves. Most of these ULF waves showed equatorward propagation, but, depending on the latitudinal separation between the substorm and the ULF wave event, a fragment of these small-scale waves can exhibit poleward propagation. The presence of some smaller scale poleward-propagating UAAs could also explain our slightly higher detection rates compared to Gillies et al. (2018).

5.2. Equatorward-propagating population

The equatorward-propagating population is less known and, to our knowledge, there are only three reports of UAAs with equatorward propagation (Mathews et al., 2004; Baddeley et al., 2017; Rae et al., 2014) of which the first two are both recorded on Svalbard during dusk with frequencies around 1.6–1.7 mHz, making them similar to our observations. The study by Rae et al. (2014) might be caused by different processes as it takes place at lower latitudes, during midnight, and at higher frequencies. The equatorward phase propagation of ULF waves has previously been linked to poloidal wave polarization (Yeoman et al., 2010, 1992), due to the lack a 180° phase change as expected for toroidal polarized waves. Similarly to toroidally polarized waves, poloidal ones can be observed as standing Alfvén waves between conjugate points in the Earth's ionosphere (James et al., 2013). As mentioned previously, the small azimuthal scale (high-m number) of these waves coupled with ionospheric attenuation effects makes it difficult to observe them in ground magnetometers (Wright and Yeoman, 1999). For a typical E-region altitude of 100 km, ground magnetometers cannot observe waves where $|m| \geq 20$ (e.g. Pilipenko et al., 2012). Therefore, radars have been predominantly used to study this population (Shi et al., 2018; Mager et al., 2009; Yeoman et al., 2008, 2010; Michael et al., 2024). The lack of indications suggesting external generation mechanisms, such as increased solar wind speeds

or dynamic pressure pulses, in our study further supports our summarization that the equatorward-propagating population mainly consists of small-scale, poloidal waves. This is further stressed by the fact that the ground magnetometer check only finds 3% (12.5%) of the events with equatorward propagation to (partial) match across MSP and magnetometer data.

In addition to the poleward or equatorward propagation, ULF waves (and by extension UAAs and FAAs) also propagate eastward or westward around the magnetosphere. The sign of the m number signifies either eastward or westward propagation. Since the MSP is scanning along the geomagnetic meridian, we do not have azimuthally spaced data and it is thus not possible to determine the azimuthal wavelength of the UAAs. It is therefore not possible to calculate the m number magnitude (other than to say they are large scale or small-scale using ground magnetometer data) nor the polarity. Regardless, there are mechanisms which can drive small-scale ULF waves and thus UAAs internal to the magnetosphere. Work by Mager and Klimushkin (2008) and Mager et al. (2009) together with the optical case studies around Svalbard, suggest that the UAAs might correspond to westward propagating small-scale ULF waves excited through a drift resonance mechanism utilizing the westward drifting substorm injected protons. Later on, James et al. (2013) found that eastward propagating electrons injected into the magnetosphere during substorm activity in the tail could provide an additional particle population for wave excitation. The frequency of the waves studied by James et al. (2013) is comparable to our study, ranging between 0.3–5 mHz with dominant frequencies around 1 mHz. As we do not have m numbers, we cannot calculate drifting periods for the particles to link UAA events to substorm onsets to confirm the theory by James et al. (2013). However, we do expect high-m numbers for the equatorward-propagating population due to a lack of corresponding magnetometer signatures. Additionally, poloidal polarization is more likely during quiet geomagnetic conditions. Quiet conditions allow the energetic particle populations, which are necessary to drive the waves, to drift after injection at midnight to the flanks of the magnetosphere (Yeoman et al., 2000). Most of our events correspond to quiet conditions as indicated by the SME index. Examples of ULF waves with equatorward phase propagation in SuperDARN radar data can be found in Yeoman et al. (2008) and Yeoman et al. (2010) and Michael et al. (2024) among others. Yeoman et al. (2008) observed an equatorward and westward propagating ULF wave ($m \sim -60$; frequency $\sim$ 3.3 mHz) above Svalbard. The waves could be driven by wave-particle interactions with a drifting ion population with energies around 10 keV. Yeoman et al. (2010) reported a 1.7 mHz wave with $m \sim +13$ and an eastward and equatorward phase propagation above Svalbard. It is expected that these waves were also excited by drift resonance. However, the eastward propagation direction suggests that the energy source is a (~30 keV) drifting electron population rather than an ion population following the theory described by Mager and Klimushkin (2008) and Mager et al. (2009). More recently, Michael et al. (2024) reported a 0.75 mHz equatorward, eastward propagating ULF wave with $m = 17 \pm 1$. This wave has its energy source from a drift resonance interaction with 13 ± 5 keV electrons which were injected during a magnetospheric substorm before drifting eastwards.

To investigate the possibility that these small-scale, poloidal ULF waves can be generated through wave-particle interactions at these high-latitudes (Wilson et al., 2006) investigated the likelihood of the required driving particle populations being available. Although their study was limited to ion populations, they found that suitable ion populations can be available at latitudes relevant to this study although their occurrence is rare. Takahashi et al. (2013) reported observations of high-m poloidal waves recorded from space without ground-based magnetic signatures. Drift resonance is the most likely wave excitation mechanism at high-latitudes. At these latitudes, both ions and electrons can contribute to such wave excitation, resulting in westward (eastward) wave propagation when excited by ions (electrons). The energy needed for drift resonance around L-shell 11 is around 15 keV (5 keV) for ions (electrons).

Another possible energy source for the UAAs comes in the form of a fast mode compressional wave which propagates sunward from the magnetotail and drives the required standing wave mode in a similar way to that of the 'traditional' toroidal, FLR theory discussed by e.g. Rankin et al. (2021). This was presented as a possibility by both Baddeley et al. (2017) and Mathews et al. (2004). As explained in Mathews et al. (2004), at the high-latitude location of Svalbard, the field lines on the dawn and dusk flanks are stretched out down into the magnetotail. This stretched morphology can lead to an additional phase lag (related to the increased propagation time of the fast mode wave across the magnetic field lines, in the equatorial plane of the magnetosphere). If this phase lag is large enough it can cause the latitude-phase relation to reverse ($d\phi/dlat > 0$) leading to apparent equatorward phase propagation of the UAAs in the ionosphere. Any waves generated through this mechanism would have a resulting sunward as well as equatorward propagation. It is well known that the magnetotail can host a wide range of fast mode waves capable of coupling to a toroidal mode (e.g. Leonovich et al., 2016; Volwerk, 2016). However, the lack of ground magnetometer signature associated with our events suggests that the waves are more small-scale, and poloidal mode.

Combining the studies of small-scale ULF waves using radars, discussed above, with the optical and magnetometer data from our study, we thus suggest that UAAs cannot solely be due to FLR type structures. We believe that they can also be generated by smaller-scale waves with poloidal or, possibly, mixed eigenmode structures. In this case, the UAAs are most likely internally generated by different wave-particle interactions. A lack of optical data in combination with the difficulty of identifying this group of UAAs could explain the lack of previous observations.

The auroral signature associated with small-scale waves indicates that these waves have accompanying kinetic energy fluxes. Van Hazendonk et al. (2024) showed that the kinetic flux was almost equal to the electromagnetic flux for a large scale ULF wave event. We do thus suggest to take both rates into account when calculating ionospheric energy dissipation rates for small-scale ULF waves as well.

5.3. Additional contributing factors

Alternatively, other optical phenomena could be responsible for part of the moving arc signatures, both poleward and equatorward, in the MSP keograms. A phenomena that matches with our high-latitude location, MLT regions of interest and keogram signature are transpolar or sun-aligned arcs. Milan et al. (2005) proposed a formation mechanism in which the IMF B_y component could control the movement of such arcs during lobe reconnection, which predominantly occurs under northward IMF. The sign of IMF B_y then determines on which side of the auroral oval the arcs are formed and their directionality (Kullen et al., 2015; Fear and Milan, 2012). More specifically, poleward propagation of arcs is expected for formation at dawn when $B_y > 0$ and at dusk for $B_y < 0$. This would fit with our observations as shown in Fig. 6a. However, the predominant negative B_z values during poleward propagation indicates that it is unlikely that a significant part of our poleward-propagating population could classify as transpolar or sun-aligned arcs. Our equatorward-propagating population shows a less clear B_y trend. The negative B_z values during dawn make it unlikely that this population is strongly influenced by transpolar arcs. Additionally, it is rare that any of these optical phenomena occur at periodic intervals as needed for ULF wave detection (Reidy et al., 2017). We do thus not expect our statistics to be drastically influenced by transpolar or sun-aligned arcs, but there could be single occurrences. Other high-latitude phenomena, such as auroral streamers (Gallardo-Lacourt et al., 2014), and PMAFs (Xing et al., 2012) are unlikely to be detected as they occur outside our MLT regions of interest.

In general, we note that local variations in the geometry of the magnetic field lines could significantly affect the propagation of ULF waves in the high-latitude magnetosphere (Engebretson et al., 2006). Furthermore, the high-latitude location (around 75° mlat) causes Svalbard to move out of the auroral oval into the polar cap. Especially at dusk, contraction and expansion of the oval is strong due to substorm activity, thus resulting in a more dynamic auroral oval (Laundal et al., 2010). The sign of IMF B_y also affects the strength of geomagnetic activity at high-latitude (Holappa and Mursula, 2018). In addition, a nonzero IMF B_y can cause asymmetries in the high-latitude convection pattern (Pitkänen et al., 2024). More explicitly, in northern winter, the polar cap is larger for positive IMF B_y compared to negative values (Reistad et al., 2020). Due to the unique location of Svalbard, we thus believe that some of the IMF clock angle dependence is due to the relative position of Svalbard with respect to the auroral oval rather than ULF wave propagation and/or generation being influenced by the clock angle.

Furthermore, we suggest further investigation of equatorward-propagating UAAs to gain more insights into their generation mechanisms and their possible link to high-latitude locations such as Svalbard. This paper provides a first statistical overview of this new population of auroral arcs.

6. Conclusions and future work

In this paper, we presented the first statistical study of high-latitude UAAs using an automated detection algorithm. Using 17 seasons, from November – February, of data we detected 198 separate events in optical keograms (630.0 nm) from the MSP located on Svalbard. The results are thus valid at high-latitude in the northern hemisphere winter. A new, equatorward-propagating population was found (72 events). The lack of ground magnetometer signature, coupled with the prevailing solar wind conditions leads us to suggest that they correspond to small-scale, poloidal ULF waves with a generation mechanism internal to the magnetosphere through some form of wave-particle interactions. Similar cases have previously been reported by studies using radar data. This study shows that even these small-scale waves can have associated auroral emissions, and thus significant kinetic energy fluxes. The other, poleward-propagating population (126 events) showed similar properties to the previous redline statistical study by Gillies et al. (2018), both in occurrence probability and dawn-dusk asymmetry. We thus believe that part of this poleward-propagating population corresponds to FAAs. However, a lack of correlating magnetometer signature for part of the poleward-propagating UAAs leads us to believe that this population also contains small-scale ULF waves with similar internal generation mechanisms as the equatorward-propagating population. Both wave populations show low frequencies as expected due to the high-latitude location. The high-latitude location might further influence the occurrence of the ULF waves due to its location on the border of the polar cap and the auroral oval. A subset of the ULF waves detected at 630.0 nm shows an accompanying signature in the 557.7 nm channel, indicating higher kinetic energy dissipation rates.

In the future, the data set created in this paper could be used as a training dataset for a machine learning tool. Thus, allowing the optimization of the detection method and potentially extending the detection method to other optical instrumentation. The algorithm could be used to narrow down the search criteria for identifying moving arc signatures in such future datasets. Additionally, this data set might also be used to cross-correlate ULF wave events in optical data to other data sources such as incoherent scatter data to gain more insights into the energy dissipation of ULF waves. Alternatively, the data set could be used to help modeling efforts into the formation of arcs (Rankin et al., 2021).

CRediT authorship contribution statement

C.M. van Hazendonk: Writing – original draft, Writing – review & editing, Visualization, Software, Investigation, Data curation, Validation, Methodology, Formal analysis, Conceptualization. **L. Baddeley:** Writing – review & editing, Project administration, Investigation, Conceptualization, Supervision, Methodology, Funding acquisition. **K.M. Laundal:** Supervision, Investigation, Writing – review & editing, Methodology, Conceptualization. **D.A. Lorentzen:** Data curation, Writing – review & editing.

Declaration of competing interest

The authors declare that they have no known competing financial interests or personal relationships that could have appeared to influence the work reported in this paper.

Acknowledgments

This work was partly funded by the Norwegian Research Council (NRC) under contract 309135. Karl Laundal was also funded by the NRC through grant 300844/F50 and by the European Union (ERC, DynaMIT, 101086985). We want to acknowledge A.L. Aruliah and I. McWhirter, Atmospheric Physics Laboratory, University College London, Gower Street, London, WC1E 6BT, UK for sharing their cloud detection data. We thank the institutes who maintain the IMAGE Magnetometer Array, in this case specifically the Tromsø Geophysical Observatory of UiT the Arctic University of Norway (Norway), and the Institute of Geophysics Polish Academy of Sciences (Poland). We gratefully acknowledge the SuperMAG collaborators (https://supermag.jhuapl.edu/info/?page=acknowledgement). Lastly, we want to thank Mikko Syrjäsuo for his help on the MSP data description.

Appendix A. Supplementary data

Supplementary material related to this article can be found online at https://doi.org/10.1016/j.jastp.2025.106585.

Data statement

Quicklook keograms of the MSP data can be obtained via the website of KHO at https://kho.unis.no/Keograms/keograms.php. The calibrated MSP data as a function of elevation angle for the dawn and dusk intervals with detection is available through the NIRD research data archive under DOI https://doi.org/10.11582/2025.B9FR665W. Data from the UCL cloud sensor is available through Zenodo under DOI https://doi.org/10.5281/zenodo.14931122 (Aruliah and McWhirter, 2025).

Solar wind data were obtained from the GSFC/SPDF OMNIWeb interface, more specifically from OMNIWeb High Resolution Solar Wind data shifted to bowshock nose: plots and lists interface at https://omniweb.gsfc.nasa.gov/form/sc_merge_min1.html. Data from the IMAGE magnetometer network is available via https://space.fmi.fi/image/. Event lists for dawn and dusk can be found in the supporting information and include start and end time for each event as well as frequency, wave number, and velocity.

References

Agapitov, A.V., Cheremnykh, O.K., 2011. Polarization of ULF waves in the earth's magnetosphere. Kinemat. Phys. Celest. Bodies 27 (3), 117–123. http://dx.doi.org/10.3103/S0884591311030020, URL: http://link.springer.com/10.3103/S0884591311030020.

Anderson, B.J., Engebretson, M.J., Rounds, S.P., Zanetti, L.J., Potemra, T.A., 1990. A statistical study of Pc 3–5 pulsations observed by the AMPTE/CCE magnetic fields experiment, 1. Occurrence distributions. J. Geophys. Res.: Space Phys. 95 (A7), 10495–10523. http://dx.doi.org/10.1029/JA095iA07p10495, URL: https://agupubs.onlinelibrary.wiley.com/doi/10.1029/JA095iA07p10495.

Aruliah, A., McWhirter, I., 2025. Aurora cloud sensor III data - University college London - Kjell Henriksen observatory. http://dx.doi.org/10.5281/ZENODO.14931122, URL: https://zenodo.org/doi/10.5281/zenodo.14931122.

Baddeley, L.J., Lorentzen, D.A., Partamies, N., Denig, M., Pilipenko, V.A., Oksavik, K., Chen, X., Zhang, Y., 2017. Equatorward propagating auroral arcs driven by ULF wave activity: Multipoint ground- and space-based observations in the dusk sector auroral oval: ULF wave-driven auroral arcs. J. Geophys. Res.: Space Phys. 122 (5), 5591–5605. http://dx.doi.org/10.1002/2016JA023427, URL: http://doi.wiley.com/10.1002/2016JA023427.

Baddeley, L.J., Yeoman, T.K., Wright, D.M., 2005. HF doppler sounder measurements of the ionospheric signatures of small scale ULF waves. Ann. Geophys. 23 (5), 1807–1820. http://dx.doi.org/10.5194/angeo-23-1807-2005, URL: https://angeo.copernicus.org/articles/23/1807/2005/.

Baker, G.J., Donovan, E.F., Jackel, B.J., 2003. A comprehensive survey of auroral latitude Pc5 pulsation characteristics. J. Geophys. Res.: Space Phys. 108 (A10), 2002JA009801. http://dx.doi.org/10.1029/2002JA009801, URL: https://agupubs.onlinelibrary.wiley.com/doi/10.1029/2002JA009801.

Dimitrakoudis, S., Mann, I.R., Balasis, G., Papadimitriou, C., Anastasiadis, A., Daglis, I.A., 2022. On the interplay between solar wind parameters and ULF wave power as a function of geomagnetic activity at high- and mid-latitudes. J. Geophys. Res.: Space Phys. 127 (1), e2021JA029693. http://dx.doi.org/10.1029/2021JA029693, URL: https://agupubs.onlinelibrary.wiley.com/doi/10.1029/2021JA029693.

Engebretson, M., Glassmeier, K.-H., Stellmacher, M., Hughes, W.J., Lühr, H., 1998. The dependence of high-latitude PcS wave power on solar wind velocity and on the phase of high-speed solar wind streams. J. Geophys. Res.: Space Phys. 103 (A11), 26271–26283. http://dx.doi.org/10.1029/97JA03143, URL: https://agupubs.onlinelibrary.wiley.com/doi/10.1029/97JA03143.

Engebretson, M.J., Posch, J.L., Pilipenko, V.A., Chugunova, O.M., 2006. ULF waves at very high latitudes. In: Takahashi, K., Chi, P.J., Denton, R.E., Lysak, R.L. (Eds.), Geophysical Monograph Series. Vol. 169, American Geophysical Union, Washington, D. C., pp. 137–156. http://dx.doi.org/10.1029/169GM10, URL: https://onlinelibrary.wiley.com/doi/10.1029/169GM10.

Fear, R.C., Milan, S.E., 2012. The IMF dependence of the local time of transpolar arcs: Implications for formation mechanism. J. Geophys. Res.: Space Phys. 117 (A3), 2011JA017209. http://dx.doi.org/10.1029/2011JA017209, URL: https://agupubs.onlinelibrary.wiley.com/doi/10.1029/2011JA017209.

Fenrich, F.R., Samson, J.C., 1997. Growth and decay of field line resonances. J. Geophys. Res.: Space Phys. 102 (A9), 20031–20039. http://dx.doi.org/10.1029/97JA01376, URL: https://agupubs.onlinelibrary.wiley.com/doi/10.1029/97JA01376.

Gallardo-Lacourt, B., Nishimura, Y., Lyons, L.R., Zou, S., Angelopoulos, V., Donovan, E., McWilliams, K.A., Ruohoniemi, J.M., Nishitani, N., 2014. Coordinated SuperDARN themis ASI observations of mesoscale flow bursts associated with auroral streamers. J. Geophys. Res.: Space Phys. 119 (1), 142–150. http://dx.doi.org/10.1002/2013JA019245, URL: https://agupubs.onlinelibrary.wiley.com/doi/10.1002/2013JA019245.

Gillies, D.M., Knudsen, D., Rankin, R., Milan, S., Donovan, E., 2018. A statistical surveyof the 630.0-nm optical signature of periodic auroral arcs resulting from magnetospheric field line resonances. Geophys. Res. Lett. 45 (10), 4648–4655. http://dx.doi.org/10.1029/2018GL077491, URL: https://agupubs.onlinelibrary.wiley.com/doi/10.1029/2018GL077491.

Gjerloev, J.W., 2012. The SuperMAG data processing technique. J. Geophys. Res.: Space Phys. 117 (A9), 2012JA017683. http://dx.doi.org/10.1029/2012JA017683, URL: https://agupubs.onlinelibrary.wiley.com/doi/10.1029/2012JA017683.

Hartinger, M.D., Moldwin, M.B., Zou, S., Bonnell, J.W., Angelopoulos, V., 2015. ULF wave electromagnetic energy flux into the ionosphere: Joule heating implications. J. Geophys. Res.: Space Phys. 120 (1), 494–510. http://dx.doi.org/10.1002/2014JA020129, URL: http://doi.wiley.com/10.1002/2014JA020129.

Herlingshaw, K., Partamies, N., Van Hazendonk, C.M., Syrjäsuo, M., Baddeley, L.J., Johnsen, M.G., Eriksen, N.K., McWhirter, I., Aruliah, A., Engebretson, M.J., Oksavik, K., Sigernes, F., Lorentzen, D.A., Nishiyama, T., Cooper, M.B., Meriwether, J., Haaland, S., Whiter, D., 2025. Science highlights from the Kjell henriksen observatory on Svalbard. Arct. Sci. 11, 1–25. http://dx.doi.org/10.1139/as-2024-0009, URL: https://cdnsciencepub.com/doi/10.1139/as-2024-0009.

Holappa, L., Mursula, K., 2018. Explicit IMF B_y dependence in high-latitude geomagnetic activity. J. Geophys. Res.: Space Phys. 123 (6), 4728–4740. http://dx.doi.org/10.1029/2018JA025517, URL: https://agupubs.onlinelibrary.wiley.com/doi/10.1029/2018JA025517.

Hynönen, R., Tanskanen, E.I., Francia, P., 2020. Solar cycle evolution of ULF wave power in solar wind and on ground. J. Space Weather. Space Clim. 10, 43. http://dx.doi.org/10.1051/swsc/2020046, URL: https://www.swsc-journal.org/10.1051/swsc/2020046.

James, M.K., Yeoman, T.K., Mager, P.N., Klimushkin, D.Y., 2013. The spatio-temporal characteristics of ULF waves driven by substorm injected particles. J. Geophys. Res.: Space Phys. 118 (4), 1737–1749. http://dx.doi.org/10.1002/jgra.50131, URL: https://agupubs.onlinelibrary.wiley.com/doi/10.1002/jgra.50131.

Kavosi, S., Raeder, J., 2015. Ubiquity of Kelvin–Helmholtz waves at earth's magnetopause. Nat. Commun. 6 (1), 7019. http://dx.doi.org/10.1038/ncomms8019, URL: https://www.nature.com/articles/ncomms8019.

Kivelson, M.G., Southwood, D.J., 1986. Coupling of global magnetospheric MHD eigenmodes to field line resonances. J. Geophys. Res.: Space Phys. 91 (A4), 4345–4351. http://dx.doi.org/10.1029/JA091iA04p04345, URL: https://agupubs.onlinelibrary.wiley.com/doi/10.1029/JA091iA04p04345.

Korotova, G., Sibeck, D., 2024. Themis observations of compressional Pc5 pulsations in the dawn- and duskside magnetosphere. Adv. Space Res. S0273117724009487. http://dx.doi.org/10.1016/j.asr.2024.09.028, URL: https://linkinghub.elsevier.com/retrieve/pii/S0273117724009487.

Kosch, M.J., Honary, F., Del Pozo, C.F., Marple, S.R., Hagfors, T., 2001. High-resolution maps of the characteristic energy of precipitating auroral particles. J. Geophys. Res.: Space Phys. 106 (A12), 28925–28937. http://dx.doi.org/10.1029/2001JA900107, URL: https://agupubs.onlinelibrary.wiley.com/doi/10.1029/2001JA900107.

Kozlovsky, A.E., Nilsson, H., Safargaleev, V.V., 2006. Complex study of the auroral arc dynamics and ionospheric plasma convection in prenoon hours. Geomagn. Aeron. 46 (4), 473–484. http://dx.doi.org/10.1134/S0016793206040098, URL: http://link.springer.com/10.1134/S0016793206040098.

Kozyreva, O.V., Pilipenko, V.A., Shi, X., Bland, E.C., Baddeley, L., 2022. Polar cap ULF pulsations: Coordinated radar-magnetometer observations. In: Kosterov, A., Bobrov, N., Gordeev, E., Kulakov, E., Lyskova, E., Mironova, I. (Eds.), Problems of Geocosmos–2020. In: Springer Proceedings in Earth and Environmental Sciences, Springer International Publishing, Cham, pp. 431–450. http://dx.doi.org/10.1007/978-3-030-91467-7_32, URL: https://link.springer.com/10.1007/978-3-030-91467-7_32.

Kullen, A., Fear, R.C., Milan, S.E., Carter, J.A., Karlsson, T., 2015. The statistical difference between bending arcs and regular polar arcs. J. Geophys. Res.: Space Phys. 120 (12), http://dx.doi.org/10.1002/2015JA021298, URL: https://agupubs.onlinelibrary.wiley.com/doi/10.1002/2015JA021298.

Kwon, H.-J., Kim, K.-H., Jee, G., Jin, H., Kim, H., Shin, J., Lee, S., Kwon, J.-W., Kim, J.-H., Lee, C., Lessard, M., 2019. Characteristics of Pc5 activity at high latitudes stations in antarctica. J. Atmos. Sol.-Terr. Phys. 193, 105087. http://dx.doi.org/10.1016/j.jastp.2019.105087, URL: https://linkinghub.elsevier.com/retrieve/pii/S1364682619301361.

Laundal, K.M., Østgaard, N., Frey, H.U., Weygand, J.M., 2010. Seasonal and interplanetary magnetic field–dependent polar cap contraction during substorm expansion phase. J. Geophys. Res.: Space Phys. 115 (A11), 2010JA015910. http://dx.doi.org/10.1029/2010JA015910, URL: https://agupubs.onlinelibrary.wiley.com/doi/10.1029/2010JA015910.

Leonovich, A.S., Mazur, V.A., Kozlov, D.A., 2016. MHD oscillations in the earth's magnetotail: Theoretical studies. In: Keiling, A., Lee, D.-H., Nakariakov, V. (Eds.), Geophysical Monograph Series, first ed. Wiley, pp. 161–179. http://dx.doi.org/10.1002/9781119055006.ch10, URL: https://agupubs.onlinelibrary.wiley.com/doi/10.1002/9781119055006.ch10.

Liou, K., Sibeck, D.G., 2014. Study of a global auroral Pc5 pulsation event with concurrent ULF waves. Geophys. Res. Lett. 41 (19), 6547–6555. http://dx.doi.org/10.1002/2014GL060755.

Lysak, R.L., 2023. Kinetic Alfvén waves and auroral particle acceleration: A review. Rev. Mod. Plasma Phys. 7 (1), 6. http://dx.doi.org/10.1007/s41614-022-00111-2.

Mager, P.N., Klimushkin, D.Y., 2008. Alfvén ship waves: high-m ULF pulsations in the magnetosphere generated by a moving plasma inhomogeneity. Ann. Geophys. 26 (6), 1653–1663. http://dx.doi.org/10.5194/angeo-26-1653-2008, URL: https://angeo.copernicus.org/articles/26/1653/2008/.

Mager, P.N., Klimushkin, D.Y., Ivchenko, N., 2009. On the equatorward phase propagation of high-m ULF pulsations observed by radars. J. Atmos. Sol.-Terr. Phys. 71 (16), 1677–1680. http://dx.doi.org/10.1016/j.jastp.2008.09.001, URL: https://linkinghub.elsevier.com/retrieve/pii/S1364682608002356.

Mann, I.R., Wright, A.N., Mills, K.J., Nakariakov, V.M., 1999. Excitation of magnetospheric waveguide modes by magnetosheath flows. J. Geophys. Res.: Space Phys. 104 (A1), 333–353. http://dx.doi.org/10.1029/1998JA900026, URL: https://agupubs.onlinelibrary.wiley.com/doi/10.1029/1998JA900026.

Marocco, A., 2024. Cloud Sensor Data Validation with Manually Labelled All-Sky Images and Weather Measurements. Technical Report, The University Centre in Svalbard, URL: https://aurora.unis.no/doc/CloudSensorValidation.pdf.

Mathews, J.T., Mann, I.R., Rae, I.J., Moen, J., 2004. Multi-instrument observations of ULF wave-driven discrete auroral arcs propagating sunward and equatorward from the poleward boundary of the duskside auroral oval. Phys. Plasmas 11 (4), 1250–1259. http://dx.doi.org/10.1063/1.1647137, URL: https://pubs.aip.org/pop/article/11/4/1250/105082/Multi-instrument-observations-of-ULF-wave-driven.

Michael, C.M., Yeoman, T.K., Wright, D.M., Chelpanov, M.A., Mager, P.N., 2024. Evolving phase propagation in an intermediate- *m* ULF wave driven by substorm-injected particles. J. Geophys. Res.: Space Phys. 129 (3), e2023JA031654. http://dx.doi.org/10.1029/2023JA031654, URL: https://agupubs.onlinelibrary.wiley.com/doi/10.1029/2023JA031654.

Milan, S.E., Hubert, B., Grocott, A., 2005. Formation and motion of a transpolar arc in response to dayside and nightside reconnection. J. Geophys. Res.: Space Phys. 110 (A1), 2004JA010835. http://dx.doi.org/10.1029/2004JA010835, URL: https://agupubs.onlinelibrary.wiley.com/doi/10.1029/2004JA010835.

Milan, S.E., Sato, N., Ejiri, M., Moen, J., 2001. Auroral forms and the field-aligned current structure associated with field line resonances. J. Geophys. Res.: Space Phys. 106 (A11), 25825–25833. http://dx.doi.org/10.1029/2001JA900077, URL: https://agupubs.onlinelibrary.wiley.com/doi/10.1029/2001JA900077.

Milan, S.E., Yeoman, T.K., Lester, M., Moen, J., Sandholt, P.E., 1999. Post-noon two-minute period pulsating aurora and their relationship to the dayside convection pattern. Ann. Geophys. 17 (7), 877–891. http://dx.doi.org/10.1007/s00585-999-0877-8, URL: https://angeo.copernicus.org/articles/17/877/1999/.

Morita, K., Ponomarenko, P., Nishitani, N., Hori, T., Shepherd, S.G., 2024. Polarization and m m-number characteristics of mid-latitude Pc5 ULF waves observed by SuperDARN radars. J. Geophys. Res.: Space Phys. 129 (9), e2024JA032592. http://dx.doi.org/10.1029/2024JA032592, URL: https://agupubs.onlinelibrary.wiley.com/doi/10.1029/2024JA032592.

Motoba, T., Ogawa, Y., Ebihara, Y., Kadokura, A., Gerrard, A.J., Weatherwax, A.T., 2021. Daytime Pc5 diffuse auroral pulsations and their association with outer magnetospheric ULF waves. J. Geophys. Res.: Space Phys. 126 (8), e2021JA029218. http://dx.doi.org/10.1029/2021JA029218, URL: https://agupubs.onlinelibrary.wiley.com/doi/10.1029/2021JA029218.

Newell, P.T., Gjerloev, J.W., 2011. Evaluation of SuperMAG auroral electrojet indices as indicators of substorms and auroral power. J. Geophys. Res.: Space Phys. 116 (A12), 2011JA016779. http://dx.doi.org/10.1029/2011JA016779, URL: https://onlinelibrary.wiley.com/doi/10.1029/2011JA016779.

NOAA Space Weather Prediction Center, 2016. Deep space climate observatory (DSCOVR). http://dx.doi.org/10.7289/V51Z42F7, URL: https://www.ncei.noaa.gov/access/metadata/landing-page/bin/iso?id=gov.noaa.ngdc.stp.swx:satellite-systems_dscovr.

Pahud, D., Rae, I., Mann, I., Murphy, K., Amalraj, V., 2009. Ground-based Pc5 ULF wave power: Solar wind speed and MLT dependence. J. Atmos. Sol.-Terr. Phys. 71 (10–11), 1082–1092. http://dx.doi.org/10.1016/j.jastp.2008.12.004, URL: https://linkinghub.elsevier.com/retrieve/pii/S1364682608003957.

Partamies, N., Whiter, D., Kauristie, K., Massetti, S., 2022. Local Time Dependence of Auroral Peak Emission Height and Morphology. Preprint, Magnetosphere & space plasma physics/Auroral ionosphere, http://dx.doi.org/10.5194/angeo-2022-6, URL: https://angeo.copernicus.org/preprints/angeo-2022-6/angeo-2022-6.pdf.

Pilipenko, V., Belakhovsky, V., Kozlovsky, A., Fedorov, E., Kauristie, K., 2012. Determination of the wave mode contribution into the ULF pulsations from combined radar and magnetometer data: Method of apparent impedance. J. Atmos. Sol.-Terr. Phys. 77, 85–95. http://dx.doi.org/10.1016/j.jastp.2011.11.013, URL: https://linkinghub.elsevier.com/retrieve/pii/S1364682611003166.

Pitkänen, T., Kullen, A., Chong, G.S., 2024. Importance of the dusk-dawn interplanetary magnetic field component (IMF by) to magnetospheric convection in earth's magnetotail plasma sheet. Front. Astron. Space Sci. 11, 1373249. http://dx.doi.org/10.3389/fspas.2024.1373249, URL: https://www.frontiersin.org/articles/10.3389/fspas.2024.1373249/full.

Rae, I.J., Murphy, K.R., Watt, C.E.J., Halford, A.J., Mann, I.R., Ozeke, L.G., Sibeck, D.G., Clilverd, M.A., Rodger, C.J., Degeling, A.W., Forsyth, C., Singer, H.J., 2018. The role of localized compressional ultra-low frequency waves in energetic electron precipitation. J. Geophys. Res.: Space Phys. 123 (3), 1900–1914. http://dx.doi.org/10.1002/2017JA024674.

Rae, I.J., Murphy, K.R., Watt, C.E.J., Rostoker, G., Rankin, R., Mann, I.R., Hodgson, C.R., Frey, H.U., Degeling, A.W., Forsyth, C., 2014. Field line resonances as a trigger and a tracer for substorm onset. J. Geophys. Res.: Space Phys. 119 (7), 5343–5363. http://dx.doi.org/10.1002/2013JA018889, URL: https://agupubs.onlinelibrary.wiley.com/doi/10.1002/2013JA018889.

Rae, I.J., Watt, C.E.J., Fenrich, F.R., Mann, I.R., Ozeke, L.G., Kale, A., 2007. Energy deposition in the ionosphere through a global field line resonance. Ann. Geophys. 25 (12), 2529–2539. http://dx.doi.org/10.5194/angeo-25-2529-2007, URL: https://angeo.copernicus.org/articles/25/2529/2007/.

Rankin, R., Gillies, D.M., Degeling, A.W., 2021. On the relationship between shear Alfvén waves, auroral electron acceleration, and field line resonances. Space Sci. Rev. 217 (4), 60. http://dx.doi.org/10.1007/s11214-021-00830-x, URL: https://link.springer.com/10.1007/s11214-021-00830-x.

Reidy, J.A., Fear, R.C., Whiter, D.K., Lanchester, B.S., Kavanagh, A.J., Paxton, L.J., Zhang, Y., Lester, M., 2017. Multi-instrument observation of simultaneous polar cap auroras on open and closed magnetic field lines. J. Geophys. Res.: Space Phys. 122 (4), 4367–4386. http://dx.doi.org/10.1002/2016JA023718, URL: https://agupubs.onlinelibrary.wiley.com/doi/10.1002/2016JA023718.

Reistad, J.P., Laundal, K.M., Ohma, A., Moretto, T., Milan, S.E., 2020. An explicit IMF B dependence on solar wind-magnetosphere coupling. Geophys. Res. Lett. 47 (1), e2019GL086062. http://dx.doi.org/10.1029/2019GL086062, URL: https://agupubs.onlinelibrary.wiley.com/doi/10.1029/2019GL086062.

Samson, J.C., Cogger, L.L., Pao, Q., 1996. Observations of field line resonances, auroral arcs, and auroral vortex structures. J. Geophys. Res.: Space Phys. 101 (A8), 17373–17383. http://dx.doi.org/10.1029/96JA01086, URL: https://agupubs.onlinelibrary.wiley.com/doi/10.1029/96JA01086.

Samson, J.C., Harrold, B.G., Ruohoniemi, J.M., Greenwald, R.A., Walker, A.D.M., 1992. Field line resonances associated with MHD waveguides in the magnetosphere. Geophys. Res. Lett. 19 (5), 441–444. http://dx.doi.org/10.1029/92GL00116, URL: https://agupubs.onlinelibrary.wiley.com/doi/10.1029/92GL00116.

Samson, J.C., Rankin, R., Tikhonchuk, V.T., 2003. Optical signatures of auroral arcs produced by field line resonances: comparison with satellite observations and modeling. Ann. Geophys. 21 (4), 933–945. http://dx.doi.org/10.5194/angeo-21-933-2003, URL: https://angeo.copernicus.org/articles/21/933/2003/.

Shi, X., Ruohoniemi, J.M., Baker, J.B.H., Lin, D., Bland, E.C., Hartinger, M.D., Scales, W.A., 2018. Survey of ionospheric Pc3-5 ULF wave signatures in SuperDARN high time resolution data. J. Geophys. Res.: Space Phys. 123 (5), 4215–4231. http://dx.doi.org/10.1029/2017JA025033, URL: https://onlinelibrary.wiley.com/doi/10.1029/2017JA025033.

Takahashi, K., Hartinger, M.D., Angelopoulos, V., Glassmeier, K.-H., Singer, H.J., 2013. Multispacecraft observations of fundamental poloidal waves without ground magnetic signatures. J. Geophys. Res.: Space Phys. 118 (7), 4319–4334. http://dx.doi.org/10.1002/jgra.50405, URL: https://agupubs.onlinelibrary.wiley.com/doi/10.1002/jgra.50405.

Takahashi, K., Higbie, P.R., Baker, D.N., 1985. Azimuthal propagation and frequency characteristic of compressional Pc 5 waves observed at geostationary orbit. J. Geophys. Res.: Space Phys. 90 (A2), 1473–1485. http://dx.doi.org/10.1029/JA090iA02p01473, URL: https://agupubs.onlinelibrary.wiley.com/doi/10.1029/JA090iA02p01473.

Van Hazendonk, C.M., Baddeley, L., Laundal, K.M., Chau, J.L., 2024. Detection and energy dissipation of ULF waves in the polar ionosphere: A case study using the EISCAT radar. J. Geophys. Res.: Space Phys. 129 (7), e2024JA032633. http://dx.doi.org/10.1029/2024JA032633, URL: https://agupubs.onlinelibrary.wiley.com/doi/10.1029/2024JA032633.

Volwerk, M., 2016. ULF wave modes in the earth's magnetotail. In: Keiling, A., Lee, D.-H., Nakariakov, V. (Eds.), Geophysical Monograph Series, first ed. Wiley, pp. 139–160. http://dx.doi.org/10.1002/9781119055006.ch9, URL: https://agupubs.onlinelibrary.wiley.com/doi/10.1002/9781119055006.ch9.

Wang, B., Nishimura, Y., Hartinger, M., Sivadas, N., Lyons, L.L., Varney, R.H., Angelopoulos, V., 2020. Ionospheric modulation by storm time Pc5 ULF pulsations and the structure detected by PFISR-themis conjunction. Geophys. Res. Lett. 47 (16), e2020GL089060. http://dx.doi.org/10.1029/2020GL089060.

Wilson, M.E., Yeoman, T.K., Baddeley, L.J., Kellet, B.J., 2006. A statistical investigation of the invariant latitude dependence of unstable magnetospheric ion populations in relation to high m ULF wave generation. Ann. Geophys. 24 (11), 3027–3040. http://dx.doi.org/10.5194/angeo-24-3027-2006, URL: https://angeo.copernicus.org/articles/24/3027/2006/.

Witasse, O., Lilensten, J., Lathuillère, C., Blelly, P.-L., 1999. Modeling the OI 630.0 and 557.7 nm thermospheric dayglow during EISCAT-WINDII coordinated measurements. J. Geophys. Res.: Space Phys. 104 (A11), 24639–24655. http://dx.doi.org/10.1029/1999JA900260, URL: https://agupubs.onlinelibrary.wiley.com/doi/10.1029/1999JA900260.

Wright, A.N., Mann, I.R., 2006. Global MHD eigenmodes of the outer magnetosphere. In: Takahashi, K., Chi, P.J., Denton, R.E., Lysak, R.L. (Eds.), Geophysical Monograph Series. Vol. 169, American Geophysical Union, Washington, D. C., pp. 51–72. http://dx.doi.org/10.1029/169GM06, URL: https://onlinelibrary.wiley.com/doi/10.1029/169GM06.

Wright, D.M., Yeoman, T.K., 1999. High-latitude HF Doppler observations of ULF waves: 2. Waves with small spatial scale sizes. Ann. Geophys. 9. http://dx.doi.org/10.1007/s00585-999-0868-9.

Xing, Z., Yang, H., Han, D., Wu, Z., Hu, Z., Zhang, Q., Kamide, Y., Hu, H., Zhang, B., Liu, J., Huang, D., 2012. Poleward moving auroral forms (PMAFs) observed at the Yellow River Station: A statistical study of its dependence on the solar wind conditions. J. Atmos. Sol.-Terr. Phys. 86, 25–33. http://dx.doi.org/10.1016/j.jastp.2012.06.004, URL: https://linkinghub.elsevier.com/retrieve/pii/S1364682612001472.

Yeoman, T.K., Baddeley, L.J., Dhillon, R.S., Robinson, T.R., Wright, D.M., 2008. Bistatic observations of large and small scale ULF waves in SPEAR-induced HF coherent backscatter. Ann. Geophys. 26 (8), 2253–2263. http://dx.doi.org/10.5194/angeo-26-2253-2008, URL: https://angeo.copernicus.org/articles/26/2253/2008/.

Yeoman, T.K., Klimushkin, D.Y., Mager, P.N., 2010. Intermediate-*m* ULF waves generated by substorm injection: a case study. Ann. Geophys. 28 (8), 1499–1509. http://dx.doi.org/10.5194/angeo-28-1499-2010, URL: https://angeo.copernicus.org/articles/28/1499/2010/.

Yeoman, T.K., Tian, M., Lester, M., Jones, T.B., 1992. A study of Pc5 hydromagnetic waves with equatorward phase propagation. Planet. Space Sci. 40 (6), 797–810. http://dx.doi.org/10.1016/0032-0633(92)90108-Z, URL: https://linkinghub.elsevier.com/retrieve/pii/003206339290108Z.

Yeoman, T.K., Wright, D.M., Chapman, P.J., Stockton-Chalk, A.B., 2000. High-latitude observations of ULF waves with large azimuthal wavenumbers. J. Geophys. Res.: Space Phys. 105 (A3), 5453–5462. http://dx.doi.org/10.1029/1999JA005081, URL: https://agupubs.onlinelibrary.wiley.com/doi/10.1029/1999JA005081.

Yin, Z.-F., Zhou, X.-Z., Hu, Z.-J., Zong, Q.-G., Liu, J.-J., Yue, C., Wang, S., Zhao, X.-X., Yang, H.-G., Li, B., 2023. Multi-band periodic poleward-moving auroral arcs at the postdawn sector: A case study. J. Geophys. Res.: Space Phys. 128 (9), e2023JA031516. http://dx.doi.org/10.1029/2023JA031516, URL: https://agupubs.onlinelibrary.wiley.com/doi/10.1029/2023JA031516.

Zhai, C., Shi, X., Wang, W., Hartinger, M.D., Yao, Y., Peng, W., Lin, D., Ruohoniemi, J.M., Baker, J.B.H., 2021. Characterization of high-m ULF wave signatures in GPS TEC data. Geophys. Res. Lett. 48 (14), e2021GL094282. http://dx.doi.org/10.1029/2021GL094282, URL: https://agupubs.onlinelibrary.wiley.com/doi/10.1029/2021GL094282.

Paper III

High-latitude observations of ULF wave driven ion upflow

van Hazendonk, C. M., Baddeley, L., Laundal, Partamies, N.
Annales Geophysicae, (2025)
doi: 10.5194/egusphere-2025-5220 (preprint, public discussion)

https://doi.org/10.5194/egusphere-2025-5220
Preprint. Discussion started: 4 November 2025

High-latitude observations of ULF wave driven ion upflow

Charlotte M. van Hazendonk[1,2], Lisa J. Baddeley[1,3], Karl M. Laundal[4,2], and Noora Partamies[1]

[1]Department of Arctic Geophysics, The University Centre in Svalbard, Longyearbyen, Norway
[2]Department of Physics and Technology, University of Bergen, Norway
[3]Department of Physics, University of Oslo, Norway
[4]Division of Geomagnetism and Geospace, DTU Space, Technical University of Denmark, Copenhagen, Denmark

Correspondence: Charlotte M. van Hazendonk (charlottva@unis.no)

Abstract. We present a comprehensive study of the first observations of ionospheric ion upflow generated by ultra-low frequency (ULF) wave driven auroral arcs (UAAs). Ground- and space-based instrumentation, together with inversion models, allow us to study the event at different length scales. This shows the complex dynamics of UAAs and their role in the ionosphere-magnetosphere coupling via ion upflow, field-aligned currents (FACs), and energy dissipation. The UAA event was observed as a series of six poleward moving arcs, primarily in the 630.0 nm emission line. At the northern extent of the arcs incoherent scatter radar (ISR) data indicated that the UAAs have driven type 2 ion upflow with low to medium fluxes of around 3.3×10^{13} particles m^{-2} s^{-1}. Data from the ISR, spacecraft, and models, result in FAC magnitudes up to 6 µA m^{-2}, total energy fluxes up to 12 mW m^{-2}, and Joule heating rates up to 11 mW m^{-2} associated with the arcs. These values mostly correspond to localized measurements, while at large-scale the values are up to 50% smaller. In addition, ground-based magnetometers suggested that the UAA event is driven by small-scale ULF waves, while energy dissipation rates and FAC magnitudes are significant and comparable to previously reported large-scale wave events, indicating the importance of using a multi-instrument approach when investigating energy dissipation associated with ULF waves. This event thus shows that even small-scale ULF waves can drive ion upflow in the ionosphere.

1 Introduction

Ion outflow plays a fundamental role in the ionosphere – magnetosphere coupling and outflows contribute significantly to the magnetospheric plasma population (Bjoland et al., 2025). At high-latitudes, ions of ionospheric origin can be energized and lifted to higher altitudes (upflow) where they may escape into the magnetosphere and interplanetary region (outflow). Originally, ion upflow has been categorized into two types where the first is driven by ion heating (type 1) and the second by electron heating (type 2) (Wahlund et al., 1992). Type 1 upflow is characterized by strong perpendicular electric fields, enhanced ion temperatures down to the E region, and low electron densities below 300 km, suggesting a lack of auroral precipitation. The enhanced ion temperature can cause a pressure gradient that accelerates ions upward. Type 2 upflow is associated with enhanced electron temperatures and densities, and is related to auroral arcs. The enhanced electron temperature can lead to an increase in the ambipolar electric field, which then causes ion upflow. Later studies confirmed that these mechanisms

https://doi.org/10.5194/egusphere-2025-5220
Preprint. Discussion started: 4 November 2025

often act simultaneously, showing both enhanced electron and ion temperatures and producing complex ionospheric signatures (Skjæveland et al., 2011).

The European Incoherent Scatter (EISCAT) Svalbard radar (ESR) has been a key instrument in quantifying ion upflow fluxes and statistical characterization of ion upflow (e.g. Ogawa et al., 2009; Ji et al., 2019; Ogawa et al., 2003; Skjæveland et al., 2011, 2014; David et al., 2018, 2024; Bjoland et al., 2025). Most upflow studies focus on the dayside ionosphere, but upflow can happen during all magnetic local times. To separate genuine upflow and downflow from noise in the ESR data, Ogawa et al. (2009) used a threshold of +100 m s^{-1} (-100 m s^{-1}) at three or more consecutive heights along the profile to detect ion upflow (downflow). Subsequent long-term ESR data sets reveal that ion upflow fluxes above Svalbard typically average at 10^{13} particles m^{-2} s^{-1}, but exhibit strong variability with magnetic local time, season, and geomagnetic activity (Ogawa et al., 2011; David et al., 2018). It is possible to divide ion upflow fluxes, f_i, into three categories: low ($1.0 \times 10^{13} \leq f_i \leq 2.5 \times 10^{13}$ m^{-2} s^{-1}), medium ($2.5 \times 10^{13} \leq f_i \leq 7.5 \times 10^{13}$ m^{-2} s^{-1}), and high ($f_i \geq 7.5 \times 10^{13}$ m^{-2} s^{-1}) (David et al., 2018). Low flux upflows occur most often, while medium and high fluxes are largely linked to enhanced geomagnetic conditions.

Ion upflow has been associated with auroral optical emissions in general (Zettergren et al., 2007), and more specifically poleward moving auroral forms (PMAFs) (Skjæveland et al., 2011), pulsating aurora (Godbole et al., 2022), continuum emission (Partamies et al., 2025), and auroral arcs (Lynch et al., 2007), among others.

Another important factor in the redistribution and transport of energy within the Earth's magnetosphere are ultra-low frequency (ULF) waves. ULF waves are magnetohydrodynamic (MHD) oscillations with frequencies ranging from 1 mHz to 1 Hz, and can be observed as Alfvén and compressional waves. One of the most commonly observed types of ULF waves in the Earth's ionosphere is the field line resonance (FLR), a large-scale, standing Alfvén wave that occurs on closed magnetic field lines and transports energy and momentum along these field lines. The azimuthal scale size of ULF waves is described by the *m*-number ($m = 2\pi R_E L/\lambda_{az}$, where R_E is the Earth's radius, L the L-shell location, and λ_{az} the azimuthal wavelength). A low *m*-number describes a large-scale wave with predominantly external generation mechanisms, such as FLRs, while a high *m*-number refers to small-scale standing wave structures, which are often produced internally to the magnetosphere (Menk and Waters, 2013). Optically, ULF waves can be observed by a periodic series of poleward or equatorward moving auroral arcs, corresponding to ULF wave driven auroral arcs (UAAs) (Gillies et al., 2017, 2018; Van Hazendonk et al., 2025). Traditionally, UAA signatures are associated with FLRs as proposed by the model of Samson et al. (2003), in which the parallel electric fields associated with FLRs can accelerate electrons downward creating these periodic auroral arcs signatures. Recently, Van Hazendonk et al. (2024) indicated that smaller-scale ULF waves could also be associated with UAA signatures in both the dawn and dusk sectors. In addition, Fenrich et al. (2019) associated FLRs with field-aligned currents (FACs) and resolved the two-dimensional (2D) velocities and FACs associated with FLRs, finding typical peak FAC magnitudes around 2–4 μA m^{-2}, which occurred in localized latitudinal bands with widths of 1–2°. The energy transport of ULF waves consists of electromagnetic energy, as described by the Poynting vector, and kinetic energy (Hartinger et al., 2015; Van Hazendonk et al., 2024). Most studies on the energy budget of ULF waves solely focus on the energy fluxes into the ionosphere, and ignore any potential mass and/or energy flow out of the ionosphere.

https://doi.org/10.5194/egusphere-2025-5220
Preprint. Discussion started: 4 November 2025

In this comprehensive case study of the high-latitude ionosphere, we aim to determine whether UAA events can be associated with energy dissipation, ion upflow and/or outflow. We present a case study taking place on 16 November 2021 above Svalbard. This event was originally detected in the Meridian Scanning Photometer (MSP) statistical study by Van Hazendonk et al. (2025). Ground-based instrumentation, including the ESR, combined with satellite data and models are used to show the complicated nature of this UAA event and its implications on the role that ULF waves play both in terms of energy dissipation into the ionosphere and the flow of mass out of or upwards in the ionosphere.

2 Data

In this study, we used instruments and models with different scale sizes to put together an extensive overview of a UAA event above Svalbard. The ground-based instrumentation includes the EISCAT Svalbard radar (ESR), a meridian scanning photometer (MSP), and ground-based magnetometers. In addition to ground-based data, we used the Defense Meteorological Satellite Program (DMSP), Iridium, and Swarm spacecraft. Solar wind conditions are obtained from ACE and WIND data, shifted to the bow shock nose with 1 min temporal resolution. The DMSP spacecraft carry payloads to measure precipitating auroral particles (Special Sensor for Precipitating Electron and Ion Spectrometer; SSJ (Redmon et al., 2017)), plasma properties including ion drift velocities (Sensor for Ion and Electron Scintillation; SSIES), and optical emissions in ultraviolet and energy fluxes (Special Sensor Ultraviolet Spectrographic Images; SSUSI; (Paxton et al., 1992)), among others. Both the locations of the ground-based instruments as well as the DMSP overpasses are shown in Figure 1. The ground-based magnetometers in Figure 1 are from the International Monitor for Auroral Geomagnetic Effects (IMAGE) magnetometer network (Tanskanen, 2009) and are located in Tromsø (TRO), Sorøya (SOR), Bjørnøya (BJN), Hopen (HOP), Hornsund (HOR), Longyearbyen (LYR), and Ny-Ålesund (NAL). Part of the data are used in two models, the ELectron Spectrum (ELSPEC) method (Virtanen et al., 2018) and the Local Mapping of Polar Ionospheric Electrodynamics (Lompe) model (Laundal et al., 2022; Hovland et al., 2022), to determine FACs and energy fluxes.

The MSP is located at the Kjell Henriksen Observatory (KHO) (78.09°N, 16.02°E geographic) near Longyearbyen (Herlingshaw et al., 2025), and the ESR is located 600 m north of KHO. The MSP records auroral intensity as a function of elevation angle as it scans along the geomagnetic meridian measuring auroral emissions at wavelengths of 630.0 and 557.7 nm. The auroral emission height is assumed at 250 km (120 km) for the 630.0 nm (557.7 nm) emission (Partamies et al., 2022), enabling conversion from elevation angle into geographic and/or geomagnetic coordinates resulting in the FOVs plotted in Figure 1. The MSP data is plotted in keograms, which show the elevation angle or latitude as a function of time. These keograms can be used to detect UAA events using the detection method presented in Van Hazendonk et al. (2025). This method detects up to four frequency peaks in fast-Fourier transform power spectra with window length of 30 min or 1 h, derived from multiple time series of auroral intensity. These frequency peaks provide wave information such as frequency and propagation velocity and they can be used to reconstruct the wave fronts. More information on the MSP, including how the data were pre-processed for the detection algorithm, can be found in Van Hazendonk et al. (2025).

https://doi.org/10.5194/egusphere-2025-5220
Preprint. Discussion started: 4 November 2025

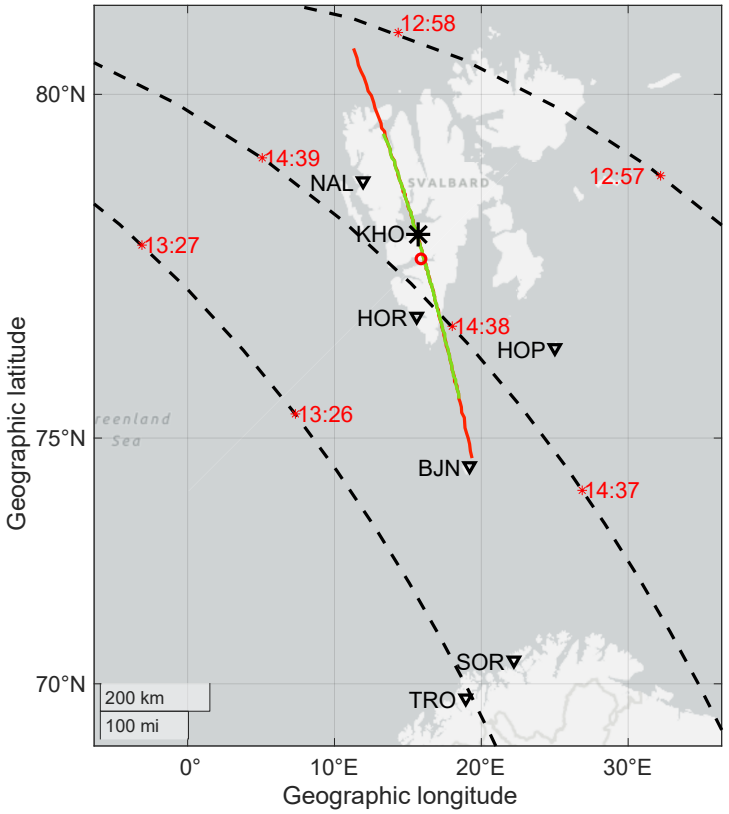

Figure 1. The location of KHO (black star), which coincides with the LYR ground-based magnetometer, and the MSP. The ESR beam at 250 km altitude (red circle), the MSP field-of-view for 557.7 and 630.0 nm (green and red lines), and ground-based magnetometers from the IMAGE chain (nabla signs) are shown. The black dashed lines give the DMSP overpasses with corresponding time stamps [UT] in red.

The ESR provides profiles of ionospheric plasma parameters including the electron density, N_e, electron and ion temperatures, T_e and T_i, and the ion line-of-sight velocity, v_i. We only used the non-steerable, field-aligned, parabolic dish (42 m antenna) of the ESR. The radar was running from 12:27–13:36 UT at an altitude range between 77–470 km, and the data is analyzed at a 1 min temporal resolution. At 250 km altitude, corresponding to the assumed 630.0 nm emission height, the ESR beam width is around 3.5 km width and pointing at 75° mlat as shown in Figure 1.

The ELectron Spectrum (ELSPEC) method (Virtanen et al., 2018) inverts the localized, field-aligned ESR electron density measurements between 80–150 km altitude to determine the differential fluxes of precipitating electrons ranging from 1–

https://doi.org/10.5194/egusphere-2025-5220
Preprint. Discussion started: 4 November 2025

100 keV. With this information, the upward FACs and the total energy flux are estimated. For each fit, the goodness of the fit is monitored via the χ^2 value, for which a small χ^2 value indicates that the model fits the data well. The Lompe method, on the other hand, represents a larger-scale inversion model that can incorporate a variety of data sources to obtain FACs, convection velocities, and Joule heating rates, among others (Laundal et al., 2022; Hovland et al., 2022). In this paper, the conductance within the Lompe model is based on auroral precipitation, Σ_{precip}, as detected by DMSP/SSUSI, solar EUV, Σ_{EUV}, and a constant background conductance, Σ_{BG} (sometimes referred to as starlight conductance) of 2 mho (Robinson et al., 2021; Laundal et al., 2025) following

$$\Sigma = \sqrt{\Sigma_{BG}^2 + \Sigma_{EUV}^2 + \Sigma_{precip}^2}. \quad (1)$$

In addition, magnetic field data from the ground, provided by SuperMAG (Gjerloev, 2012), and from space, specifically from Iridium, provided via the Active Magnetosphere and Planetary Electrodynamics Response Experiment (AMPERE; Anderson et al., 2017), and from Swarm, are added. In addition, convection data from SuperDARN is added. During our UAA event, we have three DMSP overpasses, at 12:57 and 14:38 UT (DMSP F17), and at 13:26 UT (DMSP F18), thus giving us three snapshots of the Lompe model. For each snapshot, the grid is defined such that it lies completely within the DMSP overpass to ensure that we have conductance data throughout the whole grid. The Lompe method combines ground- and space-based magnetometer measurements with measurements of plasma convection to derive the electric field within the analysis grid using the ionospheric Ohm's law, with an assumed conductance distribution. More information on how the different quantities are calculated can be found in Laundal et al. (2022).

The ion upflow flux can be determined with both the ESR and the DMSP/SSIES observations, using $f_i = v_{i,upflow} \times n_i$. The upflow velocity, $v_{i,upflow}$ is measured by ESR as the line-of-sight velocity, v_i, and by SSIES as the vertical ion drift, $v_{i,vert}$. The ion density, n_i, can be approximated by the electron density, N_e, (ESR) or the general plasma density, n, (DMSP/SSIES) using the quasi-neutrality assumption. In case of the DMSP/SSIES, electron fluxes from the DMSP/SSJ instrument are used to confirm the presence of auroral particle precipitation.

3 Results

The UAA event in this study takes place on 16 November 2021 between 13:00–14:30 UT under low geomagnetic activity as indicated by Kp = 2. It is identified using the detection algorithm by Van Hazendonk et al. (2025) in MSP data as shown in Figure 2. The original detection took place in the 630.0 nm channel (Figure 2a), in which the wave is detected from 13:00–14:30 UT between 72–75° magnetic latitude (mlat) using a 1 h window. The reconstructed wave fronts are overlaid in red. The wave has a frequency of 1.1 mHz, and a poleward velocity of 740 m s^{-1}. Figure 2b shows that there is also detection in the 557.7 nm wavelength channel between 13:00–15:00 UT and 73–74° mlat using a 1 h window. To get a better understanding of this event, we studied data from the ESR to confirm the presence of ion upflow and quantify the ion upflow flux. The IMAGE ground-based magnetometer chain gives more insight on the nature of the UAA event. For insight into the energy dynamics, FAC magnitudes and total energy fluxes are determined both locally and globally using the ELSPEC and Lompe methods and the DMSP/SSUSI instrument. Lompe is also used to get an estimate of the Joule heating rates.

https://doi.org/10.5194/egusphere-2025-5220
Preprint. Discussion started: 4 November 2025

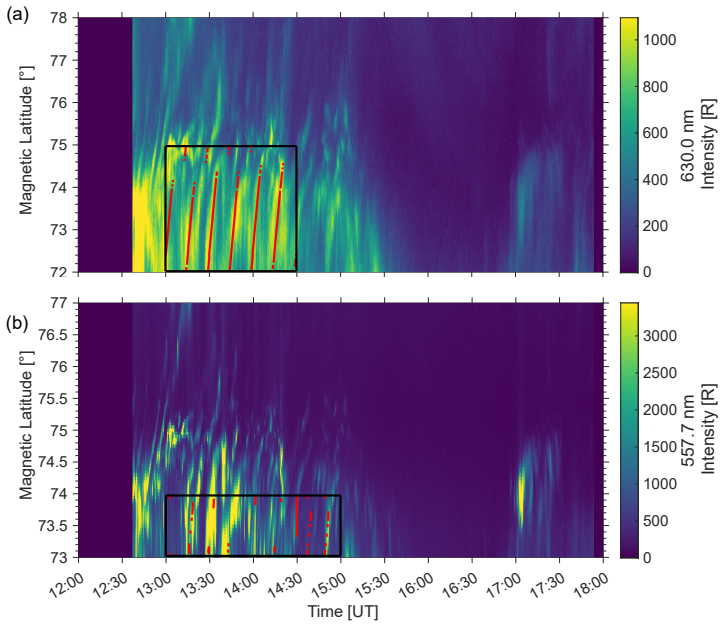

Figure 2. Detection of a UAA event in keograms of both the 630.0 and 557.7 nm channels of the MSP on 16 November 2021. The borders of the detected UAA event (in time and mlat) are shown in black and the reconstructed wavefronts are overlaid in red.

The ESR data are plotted in Figure 3. The radar was running between 12:27–13:36 UT, except for a short interruption between 12:49 and 12:53 UT. Up to 12:55 UT, the ionosphere was quiet with low electron densities, as shown in Figure 3a. From 12:55 UT onward, the electron density increases in the E and F-region ionosphere, indicative of particle precipitation. This precipitation is occurring periodically with a period of 10 min, which indicates the presence of UAAs in the radar beam. The precipitation causes the electron temperature (panel b) to increase with the same periodicity. However, no similar increases are visible in the ion temperature (panel c), suggesting a lack of frictional heating and/or Joule heating.

The observed periodicity in the ESR (10 min) is lower than that detected in the MSP (15 min). This is presumably caused by the fact that the localized ESR beam, which is pointing at 75° mlat, is located at the edge of the UAA event. The MSP keogram, Figure 2a, shows that the auroral arcs at 75° mlat appear slightly more frequently between 13:00–13:30 UT compared to the bulk event around 73.5° mlat. The MSP data in Figure 2a suggest that the emission intensity range remains constant throughout the wave field with maxima up to 1050 R. We thus assume that the ESR measurements provide a realistic estimation of the event despite its limited beam width.

To further look into the nature of the UAA event, we have analyzed the variation in spectral power and phase with latitude using stations from the IMAGE magnetometer chain. At the wave frequency detected in the MSP, 1.1 mHz, the power and

https://doi.org/10.5194/egusphere-2025-5220
Preprint. Discussion started: 4 November 2025

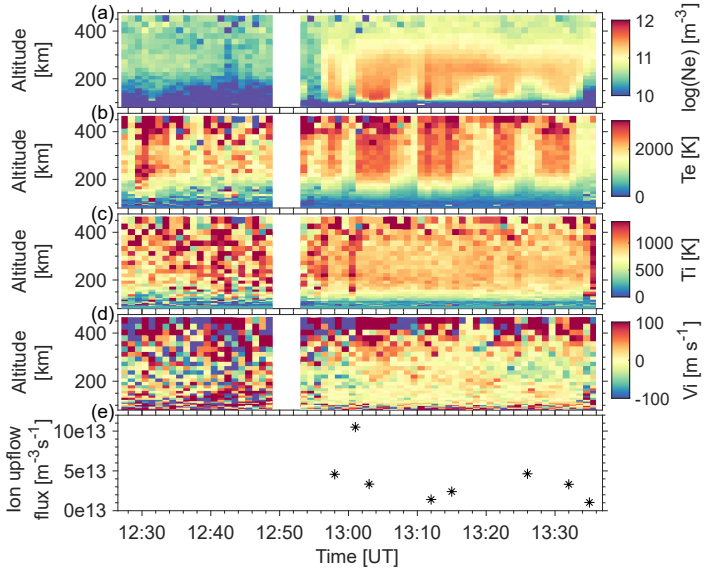

Figure 3. Ionospheric plasma parameters as measured by ESR on 16 November 2021 in panels a-d. Panel a shows the logarithmic electron density, panel b and c the electron and ion temperature respectively, and panel d the ion line-of-sight velocity where positive velocities are away from the radar. Panel e shows the ion upflow flux calculated using the average electron density and ion velocity between 400–470 km altitude when the upflow criterium from Ogawa et al. (2009) is satisfied.

phase variations are shown in Figure 4a. It can be seen that the spectral power (solid line) has a peak above the HOR (77° geographic latitude (glat); 74° mlat) and HOP (76.5° glat; 73° mlat) magnetometer stations, thus supporting the detection in the MSP between 72–75° mlat. The phase (dashed line) change in Figure 4a between SOR (70.5° glat; 67.3° mlat) and LYR (78.2° glat; 75.1° mlat) is around 240°. Thus, it exceeds the expected 180° change for a classical FLR (Menk and Waters, 2013). This could be caused by the lack of ground-magnetometer stations between SOR and BJN (74.5° glat; 71.5° mlat). However, the phase change between BJN and HOP is almost zero, while these stations correspond to a steep gradient in spectral power. This indicates that, despite the event showing a clear power peak around HOR and HOP, the UAA event does not have a classic FLR nature. The individual power spectra, as shown in Figure 4b, show a wider frequency peak between 1.1–2 mHz in HOR and HOP indicating a more complicated dynamics. Magnetometers sense a larger area compared to the MSP, and each station integrates the effects of all currents within its field-of-view into one measurement. This makes it harder to distinguish the UAA signal. In addition, the magnetometers used in this study are located close to the ocean, making their signals sensitive to induced currents in the conducting ocean, which can make up 50% of the signal (Juusola et al., 2020).

https://doi.org/10.5194/egusphere-2025-5220
Preprint. Discussion started: 4 November 2025

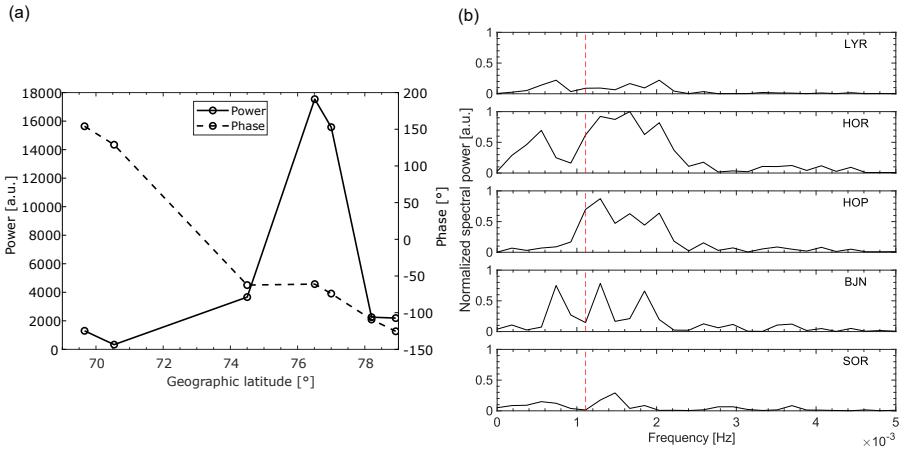

Figure 4. Panel a: Variation of the spectral power (left y-axis; solid line) and phase (right y-axis; dashed line) at 1.1 mHz between 13:00–14:30 UT using the magnetometer stations TRO, SOR, BJN, HOP, HOR, LYR, and NAL. Panel b shows the spectral power between 0–5 mHz for the stations SOR, BJN, HOP, HOR, and LYR, in which the dashed red line indicates the 1.1 mHz frequency.

Figure 3e shows the ion upflow flux when the detection criterion by Ogawa et al. (2009) (i.e. at least three consecutive altitude bins of v_i, shown in Figure 3d, exceeding 100 m s^{-1}) is satisfied and the flux exceeds 1×10^{13} m^{-2} s^{-1} in order to qualify as ion upflow flux (David et al., 2018). It can be seen that the periodic increases in N_e and T_e are accompanied by ion upflow fluxes ranging between $1 \times 10^{13} - 1 \times 10^{14}$ m^{-2} s^{-1}, with a median of 3.3×10^{13} m^{-2} s^{-1}. One data point suggests the ion upflow to be strong, while the other fluxes fall into the medium and low category. The increased N_e at lower altitudes, indicative of precipitation, in combination with the T_e, and lack of T_i, enhancements suggests the upflow to be of type 2. This fits well with the general ion upflow behavior at 16 MLT as indicated by Ogawa et al. (2009, Figure 7 herein), which shows that statistically ion upflow at 16 MLT is most likely to occur with only enhancements in T_e. Based on the low geomagnetic activity (Kp=2) we would expect the ion upflow to be low (David et al., 2018).

To investigate whether the ion upflow could result in outflow, the three DMSP overpasses have been studied. DMSP/SSJ energetic electron data are shown in Figure 5. Panel a indicates that the first overpass (12:57–12:58 UT) occurs on open field lines due to the lack of energetic electron precipitation after 12:57 UT. This overpass is located northeast of Svalbard and thus poleward of our UAA event. The energetic electron precipitation of the second (13:26–13:27 UT) and third (14:38–14:39 UT) overpass, as shown in Figure 5 b and c, indicates that these overpasses, and thus our UAA event, take place on closed field lines. Densities and ion velocities from the DMSP/SSIES instrument (not shown), however, do not indicate ion outflow signatures for these overpasses. During the period of strongest upflow (around 13:00 UT), we do not have a corresponding DMSP overpass co-located with the UAA event. The co-located overpasses at 13:27 and 14:38 UT indicate that the ion upflow at those times was not strong enough to result in ion outflow.

https://doi.org/10.5194/egusphere-2025-5220
Preprint. Discussion started: 4 November 2025

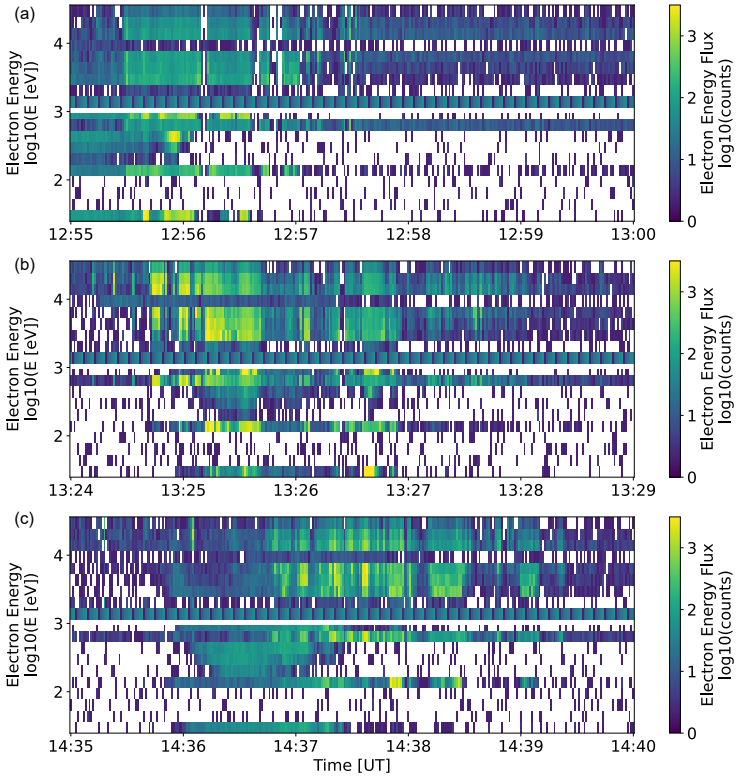

Figure 5. Electron spectrograms from three DMSP/SSJ overpasses between 12:55–13:00 UT (panel a), 13:24–13:29 UT (panel b), 14:35–14:40 UT (panel c). The electron energy flux is plotted as a function of logarithmic electron energy and time.

FACs give an indication of ongoing energy coupling processes between the magnetosphere and the ionosphere. Both the ELSPEC method, based on EISCAT data, and the Lompe method provide estimates of FACs. However, they do so on different length scales. ELSPEC, as shown in Figure 6, where panel d shows the FAC magnitudes, provides a localized measurement by inverting the EISCAT electron density. The measured value of N_e is depicted in Figure 6a, while the modeled version is shown in panel b. Generally, the ELSPEC model underestimates the FAC magnitude, because it only takes electrons with energies above 1 keV into account. The FAC magnitudes in the ELSPEC method range up to 6 μA m^{-2}. The Lompe method provides a larger-scale overview compared to ELSPEC. In our case, we have chosen the time stamps of the model based on the DMSP overpasses over Svalbard, resulting in three snapshots of which the relevant elements are shown in Figure 7. The Lompe analysis are based on 5 min windows centered at 12:57, 13:27, and 14:38 UT. The top row of Figure 7 corresponds to

https://doi.org/10.5194/egusphere-2025-5220
Preprint. Discussion started: 4 November 2025

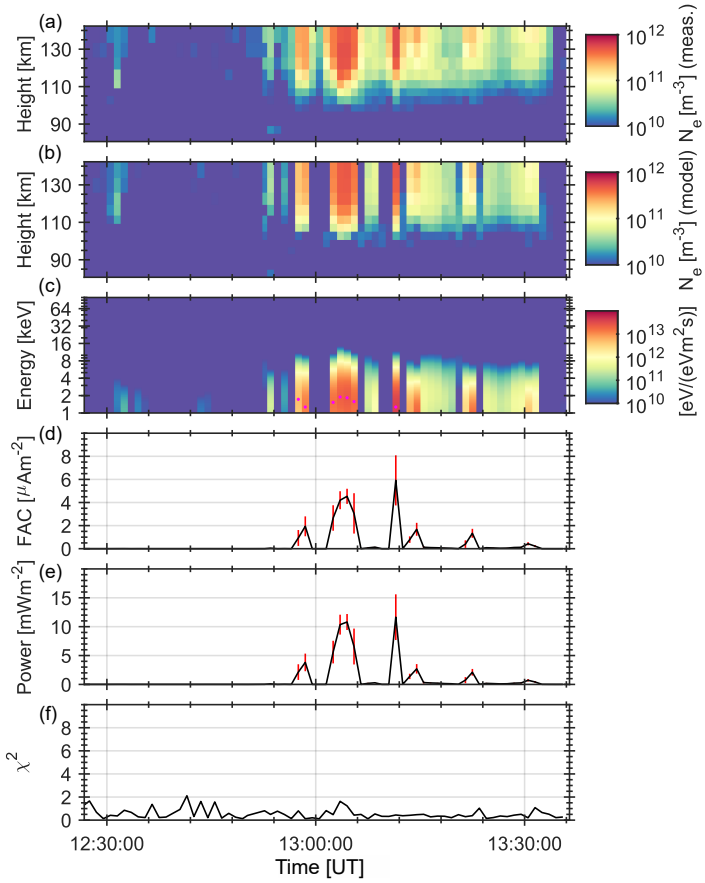

Figure 6. The ELSPEC method which shows: the observed electron density between 80–150 km altitude by the ESR (panel a), the electron density modeled in the inversion (panel b), the differential energy flux (panel c), the upward FACs (panel d), the total energy flux (panel e), and the χ^2 parameter (panel f). The red bars in panels d and e are 1-σ error estimates.

12:57 UT, the middle row to 13:27 UT, and the bottom row to 14:38 UT. The full snapshots of the inversion can be found in Appendix A. The solutions in the Lompe method are dominated by ground-based magnetometers and Iridium, since there is very little SuperDARN data available in the analysis region, and none around Svalbard. In addition, only the last snapshot, at 14:38 UT, contains a few Swarm data points located at the northern edge of the grid, while for the other snapshots no Swarm data is available. The FACs in the Lompe inversion (Figure 7 panels a, e, and i; the blue and red color scale shows the FAC magnitudes, where red corresponds to upward and blue to downward FACs), show magnitudes up to ± 3 μA m^{-2} between 72–

https://doi.org/10.5194/egusphere-2025-5220
Preprint. Discussion started: 4 November 2025

75° mlat. At 12:57 UT, Figure 7a, the ESR beam (at 75° mlat) is located in an upward FAC (red) region, while at 13:27 and 14:38 UT (panels e and i), the ESR beam is located in regions of downward FACs. At these times upward FACs are observed further south in the UAA detection region. This corresponds well with the observed higher FAC values in the ELSPEC method around 13:00 UT. In general, the ELSPEC FAC magnitudes, despite their underestimation, exceed those of Lompe during times of auroral precipitation. Both FAC magnitudes compare well to previously reported values. In case of FLRs, values of 3–6 μA m^{-2} (Gillies et al., 2018), 2–3 μA m^{-2} (Lotko et al., 1998), up to 5 μA m^{-2} (Walker et al., 1992), and 2–4 μA m^{-2} (Fenrich et al., 2019) have been reported. For small-scale waves, FAC magnitudes of 1–4 μA m^{-2} (Milan et al., 2001) and 0.8 μA m^{-2} (Baddeley et al., 2017) have been found. The UAA event thus shows FAC strengths equaling those of FLRs.

Another feature of the FACs in the Lompe method is the alternating direction of the FACs above and just south of Svalbard. This feature is visible in all three Lompe snapshots, but most pronounced at 13:27 UT, as shown in Figure 7e. The modeled FAC directions in Figure 7e can be seen directly in an Iridium overpass right over Svalbard providing magnetic field measurements as shown in orange in Appendix A Figure A1. Similar alternating FAC directionality has previously been observed in combination with a ULF wave event by Fenrich et al. (2019) using data from the SuperDARN radars and the Swarm spacecraft.

Furthermore, the Lompe inversion gives an estimation of the convection velocities. The detection in the MSP shows us that the UAA event is moving with a poleward velocity of around 740 m s^{-1}. This is comparable to the convection velocity in Lompe at 13:27 UT (Figure 7e; the quiver field). At 12:57 UT (Figure 7a), Svalbard is on the edge of the two convection cells, making it hard to extract precise velocities, while the convection velocity at 14:38 UT (Figure 7i), after the detected UAA event has ended, is slightly lower.

The ELSPEC method, as shown in Figure 6, also gives an estimation of the total energy flux in the panel e. During the brightest auroral arcs, which take place between 13:00–13:15 UT, the total energy flux goes up to 12 mW m^{-2}. Outside of this time range, the maximum total energy flux is up to 5 mW m^{-2}. A similar energy estimate is provided using the DMSP/SSUSI instrument as shown in Figure 8 for the first two overpasses. Around 12:57 UT, as shown in Figure 8a, the electron energy flux around Svalbard just exceeds 10 mW m^{-2}, while it is around 3 mW m^{-2} at 13:27 UT. Both the ELSPEC method and the DMSP/SSUSI instrument are thus giving comparable energy dissipation fluxes, showing the strongest energy fluxes around 13:00 UT and weaker fluxes around 13:30 UT. This indicates that the local features captured with the ESR are representative of the larger wavefronts of the UAA event as observed by the DMSP spacecraft. These energy flux magnitudes are comparable to the DMSP/SSUSI fluxes previously reported by Van Hazendonk et al. (2024), which equaled 8–10 mW m^{-2} within the ULF wavefronts.

To investigate how the total energy flux is dissipated, we determined the Joule heating using the Lompe method as shown in Figure 7 panels c, g, and h. Peak Joule heating rates range between 8–11 mW m^{-2}. The strongest Joule heating is found in regions between up- and downward FACs, as these areas are characterized by the horizontal Pedersen currents that close the current loops in the ionosphere. In between those regions, Joule heating is limited with base levels between 0.5–2 mW m^{-2}. The regions with alternating FAC directions, while partly located within the UAA detection region, are mostly found south of the ESR beam. This could explain the lack of T_i enhancements and thus the lack of Joule heating inside the narrow ESR beam. Outside of the ESR beam, the UAA event shows signs of Joule heating as indicated by Lompe. The Joule heating dissipation

https://doi.org/10.5194/egusphere-2025-5220
Preprint. Discussion started: 4 November 2025

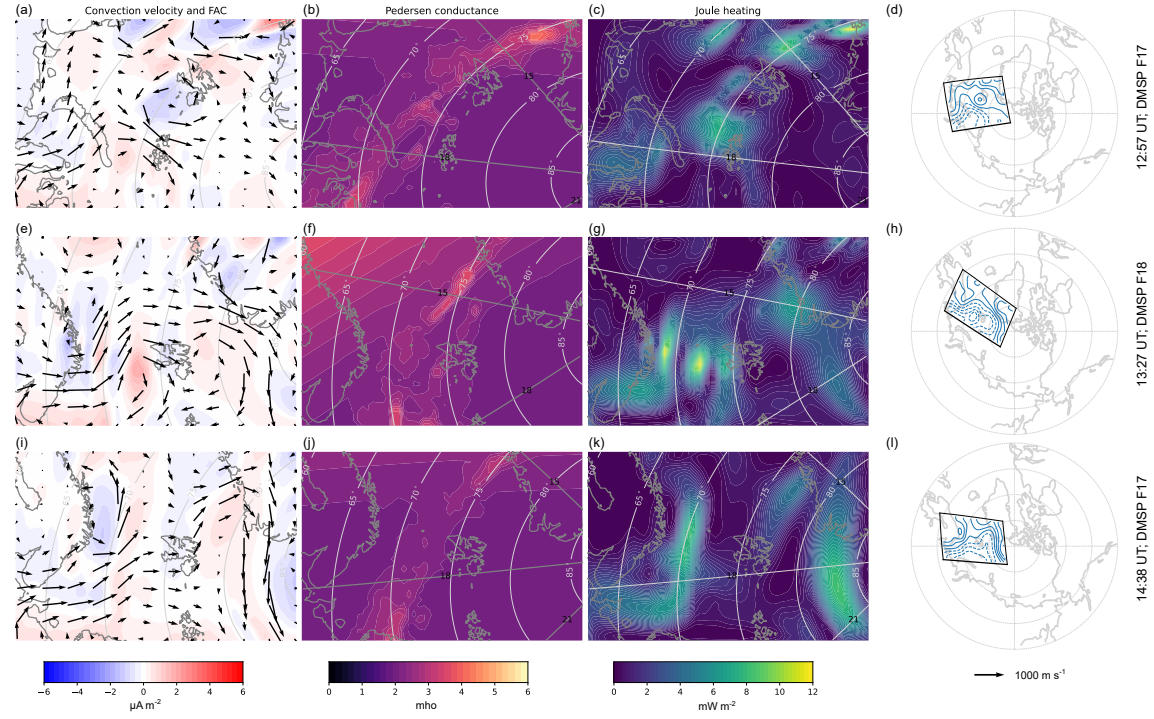

Figure 7. The Lompe inversion at 12:57 UT (top row; panels a–d), 13:27 UT (middle row; panels e–h), and 14:38 UT (bottom row; panels i–l). The first column (panels a, e, and i) shows the convection velocities (quiver field) and the FAC magnitudes (red/blue colormap). The second column (panels b, f, and j) provides the Pedersen conductance, and the third column (panels c, g, and k) the Joule heating. The last column (panels d, h, and l) shows the location of the grid with respect to the magnetic local time and magnetic coordinates. The full data panels of each run are given in Appendix A.

rates are comparable to those reported previously for ULF wave events with low/intermediate *m*-numbers and exceed those of high *m*-number waves as shown in the comparison of Table 1. Comparing to the statistical study by Aikio et al. (2012), our base Joule heating rates fall mostly into the quiet geomagnetic conditions category (Kp: 0–2^+), thus corresponding well with the observed Kp value of 2, while the peaks indicate high geomagnetic activity (Kp $\geq 5^-$). This observation is in line with previous findings which showed that the presence of ULF waves increases the dissipation rates above the otherwise expected levels and that ULF waves contribute significantly to the energy budget (Rae et al., 2007; Hartinger et al., 2015; Van Hazendonk et al., 2024).

https://doi.org/10.5194/egusphere-2025-5220
Preprint. Discussion started: 4 November 2025

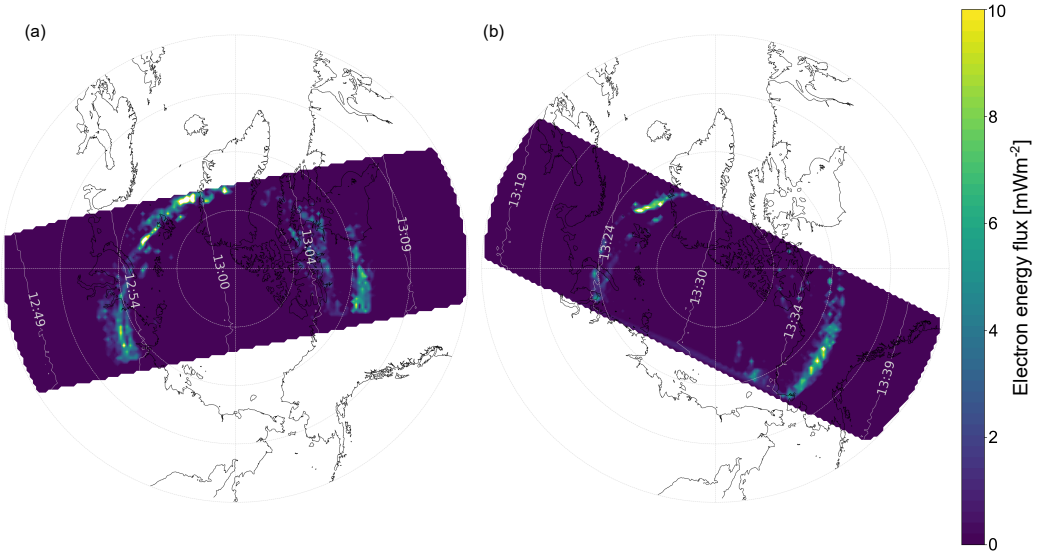

Figure 8. The dissipated electron energy flux measured by the DMSP/SSUSI instrument for overpass 1 (panel a) and overpass 2 (panel b).

	m-number	Joule heating [mW m^{-2}]
Van Hazendonk et al. (2024)	Low/intermediate	0.5–3 (base level) and 20 (peaks)
Hartinger et al. (2015)	Low	0.1–1 (>10 for extreme cases)
Rae et al. (2007)	Low	1.3 (mean) and 7.3 (peaks)
Baddeley et al. (2005)[a]	High and high	0.075 and 0.68
Aikio et al. (2012)	No ULF waves	0.5–1 (quiet), 2–3 (moderate), 5–10 (high)[b]

[a] Baddeley et al. (2005) present two separate ULF wave events.

[b]The rates from Aikio et al. (2012) are median values between 16:00–17:30 MLT. Peak values can be up to double the median values.

Table 1. Previously reported Joule heating dissipation rates. A similar version of this table has been published in Van Hazendonk et al. (2024).

4 Discussion

The UAA event on 16 November 2021 13:00–14:30 UT (16:00–17:30 MLT) detected in the MSP is located between 72–75° mlat and has a frequency of 1.1 mHz. Observations in the ESR show the presence of auroral arcs via periodic electron precipitation in the E- and F-region combined with electron temperature increases. Associated with the arcs, type 2 ion upflow is located with predominantly low and medium fluxes. In general, the event shows a complicated dynamics with partly ambiguous

https://doi.org/10.5194/egusphere-2025-5220
Preprint. Discussion started: 4 November 2025

observations across different instruments. On one hand, ground-based magnetometers suggest a non-FLR nature and thus indicate small-scale ULF waves. On the other hand, FAC magnitudes, total energy dissipation rates, and Joule heating rates are comparable to previous large-scale, possible FLR-like, events.

The ionospheric ion upflow observed in this paper provides its first direct link to UAAs. Previously, ion outflow has been observed in the inner magnetosphere at lower latitudes during storm time (Chaston et al., 2015). This outflow was connected to kinetic Alfvén waves, and it was hypothesized that simultaneous ionospheric outflow occurred. Our event shows that ionospheric upflow can indeed occur in relation to UAAs, thus fitting within the framework by (Chaston et al., 2015). To understand the physical mechanisms explaining the connection between ionospheric ion upflow and UAAs, the model proposed by Samson et al. (2003) and expanded upon by Rankin et al. 2021, gives some insights. This model describes the connection between FACs and the FLR wave field, in which the FLR generates a parallel electric current that is supported by a parallel electric field. This parallel electric field accelerates electrons and ions into the ionosphere causing the UAAs. Based on this model, we expect to observe T_i enhancements in the ESR data, adjacent to the arcs, due to Joule heating caused by the Pedersen currents that close the FAC circuit in the ionosphere. As is seen from figure 3, whilst no T_i enhancements were observed between the arcs, electron density and temperature enhancements are observed, indicating particle acceleration into the ionosphere by a parallel E-field within the arcs.

All in all, the UAA event consists of enough energy input to cause ion upflow, but, based on the ESR data alone, not enough to cause significant Joule heating. This supports that the UAA event consists of smaller-scale ULF waves with a non-FLR nature as also indicated by the ground-based magnetometers. Instead of energy being predominantly deposited via Joule heating, ESR data indicate that part of the dissipated energy went into the acceleration of particles causing N_e and T_e enhancements. Similarly to Van Hazendonk et al. (2024), the kinetic flux might be more important than previously expected. An alternative explanation is that the ESR beam is located too far north to capture the bulk of the Joule heating.

The Lompe model indicates significant Joule heating within the UAA area, as shown in Figure 7c, g, and k, but locates this Joule heating predominantly south of the ESR beam. These Joule heating rates are comparable to those previously found for large-scale ULF wave events. In our case, however, the Joule heating might be overestimated due to strong dependency on the conductance in the Lompe model. The very limited availability of convection data caused the outputs of the Joule heating and convection velocities to be heavily affected by small changes in conductance. Since the ionospheric currents, $\boldsymbol{J}$, are mostly based on magnetic field data, an increase in conductance results in a decrease in electric field following Ohm's law: $\boldsymbol{J} = \Sigma \boldsymbol{E}$. The $\boldsymbol{E} \times \boldsymbol{B}$ drift then results in a reduced convection velocity. We calculated the conductance using Equation 1, thus depending on the auroral precipitation, solar EUV, and the background conductance. The first term is based on input data from DMSP/SSUSI, while the second one is calculated using well-known empirical formulae as given by Moen and Brekke (1993). The background conductance, however, is a less-known term. Previously, $\Sigma_{BG} = 2$ mho has been used (Robinson et al., 2021; Laundal et al., 2025). Recently, Juusola et al. (2025) used long EISCAT time series, both from Tromsø and Svalbard, to determine empirical conductances. The residual of the fit then provided background conductances of $\Sigma_{BG,P} = 0.625 \pm 0.008$ mho and $\Sigma_{BG,H} = 0.894 \pm 0.011$ mho for respectively the Pedersen and Hall background conductances. The ESR data indicate conductances around 0.5 mho before 12:50 UT, while increasing to 1–3 mho in between the auroral arcs during the UAA

https://doi.org/10.5194/egusphere-2025-5220
Preprint. Discussion started: 4 November 2025

event. Convection flows are expected to be < 1 km s^{-1} as geomagnetic conditions are quiet. This lead us to use a background conductance of 2 mho, as background conductances ≤ 1 mho would imply convection flows > 1 km s^{-1}, and Joule heating rates up to 25 mW m^{-2}. The strong dependence of the Joule heating and convection velocity on the background conductance, makes both results less reliable. The comprehensive picture of this event – including both the ESR, DMSP, and Lompe data – thus shows little evidence of large Joule heating especially within the narrow ESR beam. However, it does show enough energy input into the ionosphere to cause particle precipitation and ion upflow.

Furthermore, the input data to the Lompe model in our case mostly comes from ground- and space-based magnetometers. This provides two challenges. Firstly, the Lompe technique implicitly connects all magnetic field perturbations observed by magnetometers within the grid to ionospheric currents within the same grid (Laundal et al., 2022). This might not be true, since magnetometers sense large areas, which can extend across grid boundaries. Secondly, small-scale ULF waves are prone to ionospheric attenuation and thus not always visible in ground-based magnetometer data (e.g. Takahashi et al., 2013). As our event shows a non-FLR signature in the ground-based magnetometer data (Figure 4), it is likely that the magnetometers, and thus the Lompe method, do not fully capture the ULF wave dynamics. We do therefore believe that the direct observations carry more weight than the outputs of the Lompe model, especially regarding the Joule heating rates and convection velocities.

The observed UAA event has a non-FLR nature, and exhibits small-scale signatures like ionospheric attenuation. This would indicate a generation mechanism internal to the Earth's magnetosphere. On the other hand, FAC magnitudes as provided by ELSPEC and Lompe could indicate larger-scale ULF waves. High solar wind speeds of around 600 km s^{-1}, as shown in Appendix A Figure A4b, could cause external generation at the Kelvin-Helmholtz instability on the flanks of the magnetopause. The solar wind dynamic pressure, shown in Appendix A Figure A4c, does not indicate that external pressure pulses play a role in the generation.

The periodic enhancements in both the MSP and ESR as well as the slanted and poleward moving structures in the MSP, indicate the presence of UAAs as explained in Van Hazendonk et al. (2025). However, poleward moving auroral forms (PMAFs) can appear similarly in MSP data (Xing et al., 2012). PMAFs are a dayside phenomena, mostly occurring on open magnetic field lines. However, negative B_y in combination with positive B_z, which is the case for our event as shown in Appendix A Figure A4a, can cause an asymmetry towards post-noon, making it possible for PMAFs to occur during our event timing (Xing et al., 2012; Yang and Xiang, 2022). However, as discussed earlier, the DMSP/SSJ particle detector data (Figure 5) show that the UAA event most likely takes place on closed-field lines as indicated by the overpasses at 13:27 and 14:38 UT. We do thus believe that the UAA event takes place on closed field lines and is unlikely to be a PMAF event.

5 Conclusions

In this paper, we presented a comprehensive study of a poleward moving ULF wave driven auroral arc event, utilizing ground-, and space-based instrumentation as well as models. The event takes place on 16 November 2021 between 13:00–14:30 UT (16:00–17:30 MLT) and is located on closed field lines between 72–75° mlat (above Svalbard). Its frequency of 1.1 mHz corresponds to a 15 min periodicity, and the poleward propagation velocity is 740 m s^{-1}. The UAA event provides a strong

https://doi.org/10.5194/egusphere-2025-5220
Preprint. Discussion started: 4 November 2025

coupling between the ionosphere and magnetosphere, which is visible through ion upflow, FACs, and energy dissipation. The ion upflow flux falls within the low to medium category with fluxes of around 3.3×10^{13} m^{-2} s^{-1} without proof of outflow. The FACs can locally have magnitudes of at least 6 µA m^{-2} as estimated from the ESR electron density measurements. At larger scales the Lompe output gives values around 3 µA m^{-2}, while also showing the alternating FAC directionality in 2D. The total energy flux peaks at 8 mW m^{-2} (large-scale) and 12 mW m^{-2} (small-scale), thus showing significant dissipation. Part of this energy is dissipated as kinetic energy via particle acceleration and precipitation as observed in the ESR. No co-located Joule heating was found due to lack of T_i enhancements in the ESR beam, but there is an indication of Joule heating up to 11 mW m^{-2} outside this narrow radar beam.

Different measurements provide ambiguous information on the exact nature of the UAA event. On one hand, ground-based magnetometers indicate small-scale waves with a non-FLR nature and the lack of T_i enhancements suggests that most of the UAA energy is deposited via kinetic processes rather than Joule and/or frictional heating as expected for FLRs. On the other hand, FAC magnitudes and energy dissipation rates match those of large-scale, FLR-like events. This shows that the available instrumentation in combination with existing frameworks and models cannot fully capture the complicated UAA dynamics. Additional instrumentation, such as auroral imaging from space or spatially extended incoherent scatter measurements, could provide more accurate conductivity estimations needed for improved understanding of the ULF wave energy budget and their role in the ionosphere–magnetosphere coupling. Ion upflow should be considered in these future, multi-instrument studies. To the best of our knowledge, this paper now provides the first direct observations of ionospheric ion upflow associated with UAAs.

Code and data availability. EISCAT data is available at https:/madrigal.eiscat.se in hdf5 files containing already analyzed data with an integration time of 1 min. The MSP data for this event is available through the NIRD research data archive under DOI https://doi.org/10.11582/2025.B9FR665W. DMSP data can be downloaded from https://cdaweb.gsfc.nasa.gov/pub/data/dmsp/. The magnetometer data for the FFT analysis is obtained from the IMAGE magnetometer network via https://space.fmi.fi/image/ (10 s time resolution), while the input magnetometer data for the Lompe model comes from SuperMAG https://supermag.jhuapl.edu/. The other data used for the Lompe model is retrieved from https://ampere.jhuapl.edu/ (Iridium), https://vires.services/ (Swarm), and https://doi.org/10.5281/zenodo.7821883 (SuperDARN). Solar wind data, shifted to the bowshock nose, were obtained from the GSFC/SPDF OMNIWeb interface at https://omniweb.gsfc.nasa.gov/form/sc_merge_min1.html.

The Lompe model and ELSPEC method are both available at GitHub via https://github.com/klaundal/lompe and https://github.com/ilkkavir/ELSPEC, respectively.

Appendix A: Additional figures

In this section, the figures containing the full output of the Lompe method are included for the three different snapshots. In addition, the solar wind data is shown.

https://doi.org/10.5194/egusphere-2025-5220
Preprint. Discussion started: 4 November 2025

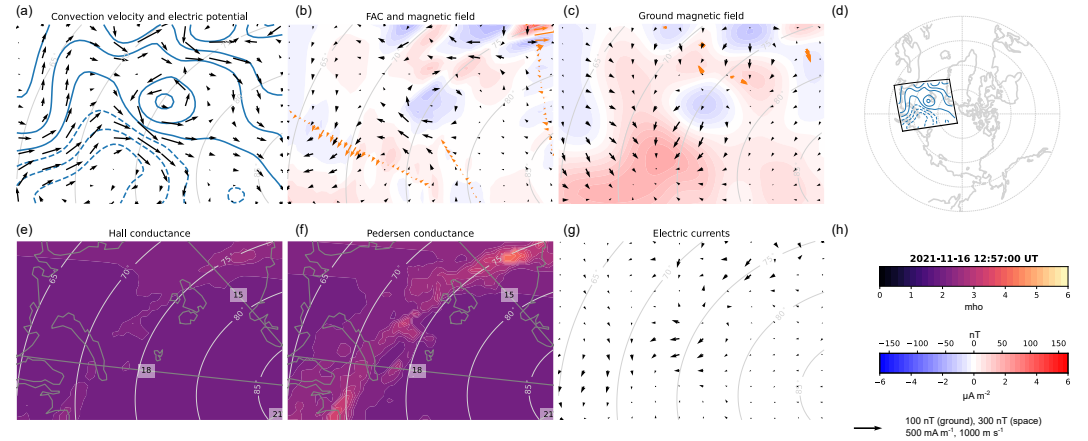

Figure A1. The full Lompe output for the 12:57 UT snapshot. Panel a shows the convection velocity (black arrows), and the electric potential contours. Panel b depicts the horizontal magnetic field disturbances at 110 km altitude (black arrows), the Iridium horizontal magnetic field measurements (orange arrows), and the FAC densities (color scale). Panel c gives the horizontal ground magnetic field perturbations (black arrows), the SuperMAG horizontal magnetic field perturbations in orange, and the radial magnetic field perturbations (color contours). Panel d shows the location of the grid with respect to the magnetic local time and magnetic coordinates. Panels e and f give the Hall and Pedersen conductance, respectively, and panel g the horizontal height-integrated ionospheric currents. Panel h gives the color and vector scales.

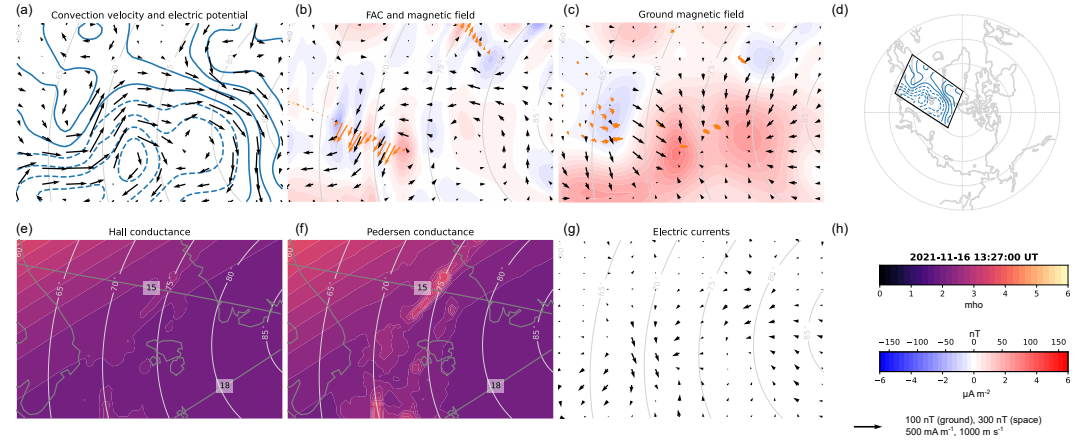

Figure A2. Same as Figure A1, but for the 13:27 UT snapshot.

https://doi.org/10.5194/egusphere-2025-5220
Preprint. Discussion started: 4 November 2025

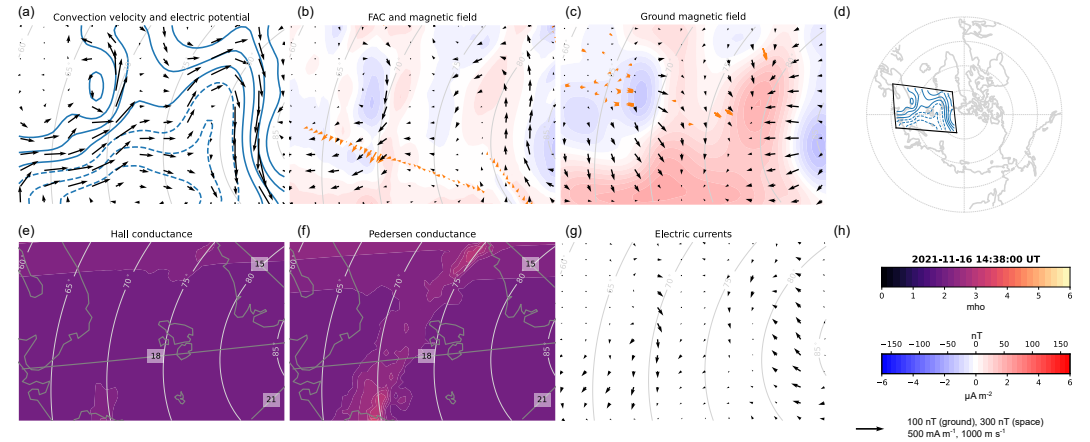

Figure A3. Same as Figure A1, but for the 14:38 UT snapshot.

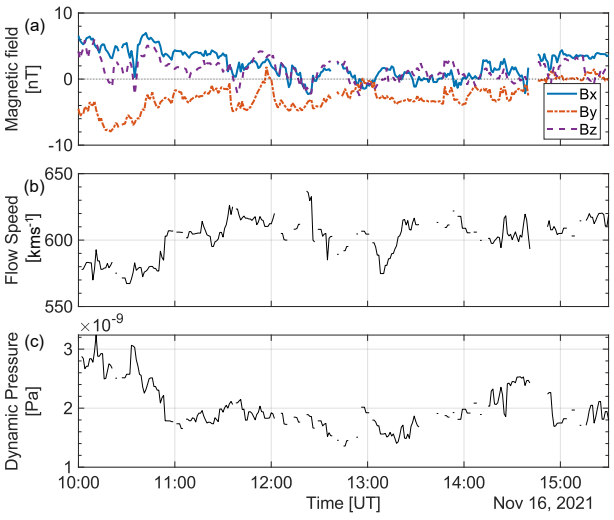

Figure A4. The solar wind data before and during the UAA event. Panel a shows the interplanetary magnetic field, panel b the solar wind velocity, and panel c the solar wind dynamic pressure.

https://doi.org/10.5194/egusphere-2025-5220
Preprint. Discussion started: 4 November 2025

Author contributions. CvH, LB, and KL conceptualized the study and selected the case study event. CvH wrote most of the manuscript and performed the data analysis. CvH, LB, and KL participated in the initial interpretation of the data, while all authors contributed to the discussing of the results, and editing of the manuscript.

Competing interests. The authors declare that they have no conflict of interest.

Acknowledgements. We want to thank Fasil Tesema for his help with the Lompe code for this event. We acknowledge EISCAT, which is an international association supported by research organizations in China (CRIRP), Finland (SA), Japan (NIPR and ISEE), Norway (NFR), Sweden (VR), and the United Kingdom (UKRI). We thank the institutes who maintain the IMAGE Magnetometer Array, for the data in this paper this specifically concerns the Tromsø Geophysical Observatory of UiT the Arctic University of Norway (Norway), and the Institute of Geophysics Polish Academy of Sciences (Poland). We gratefully acknowledge the SuperMAG collaborators (https://supermag.jhuapl.edu/info/?page=acknowledgement). The authors acknowledge the use of SuperDARN data. SuperDARN is a collection of radars funded by national scientific funding agencies of Australia, Canada, China, France, Italy, Japan, Norway, South Africa, United Kingdom and the United States of America. We thank the AMPERE team and the AMPERE Science Center for providing the Iridium-derived data products.

https://doi.org/10.5194/egusphere-2025-5220
Preprint. Discussion started: 4 November 2025

References

Aikio, A. T., Cai, L., and Nygrén, T.: Statistical distribution of height-integrated energy exchange rates in the ionosphere, Journal of Geophysical Research: Space Physics, 117, A10 325, https://doi.org/10.1029/2012JA018078, 2012.

Anderson, B. J., Korth, H., Welling, D. T., Merkin, V. G., Wiltberger, M. J., Raeder, J., Barnes, R. J., Waters, C. L., Pulkkinen, A. A., and Rastaetter, L.: Comparison of predictive estimates of high-latitude electrodynamics with observations of global-scale Birkeland currents, Space Weather, 15, 352–373, https://doi.org/10.1002/2016SW001529, 2017.

Baddeley, L. J., Yeoman, T. K., Wright, D. M., Trattner, K. J., and Kellet, B. J.: On the coupling between unstable magnetospheric particle populations and resonant high m ULF wave signatures in the ionosphere, Annales Geophysicae, 23, 567–577, https://doi.org/10.5194/angeo-23-567-2005, 2005.

Baddeley, L. J., Lorentzen, D. A., Partamies, N., Denig, M., Pilipenko, V. A., Oksavik, K., Chen, X., and Zhang, Y.: Equatorward propagating auroral arcs driven by ULF wave activity: Multipoint ground- and space-based observations in the dusk sector auroral oval, Journal of Geophysical Research: Space Physics, 122, 5591–5605, https://doi.org/10.1002/2016JA023427, 2017.

Bjoland, L. M., Ogawa, Y., and Haaland, S.: Characteristics of the ambipolar electric field during ion upflow events, Earth, Planets and Space, 77, 78, https://doi.org/10.1186/s40623-025-02217-6, 2025.

Chaston, C. C., Bonnell, J. W., Wygant, J. R., Kletzing, C. A., Reeves, G. D., Gerrard, A., Lanzerotti, L., and Smith, C. W.: Extreme ionospheric ion energization and electron heating in Alfvén waves in the storm time inner magnetosphere, Geophysical Research Letters, 42, https://doi.org/10.1002/2015GL066674, 2015.

David, T. W., Wright, D. M., Milan, S. E., Cowley, S. W. H., Davies, J. A., and McCrea, I.: A Study of Observations of Ionospheric Upwelling Made by the EISCAT Svalbard Radar During the International Polar Year Campaign of 2007, Journal of Geophysical Research: Space Physics, 123, 2192–2203, https://doi.org/10.1002/2017JA024802, 2018.

David, T. W., Michael, C. M., Wright, D., Talabi, A. T., and Ajetunmobi, A. E.: Ionospheric upwelling and the level of associated noise at solar minimum, Annales Geophysicae, 42, 349–354, https://doi.org/10.5194/angeo-42-349-2024, 2024.

Fenrich, F. R., Gillies, D. M., Donovan, E., and Knudsen, D.: Flow Velocity and Field-Aligned Current Associated With Field Line Resonance: SuperDARN Measurements, Journal of Geophysical Research: Space Physics, 124, 4889–4904, https://doi.org/10.1029/2019JA026529, 2019.

Gillies, D. M., Knudsen, D., Donovan, E., Jackel, B., Gillies, R., and Spanswick, E.: Identifying the 630 nm auroral arc emission height: A comparison of the triangulation, FAC profile, and electron density methods, Journal of Geophysical Research: Space Physics, 122, 8181–8197, https://doi.org/10.1002/2016JA023758, iSBN: 10.1002/2016 Publisher: John Wiley & Sons, Ltd, 2017.

Gillies, D. M., Knudsen, D., Rankin, R., Milan, S., and Donovan, E.: A Statistical Survey of the 630.0-nm Optical Signature of Periodic Auroral Arcs Resulting From Magnetospheric Field Line Resonances, Geophysical Research Letters, 45, 4648–4655, https://doi.org/10.1029/2018GL077491, 2018.

Gjerloev, J. W.: The SuperMAG data processing technique, Journal of Geophysical Research: Space Physics, 117, 2012JA017 683, https://doi.org/10.1029/2012JA017683, 2012.

Godbole, N. H., Lessard, M. R., Kenward, D. R., Fritz, B. A., Varney, R. H., Michell, R. G., and Hampton, D.: Observations of ion upflow and 630.0 nm emission during pulsating aurora, Frontiers in Physics, 10, 997 229, https://doi.org/10.3389/fphy.2022.997229, 2022.

Hartinger, M. D., Moldwin, M. B., Zou, S., Bonnell, J. W., and Angelopoulos, V.: ULF wave electromagnetic energy flux into the ionosphere: Joule heating implications, Journal of Geophysical Research: Space Physics, 120, 494–510, https://doi.org/10.1002/2014JA020129, 2015.

https://doi.org/10.5194/egusphere-2025-5220
Preprint. Discussion started: 4 November 2025

Herlingshaw, K., Partamies, N., Van Hazendonk, C. M., Syrjäsuo, M., Baddeley, L. J., Johnsen, M. G., Eriksen, N. K., McWhirter, I., Aruliah, A., Engebretson, M. J., Oksavik, K., Sigernes, F., Lorentzen, D. A., Nishiyama, T., Cooper, M. B., Meriwether, J., Haaland, S., and Whiter, D.: Science highlights from the Kjell Henriksen Observatory on Svalbard, Arctic Science, 11, 1–25, https://doi.org/10.1139/as-2024-0009, 2025.

Hovland, A. Ø., Laundal, K. M., Reistad, J. P., Hatch, S. M., Walker, S. J., Madelaire, M., and Ohma, A.: The Lompe code: A Python toolbox for ionospheric data analysis, Frontiers in Astronomy and Space Sciences, 9, 1025 823, https://doi.org/10.3389/fspas.2022.1025823, 2022.

Ji, E., Jee, G., and Lee, C.: Characteristics of the Occurrence of Ion Upflow in Association With Ion/Electron Heating in the Polar Ionosphere, Journal of Geophysical Research: Space Physics, 124, 6226–6236, https://doi.org/10.1029/2019JA026799, 2019.

Juusola, L., Vanhamäki, H., Viljanen, A., and Smirnov, M.: Induced currents due to 3D ground conductivity play a major role in the interpretation of geomagnetic variations, Annales Geophysicae, 38, 983–998, https://doi.org/10.5194/angeo-38-983-2020, 2020.

Juusola, L., Virtanen, I., Hatch, S. M., Vanhamäki, H., Grandin, M., Partamies, N., Ganse, U., Honkonen, I., Workayehu, A., Kero, A., and Palmroth, M.: An empirical model of high-latitude ionospheric conductances based on EISCAT observations, https://doi.org/10.5194/egusphere-2025-2394, 2025.

Laundal, K. M., Reistad, J. P., Hatch, S. M., Madelaire, M., Walker, S., Hovland, A. O., Ohma, A., Merkin, V. G., and Sorathia, K. A.: Local Mapping of Polar Ionospheric Electrodynamics, Journal of Geophysical Research: Space Physics, 127, e2022JA030 356, https://doi.org/10.1029/2022JA030356, 2022.

Laundal, K. M., Skeidsvoll, A. S., Popescu Braileanu, B., Hatch, S. M., Olsen, N., and Vanhamäki, H.: Global Inductive Magnetosphere-Ionosphere-Thermosphere Coupling, https://doi.org/10.5194/egusphere-2025-2051, 2025.

Lotko, W., Streltsov, A. V., and Carlson, C. W.: Discrete auroral arc, electrostatic shock and suprathermal electrons powered by dispersive, anomalously resistive field line resonance, Geophysical Research Letters, 25, 4449–4452, https://doi.org/10.1029/1998GL900200, 1998.

Lynch, K. A., Semeter, J. L., Zettergren, M., Kintner, P., Arnoldy, R., Klatt, E., LaBelle, J., Michell, R. G., MacDonald, E. A., and Samara, M.: Auroral ion outflow: low altitude energization, Annales Geophysicae, 25, 1967–1977, https://doi.org/10.5194/angeo-25-1967-2007, 2007.

Menk, F. W. and Waters, C. L.: Magnetoseismology: Ground-Based Remote Sensing of Earth's Magnetosphere, Wiley, 1 edn., ISBN 978-3-527-41027-9 978-3-527-65205-1, https://doi.org/10.1002/9783527652051, 2013.

Milan, S. E., Sato, N., Ejiri, M., and Moen, J.: Auroral forms and the field-aligned current structure associated with field line resonances, Journal of Geophysical Research: Space Physics, 106, 25 825–25 833, https://doi.org/10.1029/2001JA900077, 2001.

Moen, J. and Brekke, A.: The solar flux influence on quiet time conductances in the auroral ionosphere, Geophysical Research Letters, 20, 971–974, https://doi.org/10.1029/92GL02109, 1993.

Ogawa, Y., Fujii, R., Buchert, S. C., Nozawa, S., and Ohtani, S.: Simultaneous EISCAT Svalbard radar and DMSP observations of ion upflow in the dayside polar ionosphere, Journal of Geophysical Research: Space Physics, 108, 2002JA009 590, https://doi.org/10.1029/2002JA009590, 2003.

Ogawa, Y., Buchert, S. C., Fujii, R., Nozawa, S., and Van Eyken, A. P.: Characteristics of ion upflow and downflow observed with the European Incoherent Scatter Svalbard radar, Journal of Geophysical Research: Space Physics, 114, 2008JA013 817, https://doi.org/10.1029/2008JA013817, 2009.

Ogawa, Y., Buchert, S. C., Häggström, I., Rietveld, M. T., Fujii, R., Nozawa, S., and Miyaoka, H.: On the statistical relation between ion upflow and naturally enhanced ion-acoustic lines observed with the EISCAT Svalbard radar, Journal of Geophysical Research: Space Physics, 116, https://doi.org/10.1029/2010JA015827, 2011.

https://doi.org/10.5194/egusphere-2025-5220
Preprint. Discussion started: 4 November 2025

Partamies, N., Whiter, D., Kauristie, K., and Massetti, S.: Local time dependence of auroral peak emission height and morphology, preprint, Magnetosphere & space plasma physics/Auroral ionosphere, https://doi.org/10.5194/angeo-2022-6, 2022.

Partamies, N., Dayton-Oxland, R., Herlingshaw, K., Virtanen, I., Gallardo-Lacourt, B., Syrjäsuo, M., Sigernes, F., Nishiyama, T., Nishimura, T., Barthelemy, M., Aruliah, A., Whiter, D., Mielke, L., Grandin, M., Karvinen, E., Spijkers, M., and Ledvina, V. E.: First observations of continuum emission in dayside aurora, Annales Geophysicae, 43, 349–367, https://doi.org/10.5194/angeo-43-349-2025, publisher: Copernicus GmbH, 2025.

Paxton, L. J., Meng, C.-I., Fountain, G. H., Ogorzalek, B. S., Darlington, E. H., Gary, S. A., Goldsten, J. O., Kusnierkiewicz, D. Y., Lee, S. C., Linstrom, L. A., Maynard, J. J., Peacock, K., Persons, D. F., and Smith, B. E.: Special sensor ultraviolet spectrographic imager: an instrument description, pp. 2–15, San Diego, CA, https://doi.org/10.1117/12.60595, 1992.

Rae, I. J., Watt, C. E. J., Fenrich, F. R., Mann, I. R., Ozeke, L. G., and Kale, A.: Energy deposition in the ionosphere through a global field line resonance, Annales Geophysicae, 25, 2529–2539, https://doi.org/10.5194/angeo-25-2529-2007, 2007.

Redmon, R. J., Denig, W. F., Kilcommons, L. M., and Knipp, D. J.: New DMSP database of precipitating auroral electrons and ions, Journal of Geophysical Research: Space Physics, 122, 9056–9067, https://doi.org/10.1002/2016JA023339, 2017.

Robinson, R. M., Zanetti, L., Anderson, B., Vines, S., and Gjerloev, J.: Determination of Auroral Electrodynamic Parameters From AMPERE Field-Aligned Current Measurements, Space Weather, 19, e2020SW002 677, https://doi.org/10.1029/2020SW002677, 2021.

Samson, J. C., Rankin, R., and Tikhonchuk, V. T.: Optical signatures of auroral arcs produced by field line resonances: comparison with satellite observations and modeling, Annales Geophysicae, 21, 933–945, https://doi.org/10.5194/angeo-21-933-2003, 2003.

Skjæveland, Å., Moen, J., and Carlson, H. C.: On the relationship between flux transfer events, temperature enhancements, and ion upflow events in the cusp ionosphere, Journal of Geophysical Research: Space Physics, 116, A10 305, https://doi.org/10.1029/2011JA016480, 2011.

Skjæveland, Å., Moen, J., and Carlson, H. C.: Which cusp upflow events can possibly turn into outflows?, Journal of Geophysical Research: Space Physics, 119, 6876–6890, https://doi.org/10.1002/2013JA019495, 2014.

Takahashi, K., Hartinger, M. D., Angelopoulos, V., Glassmeier, K., and Singer, H. J.: Multispacecraft observations of fundamental poloidal waves without ground magnetic signatures, Journal of Geophysical Research: Space Physics, 118, 4319–4334, https://doi.org/10.1002/jgra.50405, 2013.

Tanskanen, E. I.: A comprehensive high-throughput analysis of substorms observed by IMAGE magnetometer network: Years 1993–2003 examined, Journal of Geophysical Research: Space Physics, 114, 2008JA013 682, https://doi.org/10.1029/2008JA013682, 2009.

Van Hazendonk, C., Baddeley, L., Laundal, K., and Lorentzen, D.: A statistical study of optical signatures of high-latitude Pc5 waves, Journal of Atmospheric and Solar-Terrestrial Physics, p. 106585, https://doi.org/10.1016/j.jastp.2025.106585, 2025.

Van Hazendonk, C. M., Baddeley, L., Laundal, K. M., and Chau, J. L.: Detection and Energy Dissipation of ULF Waves in the Polar Ionosphere: A Case Study Using the EISCAT Radar, Journal of Geophysical Research: Space Physics, 129, e2024JA032 633, https://doi.org/10.1029/2024JA032633, 2024.

Virtanen, I. I., Gustavsson, B., Aikio, A., Kero, A., Asamura, K., and Ogawa, Y.: Electron Energy Spectrum and Auroral Power Estimation From Incoherent Scatter Radar Measurements, Journal of Geophysical Research: Space Physics, 123, 6865–6887, https://doi.org/10.1029/2018JA025636, 2018.

Wahlund, J.-E., Opgenoorth, H. J., Häggström, I., Winser, K. J., and Jones, G. O. L.: EISCAT observations of topside ionospheric ion outflows during auroral activity: Revisited, Journal of Geophysical Research: Space Physics, 97, 3019–3037, https://doi.org/10.1029/91JA02438, 1992.

https://doi.org/10.5194/egusphere-2025-5220
Preprint. Discussion started: 4 November 2025

Walker, A. D. M., Ruohoniemi, J. M., Baker, K. B., Greenwald, R. A., and Samson, J. C.: Spatial and temporal behavior of ULF pulsations observed by the Goose Bay HF Radar, Journal of Geophysical Research: Space Physics, 97, 12 187–12 202, https://doi.org/10.1029/92JA00329, 1992.

Xing, Z., Yang, H., Han, D., Wu, Z., Hu, Z., Zhang, Q., Kamide, Y., Hu, H., Zhang, B., Liu, J., and Huang, D.: Poleward moving auroral forms (PMAFs) observed at the Yellow River Station: A statistical study of its dependence on the solar wind conditions, Journal of Atmospheric and Solar-Terrestrial Physics, 86, 25–33, https://doi.org/10.1016/j.jastp.2012.06.004, 2012.

Yang, Q. and Xiang, H.: Unsupervised Learning of Auroral Optical Flow for Recognition of Poleward Moving Auroral Forms, IEEE Transactions on Geoscience and Remote Sensing, 60, 1–11, https://doi.org/10.1109/TGRS.2021.3083369, 2022.

Zettergren, M., Semeter, J., Blelly, P., and Diaz, M.: Optical estimation of auroral ion upflow: Theory, Journal of Geophysical Research: Space Physics, 112, 2007JA012 691, https://doi.org/10.1029/2007JA012691, 2007.

Graphic design: Communication Division, UiB / Print: Skipnes AS

uib.no

ISBN: 9788230892183 (print)
9788230892367 (PDF)